LAND TIME-LAPSE CSEM

COLLECTING, MODELING AND INVERSION OF CSEM DATA FOR A STEAM-INJECTED OIL FIELD

LAND TIME-LAPSE CSEM

COLLECTING, MODELING AND INVERSION OF CSEM DATA FOR A STEAM-INJECTED OIL FIELD

Proefschrift

ter verkrijging van de graad van doctor
aan de Technische Universiteit Delft,
op gezag van de Rector Magnificus prof. dr. ir. T.H.J.J. van der Hagen,
voorzitter van het College voor Promoties,
in het openbaar te verdedigen op vrijdag 9 februari 2018 om 10:00 uur

door

Andreas Manuel SCHALLER

Master of Science in Applied Geophysics (RWTH Aachen, ETH Zürich en TU Delft)
geboren te München, Duitsland.

Dit proefschrift is goedgekeurd door de

promotor: Prof. dr. ir. E.C. Slob
copromotor: Dr. ir. G.G. Drijkoningen

Samenstelling promotiecommissie:

Rector Magnificus	voorzitter
Prof. dr. ir. E.C. Slob	Technische Universiteit Delft
Dr. ir. G.G. Drijkoningen	Technische Universiteit Delft
Onafhankelijke leden:	
Prof. dr. ir. C.P.A. Wapenaar	Technische Universiteit Delft
Prof. dr. W.A. Mulder	Technische Universiteit Delft
Prof. dr. O. Ritter	Helmholtz Center Potsdam
Dr. R. Streich,	Global Solutions International BV
Prof. dr. A.M. Ziolkowski	University of Edinburgh

Funded by: Dutch CCS research programme CO2 Afvang, Transport en Opslag (CATO2)

Keywords: electromagnetics, CSEM, land, 3D, case history, inversion, vertical electric field, repeatability, time-lapse

ISBN 000-00-0000-000-0

An electronic version of this dissertation is available at
`http://repository.tudelft.nl/`.

CONTENTS

1

INTRODUCTION

1.1. THE USE OF CSEM FOR EXPLORATION AND RESERVOIR MONITORING

The global oil demand is expected to continue rising, despite the ever-expanding importance of renewable energy. Therefore, in the long term, it will only be possible to satisfy the demand for the full range of energy products by combining renewables with cleaner hydrocarbons, and deploying technology to capture and store emissions of CO_2. With the recognition of the energy transition era and the significance of climate change, oil production is moving on recovering more from previously drilled and less desirable reservoirs by using secondary and tertiary methods and on optimizing oil field exploration by providing more energy with less carbon dioxide. Proper design of development programs together with the optimization of field life, creates a need of deploying key technologies for, mainly land-based, sustainable oil recovery and carbon dioxide storage.

To improve energy efficiency in the production and to minimize the risk of production failures, it is essential to know the spatial propagation of the fluids in the reservoir by use of monitoring techniques. Monitoring leads to a better understanding of the processes that occur inside a reservoir, can assist in determining fluid contacts and injection fronts, and has an impact on ultimate recovery and drilling procedures. For example, for Enhanced Oil Recovery (EOR) improved reservoir imaging is essential for optimizing fluid (e.g., steam, water) injection. For CO_2 storage, (semi-) permanent reservoir monitoring benefits in early identification of potential CO_2 leakages. It reduces the likelihood of unwanted emission of CO_2 that is harming the environment and is the basis for creating detailed models to ensure safe storage of CO_2.

Among the available approaches for reservoir monitoring, flow and thermal control systems, geophysical methods offer non-destructive in-situ measurements and are increasingly used. In general, passive and active geophysical monitoring can be distinguished. Passive monitoring focuses on measuring the background fields and can be performed permanently, while active monitoring needs a source signal and is therefore

mostly done on a temporary basis repeated over time, so-called time-lapse. In other words, to identify when injection processes start to cause unwanted effects i.e. fracturing or CO_2 leakages and to allow for faster and better reservoir decisions, surveys should be repeated on a short time interval. One of the geophysical method that is routinely applied for active-source monitoring is the seismic reflection method. The seismic reflection method is based on interpreting changes in the media's elastic properties that result from replacing reservoir fluids during injection. This method has been proven effective for detecting and monitoring the injection and spreading of steam (Michou et al., 2013) and geologically stored CO_2 (Strickland et al., 2014; Ivandic et al., 2012).

Despite of successful implementation of the seismic method for reservoir monitoring, seismic approaches (1) do not detect changes in electrical resistivity inside the reservoir (are sensitive to pressure changes)(2) are not always able to distinguish the fluid content in the rock (Wright et al., 2002; Wilt and Alumbaugh, 1998) and (3) are relatively expensive (mainly due to their instrumentation intensity). Therefore, we seek alternative, more cost-effective geophysical methods for long-term reservoir monitoring that can distinguish differences between various pore fluids of a reservoir. As the resistivity difference between hydrocarbon-bearing and steam- or water-saturated rocks can be significant (Wright et al., 2002), electromagnetic methods may be potentially suitable for detecting temporal variations inside the reservoir that are not detectable with the seismic method alone and thus can be used for reservoir monitoring (Um and Alumbaugh, 2007; Lien and Mannseth, 2008). Electromagnetic methods are generally employed to measure the conductivity (or resistivity) of fluid-saturated rocks, which may aid in discriminating highly resistive hydrocarbon-bearing rocks from those with relatively more conductive saline formation water. Still, many wells have resistivity logs and gathering additional EM data would provide 3D knowledge of the resistivity distribution inside an oil or gas field.

For reservoir monitoring, we require an advanced method that can reach sufficient penetration depth and that can deal with the increased complexity of the reservoir fluid systems due to the use of enhanced oil recovery methods. Such a method that uses low frequencies and can provide resistivity maps of the subsurface (Everett and Meju, 2005) is the Controlled-Source ElectroMagnetic (CSEM) method. At these frequencies, the EM signals exhibit a diffusive character in the earth in contrast to the wave-propagation character of seismics. The CSEM method has generally a higher resolution than potential-field methods such as gravity (Li and Oldenburg, 1998; Dell'Aversana et al., 2012) and may be able to detect complex field patterns, introduced by multi-phase flow in the reservoir. As an example, steam injected into a resistive hydrocarbon reservoir is generally even more resistive, thus creating a high-resistivity zone around the injector well. However, the steam condensates and mixes with usually saline formation water leading to a more conductive zone and consequently a resistivity decrease away from the injector well. One of the challenges is the interpretation of these complex transition zones in the reservoir, where oil (or gas) coexists and /or mixes with water or steam. The CSEM method can be applied in an attempt to monitor and further understand this complex behavior.

Electromagnetic methods were initially developed on land, however large-scale (CS)EM surveys on land are not commonly conducted, and the knowledge provided in

the literature is still limited, especially with respect to monitoring approaches (Streich, 2016). In a marine environment, the CSEM method has been widely used for derisking drilling activities (MacGregor and Sinha, 2000; Ellingsrud et al., 2002; Hoversten et al., 2006; Darnet et al., 2007; Constable, 2010; Fanavoll et al., 2014; Houck et al., 2015; Hesthammer et al., 2010a,b; Johansen, 2008). It is challenging to replicate the success of the marine method to land. In marine CSEM surveys, dense 2D profiles or complex 3D grids with tens of transmitter tow lines and hundreds to thousands of receiver deployments are feasible and source coverage is ample due to moving sources (Constable, 2010). Such source and receiver coverage is very difficult to achieve for land surveys because of various typically terrestrial constraints (access restrictions, urbanization, presence of infrastructure and noise sources). In addition, deploying sources of sufficient strength is difficult. In contrast to the marine case where the transmitter is situated in the most conductive area, the seawater, land transmitters are usually situated on the surface, or air-earth interface, and they are deployed in a medium much more resistive than seawater, which makes it difficult to achieve strong source currents. The absence of the attenuating seawater results in higher levels of cultural EM noise and air-wave energy that mask target responses. Further, more near-surface heterogeneity exists on land than at the sea floor and close-by interfaces can result in more complex electric-field patterns close to the transmitter.

CSEM data can either be acquired and processed in the time or in the frequency domain. Time- and frequency-domain data are in principle equivalent and uniquely related by the Fourier transform and thus EM data can be represented in either domain without information loss. Since either domain may highlight different parts of the information contained in the data, choosing the domain is thus a "personal" choice and may additionally depend on available equipment and preferred acquisition layout. The air wave influence can be reduced by separating the signal and processing the data in the time domain since the airwave travels with the speed of light and is thus separated in time from subsurface responses that propagate more slowly. Therefore, transient EM measurements (a technique in which electric and magnetic fields are induced by transient pulses of electric current and the subsequent decay response measured) and time-domain processing has been the preferred CSEM method for many authors on land (Ziolkowski et al., 2007, 2011; McCracken et al., 1980; Frischknecht and Raab, 1984; Strack, 1992; Andrieux et al., 2000; Wright et al., 2002). Time-domain processing potentially may enhance subsurface signals due to better separation of the airwave from the subsurface response (see Figure 4, Streich, 2016), although interpretation of noise-plagued transients remains difficult. In this thesis, the data were interpreted in the frequency domain, similar to the marine CSEM method. At the time of planning the survey, we were convinced that frequency-domain measurements were the best option. We believed that (1) the available source and receiver equipment favored a non-transient measurement, since the source was primarily built for emitting low-frequency square waves or variants thereof and the recording equipment had low maximal sampling rates and that (2) we can achieve a good signal-to-noise ratio by continuous long-lasting measurements per source position. We attempted to get low noise levels at each station, where "noise" is not a certain arrival – like the air wave but primarily man-made cultural noise. The highest signal-to-noise levels were required to evaluate the possibility of measuring E_z.

Although a frequency domain approach was chosen in this thesis, we are aware that the source is capable to be used as a transient source and that the power of deconvolution gain in signal processing could favor transient measurements. However, transient measurements were never tested and thus optimized transient measurements were not compared to optimized frequency-domain measurements. A recent review of CSEM approaches for hydrocarbon exploration and monitoring on land is given by Streich (2016).

In the light of the energy transition, enhanced oil recovery and carbon dioxide storage programs are mainly focused on land and require monitoring. However, due to multiple challenges, there is a lack of real data examples for the land use of the CSEM method. The recent successes in the marine environment and technical advances in the accuracy of recording equipment make it worthwhile to evaluate the land application of CSEM again. Recently conducted EM surveys, which can be considered technology trials rather than commercial surveys (e.g., Streich and Becken, 2011; Grayver et al., 2014; Streich, 2016; Tietze et al., 2015) have indicated that there is potential in the land CSEM method. Therefore, the main objective of this thesis is to investigate the potential of the land CSEM method for monitoring steam injection into an oil field on actual field data. Since there is very limited knowledge on inverting actual field data, one goal of the thesis is the usage of 1D and 3D inversion tools to invert CSEM data. Further, we test the monitoring capability of the CSEM method by evaluating time-lapse measurements, measuring all components of the electric field and by analyzing the repeatability of the CSEM data acquisition, an important precondition for successful monitoring that has hardly been studied in literature.

1.2. RESEARCH OBJECTIVES AND THESIS OUTLINE

The work described in this thesis explores various aspects to improve the land CSEM method for exploration and monitoring purposes. Since there exists very limited knowledge on inverting actual CSEM field data on land and on the measurement repeatabitlity, we carried out three separate active land CSEM field experiments, a baseline and two repeat surveys. The data were acquired over a period of nearly two years at the Dutch Schoonebeek oil field, where heavy oil is produced by injecting steam to reduce the viscosity of the oil. Steam injection and oil production have to be closely monitored to prevent breakthrough of steam to production wells and to detect possible unwanted leakage or contamination of groundwater such that further measures can be taken. The field survey layout, a single receiver line and two source positions, including any permitting work and detailed positioning of sources and receivers, was done by Shell. I focus on two different approaches, namely the measurement of the horizontal electric-field component via surface receivers and a novel method of measuring the vertical electric-field component via electrodes in shallow boreholes. The thesis starts with background information on the Schoonebeek area and on the field survey (**Chapter 2**). This chapter gives a compact overview of the Schoonebeek oil field, introduces the Steam-Assisted Gravity Drainage (SAGD) used for EOR and explains the acquisition layout. The measurements and the main processing steps that are repeatedly applied during the subsequent chapters are explained. Optimized placement of source and receivers is needed to enhance the resolution in the reservoir. I show pre-survey studies that were performed to justify the survey layout by evaluating optimal source and receiver positions.

Whereas Chapter 3 focuses on the base survey, Chapter 4 and Chapter 5 include the two repeat surveys. Details, necessary to understand the chapter, are repeated throughout the following chapters such that the main parts of each chapter can be read independently of each other.

In **Chapter 3**, I discuss the potential of using the land CSEM method to improve onshore hydrocarbon exploration. I start with synthetic studies and highlight the applicability of the land CSEM method for recovering the resistivity distribution inside a target reservoir by using 1D and 3D inversions. The underlying mathematical theory of EM inversion is well established, but the application to real data requires a thorough analysis of uncertainties in the inversion result. I use a deterministic inversion approach, in which gradients are derived from the forward-model process and used to update a sequence of models. Further, I numerically investigate resolution capability in terms of the survey geometry, noise distortion, reservoir depth and resistivity distribution inside the reservoir. Data are inverted either from single receivers or from a collection of receivers and their inversion results are compared. Then, I give an example of the field data collected during the base survey. The data were inverted for the resistivity distribution inside the reservoir where the injected steam leads to more complex resistivity patterns close to the injector and producer wells. I investigate if the sparse source-receiver configuration has the potential of resolving complex resistivity patterns inside the reservoir zone. Further, I discuss to what extent small-scale variations of resistivity can be detected.

In **Chapter 4**, I focus on the repeatability potential of land CSEM measurements, since the time interval between the base and the repeat surveys is too short to be able to detect resistivity changes inside the reservoir due to steam injection and oil production. Therefore, the acquired field data were identically processed and inverted for the resistivity distribution in the subsurface. I highlight the importance of high-accuracy, high-precision and high-repeatability measurements.

Up to this point of the thesis, the research was limited to the horizontal electric-field components. **Chapter 5** deals with a novel approach to measure the vertical electric-field component by deploying electrodes in shallow boreholes. Previous synthetic studies showed that the vertical electric-field component is more sensitive to resistive changes in the reservoir and thus might have the potential to measure even minor changes that would be too small to detect the horizontal electric-field components. I begin the chapter by synthetically studying the sensitivity of the near-surface vertical electric field compared to the sensitivity of the horizontal electric field. This is followed by an extensive synthetic study about the advantages and challenges of vertical electric-field measurements. I highlight the importance of borehole deviation that has to be known and included in modeling, inversion, and interpretation of the data. At the Schoonebeek field, electrodes were actually installed in shallow vertical boreholes. It shows additional technical challenges due to high cultural EM noise, near-surface heterogeneities and large metallic objects in the vicinity of the receiver and source locations that lead to a complex interpretation. Further, I study the potential of getting an improved image of the resistivity distribution inside the reservoir and its changes when combining vertical and horizontal data.

I conclude the work in **Chapter 6** and give an outlook for further studies that may improve future time-lapse land CSEM measurements. As the EM field is diffusive for the

frequency range used in the CSEM method, the resolution capability is low. To enhance resolution, wave-propagation methods such as the seismic method can be used in parallel for a joint interpretation or inversion of the data.

REFERENCES

Andrieux, P., F. Neubauer, K. Vozoff, et al., 2000, A first attempt at monitoring underground gas storage by means of time-lapse multichannel transient electromagnetics: Geophysical Prospecting, **48**, 489–509.

Constable, S., 2010, Ten years of marine CSEM for hydrocarbon exploration: Geophysics, **75**, 75A67–75A81.

Darnet, M., M. C. K. Choo, R. . Plessix, M. L. Rosenquist, K. Yip-Cheong, E. Sims, and J. W. K. Voon, 2007, Detecting hydrocarbon reservoirs from CSEM data in complex settings: Application to deepwater Sabah, Malaysia: Geophysics, **72**, WA97–WA103.

Dell'Aversana, P., S. Colombo, B. Ciurlo, J. Leutscher, and J. Seldal, 2012, CSEM data interpretation constrained by seismic and gravity data: An application in a complex geological setting: First Break, **30**, 43–52.

Ellingsrud, S., T. Eidesmo, S. Johansen, M. Sinha, L. MacGregor, and S. Constable, 2002, Remote sensing of hydrocarbon layers by seabed logging (SBL): Results from a cruise offshore Angola: The Leading Edge, **21**, 972–982.

Everett, M. E., and M. A. Meju, 2005, Near-surface controlled-source electromagnetic induction: background and recent advances: Springer. (Chapter in Hydrogeophysics).

Fanavoll, S., P. T. Gabrielsen, and S. Ellingsrud, 2014, CSEM as a tool for better exploration decisions: Case studies from the Barents Sea, Norwegian Continental Shelf: Interpretation, **2**, SH55–SH66.

Frischknecht, F. C., and P. Raab, 1984, Time-domain electromagnetic soundings at the Nevada Test Site, Nevada: Geophysics, **49**, 981–992.

Grayver, A. V., R. Streich, and O. Ritter, 2014, 3D inversion and resolution analysis of land-based CSEM data from the Ketzin CO2 storage formation: Geophysics, **79**, E101 E114.

Hesthammer, J., A. Stefatos, M. Boulaenko, S. Fanavoll, and J. Danielsen, 2010a, CSEM performance in light of well results: The Leading Edge, **29**, 34–41.

Hesthammer, J., A. Stefatos, M. Boulaenko, A. Vereshagin, P. Gelting, T. Wedberg, and G. Maxwell, 2010b, CSEM technology as a value driver for hydrocarbon exploration: Marine and Petroleum Geology, **27**, 1872 – 1884.

Houck, R. T., A. Ciucivara, and S. Hornbostel, 2015, Accuracy and effectiveness of three-dimensional controlled source electromagnetic data inversions: Geophysics, **80**, E83–E95.

Hoversten, G. M., F. Cassassuce, E. Gasperikova, G. A. Newman, J. Chen, Y. Rubin, Z. Hou, and D. Vasco, 2006, Direct reservoir parameter estimation using joint inversion of marine seismic AVA and CSEM data: Geophysics, **71**, C1–C13.

Ivandic, M., C. Yang, S. Lüth, C. Cosma, and C. Juhlin, 2012, Time-lapse analysis of sparse 3D seismic data from the CO 2 storage pilot site at Ketzin, Germany: Journal of Applied Geophysics, **84**, 14–28.

Johansen, S., 2008, How EM survey analysis validates current technology, processing and interpretation methodology: First break, **26**.

Li, Y., and D. W. Oldenburg, 1998, 3-D inversion of gravity data: Geophysics, **63**, 109–119.

Lien, M., and T. Mannseth, 2008, Sensitivity study of marine CSEM data for reservoir production monitoring: Geophysics, **73**, F151–F163.

MacGregor, L., and M. Sinha, 2000, Use of marine controlled-source electromagnetic sounding for sub-basalt exploration: Geophysical Prospecting, **48**, 1091–1106.

McCracken, K., G. Hohmann, and M. Oristaglio, 1980, Why time domain?: Exploration Geophysics, **11**, 176–179.

Michou, L., T. Coléou, and Y. Lafet, 2013, 4D Seismic inversion on continuous land seismic reservoir monitoring of thermal EOR: 75^{th} EAGE Conference & Exhibition. (Extended Abstract).

Strack, K.-M., 1992, Exploration with deep transient electromagnetics: Elsevier Amsterdam, **373**.

Streich, R., 2016, Controlled-Source Electromagnetic Approaches for Hydrocarbon Exploration and Monitoring on Land: Surveys in Geophysics, **37**, 47–80.

Streich, R., and M. Becken, 2011, Sensitivity of controlled-source electromagnetic fields in planarly layered media: Geophysical Journal International, **187**, 705–728.

Strickland, C. E., V. R. Vermeul, A. Bonneville, E. C. Sullivan, T. C. Johnson, F. A. Spane, and T. J. Gilmore, 2014, Geophysical Monitoring Methods Evaluation for the FutureGen 2.0 Project: Energy Procedia, **63**, 4394 – 4403. (12th International Conference on Greenhouse Gas Control Technologies, GHGT-12).

Tietze, K., O. Ritter, and P. Veeken, 2015, Controlled-source electromagnetic monitoring of reservoir oil saturation using a novel borehole-to-surface configuration: Geophysical Prospecting, **63**, 1468–1490.

Um, E. S., and D. L. Alumbaugh, 2007, On the physics of the marine controlled-source electromagnetic method: Geophysics, **72**, WA13–WA26.

Wilt, M., and D. Alumbaugh, 1998, Electromagnetic methods for development and production: State of the art: The Leading Edge, **17**, 487–487.

Wright, D., A. Ziolkowski, and B. Hobbs, 2002, Hydrocarbon detection and monitoring with a multicomponent transient electromagnetic (MTEM) survey: The Leading Edge, **21**, 852–864.

Ziolkowski, A., B. A. Hobbs, and D. Wright, 2007, Multitransient electromagnetic demonstration survey in France: GEOPHYSICS, **72**, F197–F209.

Ziolkowski, A., D. Wright, and J. Mattsson, 2011, Comparison of pseudo-random binary sequence and square-wave transient controlled-source electromagnetic data over the Peon gas discovery, Norway: Geophysical Prospecting, **59**, 1114–1131.

2

FIELD SURVEY DESIGN OF A LAND CSEM SURVEY AT SCHOONEBEEK OIL FIELD, THE NETHERLANDS

Three land Controlled-Source ElectroMagnetic (CSEM) surveys were acquired at the Schoonebeek oil field in the Netherlands where steam-assisted gravity drainage (SAGD) is used as an enhanced oil recovery method. A base survey was carried out to show the potential of the CSEM method for exploration purposes and two repeat surveys for time-lapse monitoring and repeatability studies. These surveys were carried out over a period of about two years. In this chapter, we take a closer look at the Schoonebeek area and show how the field survey was designed. The measurements at Schoonebeek and the main processing steps that are repeatedly applied during the subsequent chapters are separately explained. Optimized placement of source and receivers is needed to enhance the resolution in the reservoir. This chapter also shows the studies to optimize source and receiver layout suitable for an optimal imaging and monitoring of the reservoir.

2.1. INTRODUCTION

The Controlled-Source ElectroMagnetic (CSEM) method has been developed significantly over the last decades and is known to have potential for exploration and time-lapse purposes. It is a method that shows promising results especially when used supplementary to other geophysical methods such as the seismic technique.

The research in this thesis focuses on the Schoonebeek oil field in the Netherlands where changes inside the reservoir due to steam injection can be and were monitored by both seismic and CSEM methods. In regions where the heavy-oil formation has similar acoustic properties as the injected steam or in regions with interfering pressure effects, the seismic method may be limited and thus EM measurements can provide additional information. Three land CSEM field experiments were carried out during this project between:

- 27 January - 7 February 2014,
- 17 November - 5 December 2014 and
- 16 November - 4 December 2015.

This chapter is devoted to giving an overview of the Schoonebeek site and the field survey in detail. A comprehensive explanation about the survey layout, modeling studies and the measurements at Schoonebeek is given in the next sections.

2.2. SCHOONEBEEK OILFIELD

2.2.1. DISCOVERY AND PRODUCTION

The Schoonebeek oil field is the largest onshore oil field in North-Western Europe and is located in the northeast of the Netherlands at the German border. It is part of a complexly faulted anticline. The main productive formation is the lower cretaceous Bentheim sandstone, an unconsolidated, clean, well-sorted deposit with a thickness of 10-30 m (Peksa et al., 2015). The oil field was discovered in 1943 and production temporarily stopped in 1996.

2.2.2. REDEVELOPMENT OF SCHOONEBEEK OIL FIELD VIA SAGD

In 2009, the Schoonebeek oil field was redeveloped by the Nederlandse Aardolie Maatschappij B.V. (NAM) using a new technology that combines horizontal wells with low-pressure steam injection (Jelgersma, 2007). Horizontal wells were drilled inside the reservoir at depths between 600 and 900 m below the surface leading to an increased contact of the production and injection wells with the oil-bearing rock formation (Figure 2.1), leading to the capability to pumping up more oil from each well. This was realized by deploying 40 15-meter tall high-efficiency pumps. The oil in the Schoonebeek field is viscous and thick. It contains a large quantity of paraffin which solidifies at lower temperatures. The viscosity of the paraffin is highly dependent on the temperature. Ultrapure water is heated to generate steam that is injected into the oil reservoir under low pressure to liquefy the oil before pumping it up to the surface. This is achieved by using a closely spaced pattern of horizontal oil producer and horizontal steam injector

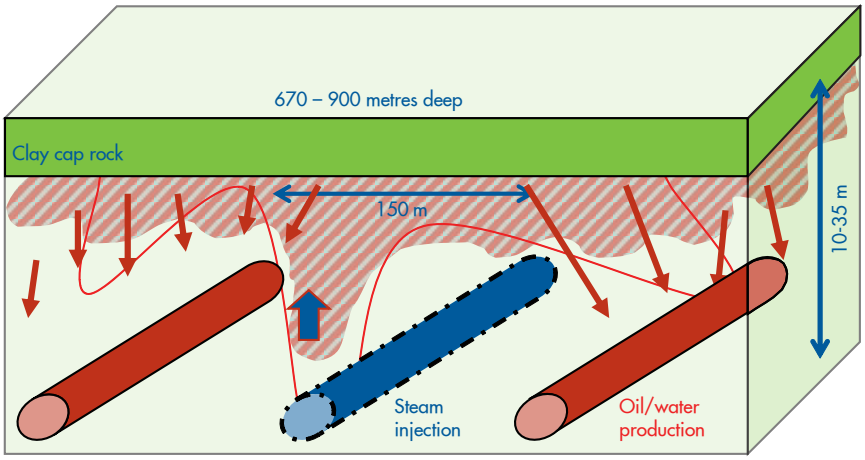

Figure 2.1: Low-pressure steam injection in horizontal wells at the Schoonebeek oil field (after NAM (2010)).

wells at distances of about 150 m from each other as shown in Figure 2.1. Steam is injected into the rock formation and rises until being hindered from rising further by the impermeable stratum sealing the oil field. On its way up, the steam heats and liquefies the oil in the reservoir. Due to gravity, the now liquefied oil slowly sinks to the bottom of the reservoir towards the two adjacent production wells where pumps extract the oil through these wells to the surface. This procedure is known as Steam Assisted Gravity Drainage (SAGD).

2.3. SEISMIC

Numerous seismic data sets were collected at the Schoonebeek oil field over the past decades. One of the first 3D seismic surveys was acquired by Shell in 1975 (Myers et al., 1992). The main reason for this early 3D survey was a discrepancy between prognosed and actual drilling results that could not be explained by conventional 2D data (Van Der Kallen and Pion, 2010). The survey was a success and led to significant improvement in structural interpretation. In 2005, as part of the Schoonebeek redevelopment project, a high-resolution baseline survey for repeat 4D seismic monitoring measurements was acquired. Its goal was to assist in monitoring production related fluid movements and to be able to acquire repeat seismic measurements in the case of unexpected production behavior. Further, causes for non-perfect repeatability of the seismic acquisition were investigated. For 4D seismic, differences in source and receiver locations were found to produce semi-coherent noise. In addition, different environmental noise and changes in the weathering layer such as variations in the ground water levels were likely to have a large influence on data quality. These results give an indication what may be expected from the repeatability measurements conducted in this thesis.

For longer term seismic measurements, a permanent seismic monitoring system is more attractive. Therefore, a permanent seismic system called SeisMovie® (Schissele et al., 2009) was installed in 2010. It consists of permanently buried receivers and sources

that can operate continuously over long periods of time. The system has the advantage to be unmanned and non-intrusive with minimal environmental impact. Its repeatability is high due to fixed source and receiver locations and it allows for continuous monitoring at any moment in time. One disadvantage is that daily variations in the subsurface are hard to correct for. After a 2D trial (Hornman et al., 2012), a 3D system was installed in 2012 with 36 high-repeatable SeisMovie® sources at 25 m depth and five lines of 68 receiver stations (Hornman and Forgues, 2013). Technically, the survey was a success since the progress of the steam front could be monitored with surprising detail and thus showed the potential of this method. The main disadvantage of this system was its costs and that it was economically not sustainable for a field like Schoonebeek and therefore cheaper options are needed. In this thesis, results and structural information obtained from the seismic surveys are used as input in the 3D CSEM inversion.

2.4. CSEM DATA ACQUISITION AND PROCESSING

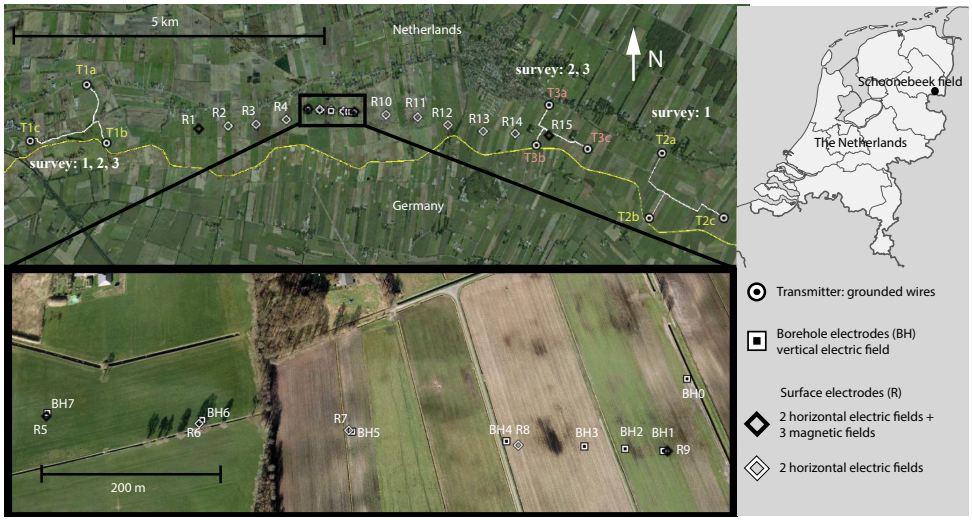

Figure 2.2: EM-source and -receiver locations at Schoonebeek.

Because of its steam injection, the Schoonebeek oil field was seen as a suitable case for (time-lapse) surveying with the CSEM methodology. Schoonebeek is a rather large field, and an area south of the town of Schoonebeek close to the border to Germany was chosen for the CSEM survey (Figure 2.2) because that area is co-located with the SeisMovie® survey and is in addition the area where the reservoir is at its shallowest depth.

To measure the horizontal electric-field components and the magnetic-field components, receivers were placed at the surface as shown in Figure 2.3. What is not common is to measure the vertical electric-field component and that was done by placing electrodes in shallow boreholes (Figure 2.4). Although measuring the 5 components at each station was possible, it was decided to measure the electric field at each station while

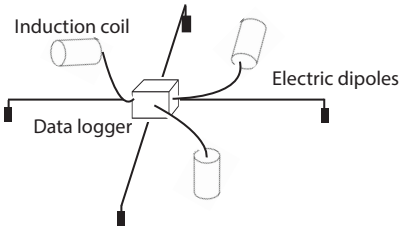

Figure 2.3: Sketch of a 5-component (2 E-field and 3 B-field) receiver station at surface.

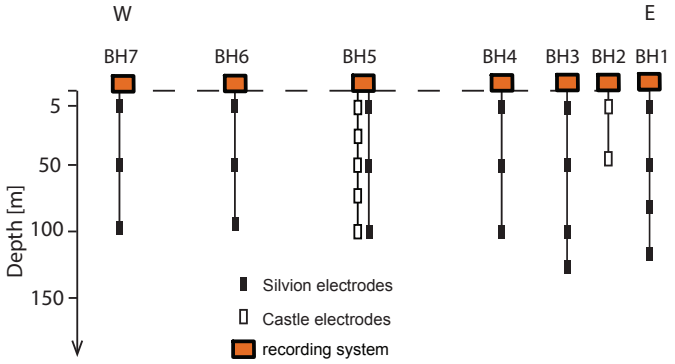

Figure 2.4: Section view of vertical electrodes.

measuring the magnetic field only at a few of the stations. This approach is based on the experience and observation from other field acquisitions that (i) the magnetic field usually varies much more smoothly in space and is less noisy than the electric field and (ii) the magnetic field typically is far less sensitive to resistive reservoirs than the electric field. These observations are related to the fact that the time derivative of the magnetic field is measured with coils, which do not suffer from the static EM field of the earth. Reducing the number of measurement points of the magnetic field has the added advantage that the costs due to deploying magnetic coils (installation, maintenance and power supply) and its post-survey processing are reduced.

The setup on the source side consists only of electric-field dipoles, as commonly used nowadays in CSEM for imaging resistive reservoirs. Typical land electric-field sources have a length on the order of 1 km, long enough to get sufficient power into the ground and small enough to have sufficient resolution. Laying those out at the Earth's surface poses logistical challenges in populated regions, so also near Schoonebeek. Two transmitter locations, east and west of the receiver stations, were chosen. The transmitter cables were laid out along vehicle-accessible tracks in approximately T-shaped geometries to get a uniform azimuthal distribution of the CSEM source fields.

2.4.1. INSTRUMENTATION

Instrumentation for marine magnetotelluric and CSEM sounding was described earlier (Constable, 2013). For land surveys, however, instrumentation differs and multiple different approaches to measure the electromagnetic field have been applied throughout the years (Streich, 2016).

ELECTRODE CHOICES

Although electrodes were used for monitoring purposes earlier, no literature was found which electrodes would be most suitable for CSEM monitoring on land, including the possibility for electrodes in shallow boreholes (under the water table). One main requirement is that the electrodes need to be non-polarizable. Therefore, two different type of electrodes, the copper-copper sulphate electrode ($Cu/CuSO_4$) used in land magnetotelluric (MT) and the silver-silver chloride electrode (Ag/AgCl) commonly used in marine EM and land MT, were initially considered. $Cu/CuSO_4$ electrodes are known to be more noisy than the Ag/AgCl ones (Perrier et al., 1997) such that we focused in an early stage on different types of Ag/AgCl electrodes. As Ag/AgCl electrodes, 3 types were considered, namely the ones from the company Silvion, from the company Castle and from the research institute Scripps. Although tests have taken place with these electrodes in some institutes, the results were kept internally and also were not conclusive for monitoring applications. The Silvion electrodes have a higher contact area than the Castle electrodes while the Scripps electrodes have the highest contact area due to their entire plastic housing being porous. Silvion electrodes seem to have the lowest noise and smallest drift over a few weeks, but also seem to show significant decay over time. This decay over a period of about a year was found out only after deployment in the boreholes. Castle and Scripps electrodes seemed to perform about identically. Finally, a design issue was that the Scripps electrodes are not made for use in boreholes.

As borehole receivers, it was decided to use WE200 electrodes from Silvion and for

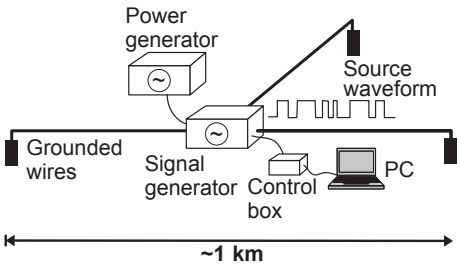

Figure 2.5: Sketch of CSEM source (after Streich et al. (2010))

comparison purposes a few LD25 electrodes from Castle. Finally, 32 WE200 and 3 LD25 electrodes were purchased. As surface receivers, the Ag/AgCl electrodes developed by GFZ Potsdam were used.

RECORDING-INSTRUMENT CHOICES

Two different recording systems were used for the field tests. The recording system used for all surface stations and a few borehole stations was the short-period automatic magnetotelluric (SPAM Mk. IV) data acquisition instrument developed by the German Research Centre for Geosciences (GFZ; Klose et al. (2011)). For the majority of the borehole stations, the Metronix ADU-07e (Analog Digital Unit) systems were used. The source signal was recorded by both an ADU and a SPAM system to allow for proper processing of the recorded data.

TRANSMITTER CHOICES

A three-phase CSEM transmitter developed by Metronix GmbH and the German Research Centre for Geosciences (GFZ) was used for the three surveys (Figure 2.5). The CSEM transmitter is powered by a 400 V generator that supplies three-phase 50 Hz alternating currents. The currents are fed into a high-power, high-voltage programmable signal generator. The source uses tripoles such that the direction of the signal can be steered by feeding three currents with a fixed phase relationship into three grounded electrodes. The overall source polarization can be adjusted by simply applying a constant phase shift to the three source currents. We refer to this phase shift as the source polarization angle. As a result, multipolarization fields can be generated for a fixed transmitter geometry simply by electronically adjusting the polarization angle. Multipolarization fields have the advantage to allow for uniform subsurface illumination, i.e., for every source polarization, certain azimuth ranges from the source exist where the amplitude of the CSEM source field is very low. By using several polarizations, it can be ensures that fields of measurable amplitude are generated at all azimuths. That feature gives more flexibility for the field set-up and may allow for a reduced number of strategically chosen source locations compared to standard dipole sources. For a mathematical explanation of how the source is able to generate multiple current polarizations without physically moving the source as well as for details about technical specifications of the transmitter and response function calculation, the reader is referred to the appendices of Chapter 3.

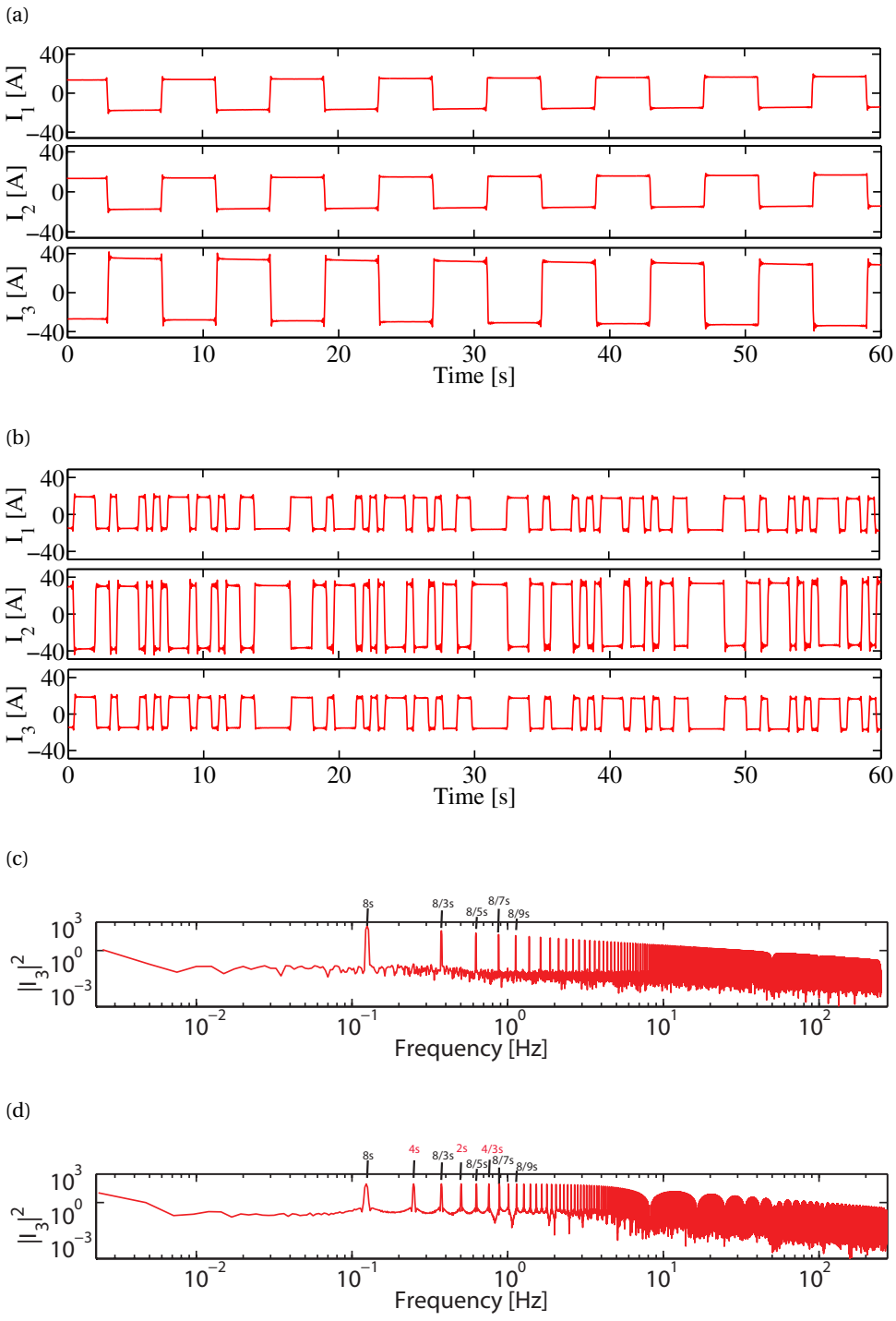

Figure 2.6: (a) Examples of square-wave source currents of 8s injected through the three source electrodes. Current amplitudes are nearly 40 A and the three currents sum up to zero. (c) Power spectrum for current I_3, showing well-defined peaks at the fundamental frequency and odd harmonics up to the Nyquist frequency of the recording device. (b) Example of a 8-s PRBS-31 signal. (d) Power spectrum for current I_3, showing peaks also at the position of the even harmonics.

The transmitter can be fed with different source signals: (1) Square-wave signals where the transmitted energy is focused in narrow frequency bands. In previous field surveys at Ketzin (Germany), square-wave signals with different source base frequencies were used and were capable to adequately image a resistive target at about 1 km depth; (2) Complex waveforms can be designed to spread the transmitted energy across a band of discrete frequencies in a more even manner than the linear amplitude decrease of the traditional square wave, such as the pseudo-random binary sequences (PRBS) that approximate the spectra of white noise. An example of transmitted currents is shown in Figure 2.6. Figure 2.6a, c shows the time series and the corresponding power spectrum for an 8-s square wave signal and Figure 2.6b, d shows the time series and the corresponding power spectrum for a 8-s PRBS-31 signal. It can be seen that the sum of the three currents is zero at all times because of the 120° phase shifts between the three currents (Figure 2.6a, b).

PRBS signals of fairly low order were used (sequence length of 31 or 63 points) that do not need much more recording time compared to square-wave signals. Other waveforms can be used as well (Mittet and Schaug-Pettersen, 2008; Myer et al., 2011). Myer et al. (2011) created different waveforms that were designed to put more power into specific harmonics than the fundamental frequency. During the main part of our survey either a square wave or a PRBS source current was fed into the ground through the three source electrodes.

The sensitivity of the CSEM method to variations in the subsurface differs on the basis of the applied frequency. The maximum acquisition ranges for these frequencies, however, are constrained due to the increase in attenuation with frequency. Thus, to acquire useful CSEM data, we focus on different base frequencies of 1/16 Hz, 1/8 Hz, 1/4 Hz, 1/2 Hz and 2 Hz. Whereas low frequencies penetrate over longer distances and deeper, higher frequencies add higher-resolution information at shorter offsets and shallower depths. With source fundamental periods of $16 - 4$ s, we get strong signal at those frequencies, but fairly weak signal at higher frequencies (see wavelet spectrum in Figure 2.6c). By also transmitting at fundamental frequencies of 1/2 Hz and 2 Hz, we get stronger signal and more signal to stack at those frequencies.

CHOICE FOR (BASIC) SURVEY LAYOUT

For monitoring applications, it is essential to place sources and receivers at locations that optimally resolve the target area and optimally show the very subtle changes in the subsurface. At Schoonebeek these are confined to the target region at about 700 m depth. The source and receiver positions were chosen such that the source-receiver offsets for the borehole receiver is optimal, in the following sense:

- Receivers that are placed too close to the source cannot be used due to complex near-source characteristics and due to the fact that close to the source the direct field is primarily measured and therefore the data hardly contain subsurface information;

- Receivers that are placed too far away from the source suffer from low signal-to-noise ratios.

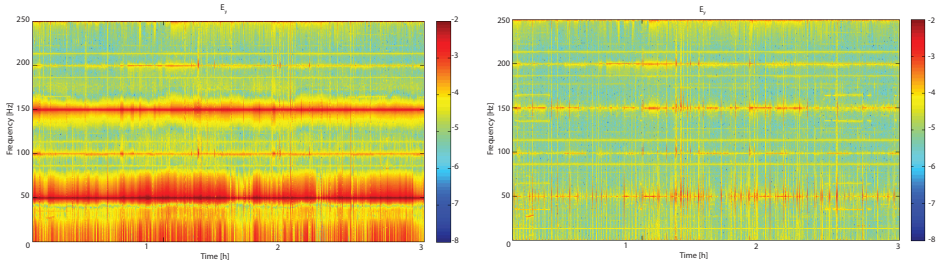

(a) (b)

Figure 2.7: Frequency spectrum before (a) and after (b) 50-Hz notch filtering.

With this in mind, the optimal offset was studied considering electric-field amplitudes and a minimal offset of at least 2 km for the vertical-electric field measurements. (For details the reader is referred to Chapter 5.) The best sensitivity to reservoir changes for the vertical electric-field component, while maintaining acceptable signal amplitudes, was found from synthetic studies at source-receiver offsets between approximately 3 and 5 km.

Analysis of the base-survey field data, however, showed that signal-to-noise ratios were too low at one transmitter location about 5 km from the vertical electric-field receivers. Therefore one source location had to be moved closer to the borehole receivers for both repeat surveys. Since the obtained source-receiver offsets were optimized for the borehole receivers, some of the surface receivers, especially at the far end of the receiver line in the east are too close to the Eastern transmitter side and could not be used while the transmitter was operating.

Modeling studies showed that the reservoir response for the vertical electric-field component is clearer when the receivers are buried deeper, closer to the reservoir (Colombo and McNeice (2013) and Chapter 5). Thus borehole receivers were planted as deep as possible or as deep as economically feasible.

2.4.2. DATA PROCESSING

The data were processed to obtain frequency-dependent response functions (also often called transfer functions in magnetotelluric (MT) processing) between the source and receivers that can be used as input for inversion. A response function describes the mathematical relationship between an input process (e.g., source currents) and an output process (e.g., EM field) with the Earth regarded as a linear system that responds to the input process via the output process. Because the system is linear, the response function does not depend on the amplitude of the input process (i.e., the source currents for a CSEM survey). The estimation of the response functions is usually hindered by noise. If the noise level has a Gaussian distribution or is low, then a least-square estimation is sufficient. In areas with high or non-Gaussian distributed noise levels such as the Schoonebeek oil field, however, a robust processing scheme is necessary to down-weight outliers in the data.

For the data processing, we used a software from Shell based on a robust processing

scheme, a technique routinely used for MT processing to reduce the influence of noise (e.g., Egbert and Booker, 1986;Chave and Thomson, 1989;Ritter et al., 1998;Streich et al., 2013). As processing sequence, we used:

- 50-Hz notch and high-pass filtering;
- Stacking;
- Calculation of bivariate response functions by combining and deconvolving the source currents

With this processing sequence, we obtained the response functions, as defined by Streich et al. (2013). These response functions were subsequently inverted to subsurface resistivity distributions.

We will briefly discuss each of these steps, starting with the 50-Hz notch filtering. The 50-Hz notch filter suppresses 50-Hz signals and its associated harmonics, generated by the (urban) environment and the system itself. The filtering was done in the time domain on all receiver data and transmitter signals using identical filters with identical filter parameters. We use the 50-Hz notch filter mainly for time-domain display purposes and we are aware that for frequency-domain inversions this filter is unnecessary since the frequencies of interest are all below 10 Hz. The result of the notch filter can be seen in Figure 2.7. The 50-Hz and 150-Hz noise are clearly filtered out. Further, it shows that some parts of the low frequency data, in the band 0 – 50 Hz, are filtered. This might be due to the fact that the filter operates in the time domain and that the very strong 50-Hz signal might be subject to longer periodic oscillations leading to an additional change in the spectrum at low frequencies. The high-pass filter removes signals at frequencies lower than the primary source frequency.

Subsequently, the data was cut into time windows as long as the source period. The data were then Fourier transformed, the spectral components (Fourier coefficients) excited by the source extracted (i.e., the fundamental frequency and odd harmonics for square-wave signals), and the measured responses of the recording instruments and sensors deconvolved. Since neighboring frequencies will provide similar response functions (Weidelt, 1972), data reduction is achieved by robustly stacking data falling within particular spectral bands using a logarithmic frequency binning as is commonly done in MT processing.

In calculating response functions, data from different source periods and polarizations were combined. The calculation effectively deconvolved the source currents, while not accounting for the source geometry or length of source wires. So-called bivariate response functions were obtained by choosing two of the three measured source currents fed into the three source electrodes. The third current is linearly dependent on those two, yet the choice of currents may influence response function quality due to noise characteristics of the data. Mathematical details about the calculation of bivariate response functions can be found in Chapter 3 in Appendix B and in Streich et al. (2013).

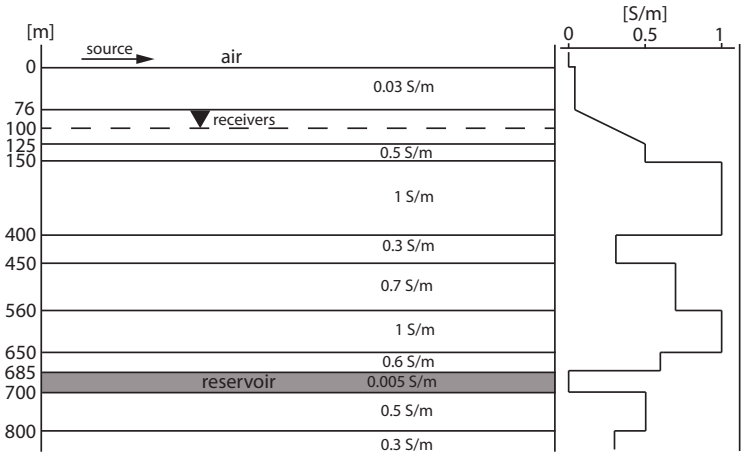

Figure 2.8: Layer model and conductivity profile (in S/m) of Schoonebeek area derived from logging data. The source represented by the black arrow is placed at the surface, and receivers are placed at a depth of 100 m. The conductivity profile is plotted in linear scale to better indicate the conductivity changes of the layers above the strongly resistive reservoir layer.

2.5. SURVEY-RELATED MODELING STUDIES

2.5.1. MAIN GOALS

Modeling is crucial to design a field survey that focuses on a specified target area. Roux and Garcia (2014) recently developed a statistical experimental design algorithm to optimize a CSEM land experiment and to maximize the information about the reservoir layer (Roux and Garcia, 2014). We do not take such an approach and focus on different scenarios to test the influence of survey-design parameters on the final inverted images.

The main goals of the modeling studies are to:

1. Derive a geophysical model for Schoonebeek using information obtained from recent and old well logging data (Figure 2.8);
2. Optimize the field acquisition layout, i.e., optimal source and receiver locations, and optimal depth of the receivers in the shallow boreholes;
3. Quantify the sensitivity of the vertical electric-field component for Schoonebeek and compare them to horizontal electric-field component sensitivities;
4. Quantify the effects of subsurface changes, i.e., time-lapse effects; and
5. Quantify the influence of borehole deviation from verticality on the vertical electric-field data.

We will discuss each item briefly, starting with deriving a resistivity model that can be used for the modeling. The geology of the subsurface and the target region, the reservoir, at Schoonebeek are well known from numerous well logs, drill cores and 3D seismic reflection data. For our modeling studies, we approximate the area as consisting

of horizontally-plane layers with a shallow reservoir at 685-700 m depth (Figure 2.8) although we are aware that detailed geological maps of the region, its structure based on 3D seismic reflection data, show that the reservoir is not horizontally layered but varies from 700 m depth at the center of our survey to about 900 m depth some 5 km towards the west and east. Since the survey array has highest sensitivity to the region around the middle of the receiver array (as shown in Chapter 3), the plane-layered assumption may be justified for these synthetic studies.

With regard to the second point above: The modeling was done for receiver depths: 5, 50, 100 and 150 m and for frequencies between 0.1 and 10 Hz which is a realistic range for field data.

With regard to the points 3, 4 and 5 above: The modeling study related to time-lapse effects is discussed in Chapter 4 and the sensitivity study and modeling related to the vertical electric field is discussed in Chapter 5.

2.5.2. SENSITIVITY COMPARISON OF 2D VERSUS 3D GEOMETRY

In this section, we briefly discuss the influence of additional cross-line source and receiver positions and analyze the effect of choosing a rather limited acquisition setup with only (approximately) in-line source and receiver positions. The choice of in-line source and receiver positions was initially chosen for validation and integration of "standard" EM data with vertical E-field data from shallow boreholes. To that aim, two transmitter locations and 15 surface receiver stations were chosen (see section 2.4 of basic layout). We aim for a field setup to show the feasibility of vertical electric-field measurements and repeatability. To avoid repetition of this discussion, details about 1D and 3D inversion are not given in this chapter, but will be discussed in the following Chapter 3.

We will start by showing two subsurface models that have small resistive and conductive bodies included into the reservoir layer to simulate a complex resistivity distribution. Then we determine a sensitivity at reservoir depth due to our choices of source and receiver positions. We will use our basic layout, as given in subsection 2.4. Either we add two extra transmitter positions in the cross-line direction or receiver stations in the cross-line direction. The results of each of these configurations on the sensitivity of recognizing the small bodies in the reservoir layer will then be compared and evaluated.

Figure 2.9 shows 3D inversion results for the basic acquisition setup (used throughout the thesis), a setup with additional source locations and a setup with an additional perpendicular receiver line. Two scenarios are distinguished: two highly resistive bodies of 1 km × 1 km separated by 500 m with ρ_v = 1000 Ωm; $\rho_h = \rho_v/2$ (Figure 2.9a) and a complex model with two highly resistive blocks and two blocks more conductive than the background reservoir and of different shapes with $\rho_{v,1}$ = 1000 Ωm, $\rho_{v,2}$ = 100 Ωm and $\rho_h = \rho_v/2$ (Figure 2.9b). Figures 2.9c and 2.9d show the inversion results at a depth level of 785 m. The boundaries of the objects after inversion, indicated by black dashed lines, were in the following defined such that they coincide with a resistivity contrast of 10% from the background resistivity. Anomalies with small separation are difficult to resolve. The two blocks are too close to each other to obtain two separate resistivity maxima. The complex scenario with four bodies might be detectable and can be partly resolved horizontally and vertically. Both inversions terminate short of the actual resistivity values.

Two additional sources north and south of the receiver line are added in Figures 2.9e

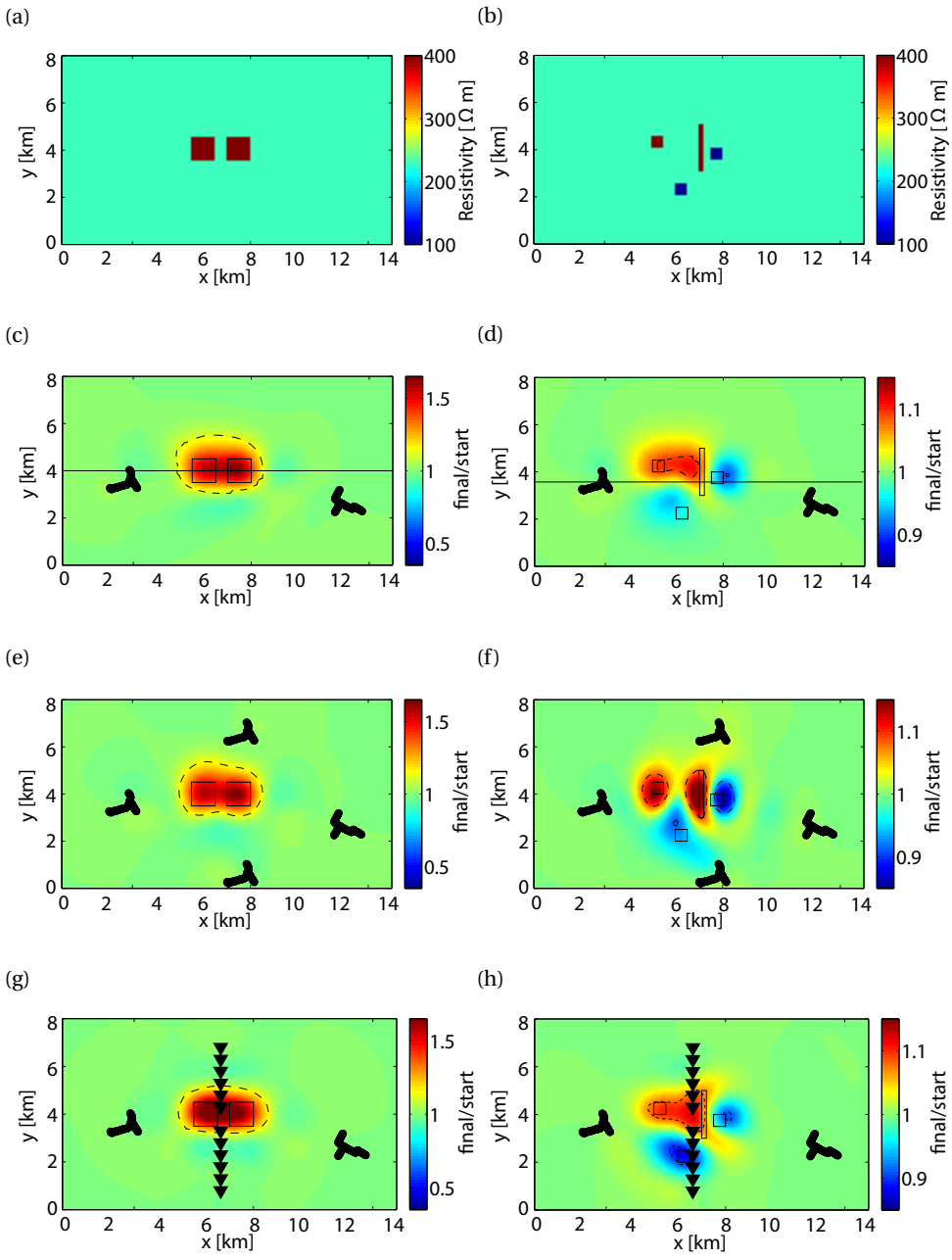

Figure 2.9: 3D inversion results of the models shown in (a) and (b) for the basic acquisition setup (c) and (d); for a setup with additional source locations (e) and (f) and for a setup with an additional receiver line perpendicular to the existing one (g) and (h). The black rectangles indicate the borders of the inserted bodies and the black dashed lines indicate the borders of the inserted bodies after inversion. Receiver locations of the basic setup not shown since they would mask the inversion results. For better visibility the ratio between the inverted and the starting resistivity model is plotted.

and 2.9f showing that especially for the four block scenario, each block may be resolved separately. Additional receivers cross-line to the receiver line (Figures 2.9g and 2.9h) hardly result in any resolution improvement apart from the two bodies that were placed outside the receiver plane. Although two additional sources would help in resolving or detecting the shape of the blocks, the main aim of the field surveys was evaluating the use of E_z-field measurements via electrodes in shallow boreholes, and later the effects of repeatability so the lack of resolution outside the receiver plane was not of main concern. All in all, small and complex structures might be detectable, but not well resolvable in size and amplitude.

To be able to resolve resistive or conductive structures around the reservoir depth, the survey geometry has to be chosen such that the sensitivity to this depth range is sufficiently high. We use the cumulative sensitivity and define it as a weighted ℓ^2-norm resulting in a single sensitivity value for every model parameter:

$$C(m_i) = \Big(\sum_{j=1}^{n} |W_{d_j} \frac{\partial F_j(m)}{\partial m_i}|^2 \Big)^{\frac{1}{2}} \tag{2.1}$$

where n is the number of all data points j (counted over sources, source polarizations, receivers and frequencies); $F_j(m)$ is the electromagnetic field at data point j, $\frac{\partial F_j(m)}{\partial m_i}$ is the Fréchet derivative of the data with respect to the model parameter m_i and $W_{d_j} = \frac{1}{F_j(m)+\epsilon}$ are data weights with $j = 1, ..., n$ with ϵ being the absolute error floor: $\epsilon = 10^{-10}$ V/m. The cumulative sensitivities are normalized by their maximum value; for more details the reader is referred to Chapter 3.

Horizontal-sensitivity sections are depicted in Figure 2.10. The corresponding survey geometry is indicated by the black lines (position of the sources) and black triangles (position of the receivers). In Figure 2.10a the logarithm of the normalized cumulative sensitivity at a depth level of 685 m is plotted, showing a high-sensitivity region between both transmitters and within an approximately 2-km wide corridor around the receiver locations, indicating that structures close to the receiver line should be resolvable. Adding a receiver line perpendicular (Figure 2.10b) broadens the area where the survey geometry is sensitive to but does slightly decrease the sensitivity amplitude compared to Figure 2.10a. Additional sources, as shown in Figure 2.10c, lead to a broadening of the area where the survey geometry is sensitive to while preserving sensitivity amplitudes.

As will be presented in Chapter 3, the sensitivity to the reservoir is high because of its high overall resistivity. This demonstrates that the survey geometry is sensitive to the reservoir layer and thus targets inside this layer may be detectable and resolvable. A major aspect that influences the resolution is man-made EM noise. Data deteriorated by EM noise will be discussed in detail in Chapter 3 by assessing the impact of field noise on resolution using uncertainties estimated from real data.

In Chapter 3 the 3D inversion performance of the chosen acquisition design is evaluated by testing the ability to resolve small and complex structures.

2.6. CONCLUSIONS

We showed that a sparse source receiver configuration consisting of a single receiver line of 15 receivers with a length of about 6 km and two transmitters approximately in-line

(a)

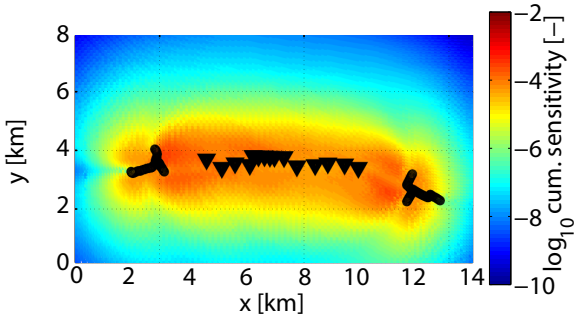

(b)

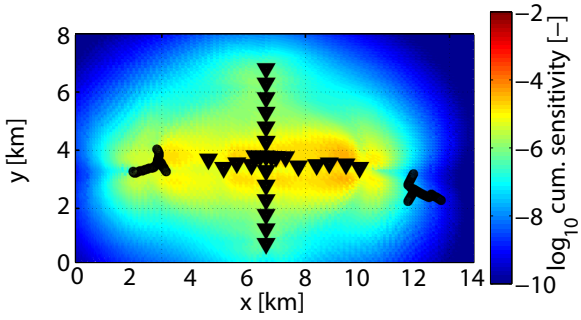

(c)

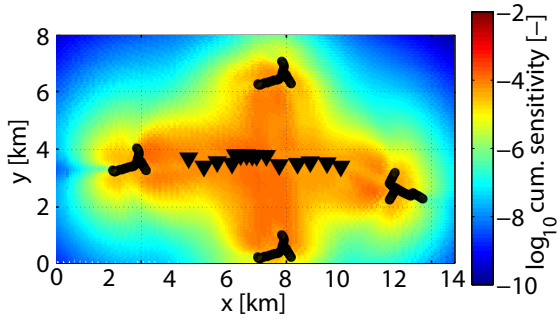

Figure 2.10: Depth section at reservoir level of normalized cumulative sensitivity for (a) line-survey geometry, (b) geometry with added cross-line receivers and (c) geometry with two additional sources. Black lines indicate the position of the sources and black triangles indicate the position of the receivers.

with the receiver positions is sensitive to and may give a good prediction about the resistivity distribution inside a reservoir within a corridor of roughly 2 km width around the receiver plane. Therefore this setup was seen as suitable for validating and evaluating the use of vertical electric-field measurements in shallow boreholes. This setup further proves to resolve resistive and conductive features that may be introduced by injection fluids. Whereas resistive bodies can be recognized and located by assuming good knowledge of the background resistivity, their extent and resistivity cannot be resolved accurately, especially for small bodies inside the reservoir. The bodies' resistivities are smeared over large volumes of lower than the actual resistivity. In order to better constrain the boundaries of 3D bodies, additional source positions perpendicular to the receiver line may give additional coverage resulting in improved resolution. Limitations in survey geometry lead to a decrease in resolution away from the receiver line and stronger smoothing of complex structures.

REFERENCES

2010, Redevelopment of the Schoonebeek oil field. (flyer published by Nederlandse Aardolie Maatschappij B.V. (NAM), www.nam.nl).

Chave, A. D., and D. J. Thomson, 1989, Some comments on magnetotelluric response function estimation: J. Geophys. Res, **94**, 215–14.

Colombo, D., and G. McNeice, 2013, Quantifying surface-to-reservoir electromagnetics for waterflood monitoring in a Saudi Arabian carbonate reservoir: Geophysics, **78**, E281–E297.

Constable, S., 2013, Review paper: Instrumentation for marine magnetotelluric and controlled source electromagnetic sounding: Geophysical Prospecting, **61**, 505–532.

Egbert, G. D., and J. R. Booker, 1986, Robust estimation of geomagnetic transfer functions: Geophysical Journal International, **87**, 173.

Hornman, J. C., J. van Popta, J. L. Lopez, H. Dijkerman, et al., 2012, Continuous monitoring of thermal EOR at Schoonebeek for intelligent reservoir management: Presented at the SPE Intelligent Energy International, Society of Petroleum Engineers.

Hornman, K., and E. Forgues, 2013, Permanent reservoir monitoring with onshore surface seismic: Presented at the Second EAGE Workshop on Permanent Reservoir Monitoring 2013–Current and Future Trends.

Jelgersma, F., 2007, Redevelopment Of The Abandoned Dutch Onshore Schoonebeek Oilfield With Gravity Assisted Steam Flooding: Presented at the IPTC 2007: International Petroleum Technology Conference.

Klose, R., G. Schmidt, O. Ritter, and G. Dawes, 2011, What is SPAM four for?: Protokoll über das 24. Schmucker-Weidelt-Kolloquium für Elektromagnetische Tiefenforschung, 24. Schmucker-Weidelt-Kolloquium für Elektromagnetische Tiefenforschung (Neustadt a. d. Weinstraße 2011), 127–134.

Mittet, R., and T. Schaug-Pettersen, 2008, Shaping optimal transmitter waveforms for marine CSEM surveys: Geophysics, **73**, F97–F104.

Myer, D., S. Constable, and K. Key, 2011, Broad-band waveforms and robust processing for marine CSEM surveys: Geophysical Journal International, **184**, 689–698.

Myers, R., E. Rijks, et al., 1992, Optimization of Field Development Through Early Acquisition of 3D Seismic: Presented at the International Meeting on Petroleum Engineer-

ing, Society of Petroleum Engineers.

Peksa, A. E., K.-H. A. Wolf, and P. L. Zitha, 2015, Bentheimer sandstone revisited for experimental purposes: Marine and Petroleum Geology, **67**, 701 – 719.

Perrier, F. E., G. Petiau, G. Clerc, V. Bogorodsky, E. Erkul, L. Jouniaux, D. Lesmes, J. Macnae, J. M. Meunier, D. Morgan, D. Nascimento, G. Oettinger, G. Schwarz, H. Toh, M. J. Valiant, K. Vozoff, and O. Yazici-Cakin, 1997, A One-Year Systematic Study of Electrodes for Long Period Measurements of the Electric Field in Geophysical Environments: Journal of geomagnetism and geoelectricity, **49**, 1677–1696.

Ritter, O., A. Junge, and G. J. Dawes, 1998, New equipment and processing for magnetotelluric remote reference observations: Geophysical Journal International, **132**, 535–548.

Roux, E., and X. Garcia, 2014, Optimizing an experimental design for a CSEM experiment: Methodology and synthetic tests: Geophysical Journal International, **197**, 135–148.

Schissele, E., E. Forgues, J. Echappé, J. Meunier, O. De Pellegars, and C. Hubans, 2009, Seismic Repeatability–Is There a Limit?: Presented at the 71st EAGE Conference and Exhibition incorporating SPE EUROPEC 2009.

Streich, R., 2016, Controlled-Source Electromagnetic Approaches for Hydrocarbon Exploration and Monitoring on Land: Surveys in Geophysics, **37**, 47–80.

Streich, R., M. Becken, and O. Ritter, 2010, Imaging of CO2 storage sites, geothermal reservoirs, and gas shales using controlled-source magnetotellurics: Modeling studies: Chemie der Erde - Geochemistry, **70**, 63–75.

———, 2013, Robust processing of noisy land-based controlled-source electromagnetic data: Geophysics, **78**, E237–E247.

Van Der Kallen, A., and J. Pion, 2010, 35th anniversary of the first land 3D survey by NAM and Shell: The Leading Edge, **29**, 800–805.

Weidelt, P., 1972, The inverse problem of geomagnetic induction: J. Geophys., **38**, 257–289.

3

3D INVERSION OF LAND-BASED CSEM SURVEY

Controlled-source electromagnetic data is sensitive to the subsurface resistivity distribution, but 3D inversion results are ambiguous and in-depth interpretation is challenging. Resolution and sensitivity analysis as well as the influence of noise on resolution have been used to quantify 3D inversion performance. Based on these numerical studies, a land-based controlled-source electromagnetic survey was designed and carried out at the Schoonebeek oil field, the Netherlands. The acquired data were processed and subsequently inverted for the resistivity distribution. Both 1D and 3D inversion of horizontal electric-field data show the reservoir at the right depth, matching well-log data without using a-priori knowledge about the actual reservoir depth. We used a 1D model with a fine layering as starting model for 3D inversion. Synthetic data inversions and sensitivity tests demonstrate that resistive or conductive bodies inside the reservoir zone may be well detectable with our proposed limited acquisition geometry. Spatial variations in reservoir resistivity are visible in the measured data and after inversion by assuming good knowledge of the background resistivity distribution. Reservoir resistivity and size, however, have to be interpreted with care considering the intrinsically low resolution of EM which is further reduced by man-made EM noise.

This chapter has been published in Geophysics as *Schaller, A.M., Streich, R., Drijkoningen, G.G., Ritter, O., Slob, E.C., 2017, A land-based CSEM method for oil field exploration: An example from the Schoonebeek oil field: Geophysics. 2017 Nov 13;83(2):1-71.*

3.1. INTRODUCTION

Since the first survey of an oil field offshore Angola using marine controlled-source electromagnetic (CSEM) sounding for determining the absence or presence of hydrocarbons in a known reservoir (Ellingsrud et al., 2002), the CSEM method has gained a lot of interest in the industry. The marine CSEM method is generally recognized to give additional information and is especially applied for hydrocarbon exploration, primarily with the objective to derisk drilling activities (e.g., Darnet et al., 2007; Constable, 2010; Fanavoll et al., 2014). Whereas in marine CSEM surveys dense 2D profiles or complex 3D grids with tens of transmitter tow lines and hundreds to thousands of receiver deployments is feasible (Constable, 2010), such source and receiver coverage is very difficult to achieve for terrestrial surveys because of various logistical constraints (access restrictions, urbanization, presence of infrastructure and noise sources) and typically limited equipment availability. In addition, deploying sources of sufficient strengths is difficult. In contrast to the marine case where the transmitter is situated in the most conductive area, the sea water, land transmitters are usually situated on the earth's surface and the source electrodes are deployed in a medium much more resistive than sea water, which limits achievable source current amplitudes. Further, more near-surface heterogeneities exist on land than at the sea floor and near-electrode heterogeneities can result in more complex electric-field patterns.

Although electromagnetic methods were initially developed on land (Streich, 2016), the mentioned problems and challenges of land EM make it difficult to replicate the marine EM exploration success on land. To date, the seismic method is the principal geophysical method that is routinely applied for hydrocarbon exploration on land. The seismic wave-propagation method provides higher resolution than the diffusive CSEM method. However, CSEM methods have the advantage to be sensitive to resistive objects and to spatial variations in the resistivity. They provide generally higher resolution than potential-field methods such as gravity (Li and Oldenburg, 1998; Dell'Aversana et al., 2012). Large-scale EM surveys are not commonly carried out, but many wells exist with resistivity logs. Gathering additional EM data would provide knowledge of the resistivity distribution inside an oil or gas field, which is essential to evaluate its processes during hydrocarbon production or steam injection.

Numerical feasibility studies on land exist (Wirianto et al., 2010) and show that subsurface responses are weaker compared to marine CSEM responses, and are more complicated to interpret due to near-surface inhomogeneities. Up to now, only a few academic EM surveys, and a small number of industry surveys were conducted, which can be considered technology trials rather than commercial surveys (e.g., Streich and Becken, 2011; Grayver et al., 2014; Streich, 2016; Tietze et al., 2015). Grayver et al. (2014) showed that for a land CSEM survey it is possible to get good 3D inversion results consistent with regional geology. They deployed 39 five-component receivers along an 11 km long line centered at a CO_2 injection site and 8 CSEM transmitters well-distributed around the area. Several 3D inversion algorithms have been developed over the last decade to reconstruct resistivity models from marine and land EM data (e.g., Plessix and Mulder, 2008; Commer and Newman, 2008; Grayver et al., 2013; Oldenburg et al., 2013; Schwarzbach and Haber, 2013; Zhdanov et al., 2014). A recent review of the latest developments can be found in Newman (2014).

In this work, we study the applicability of land CSEM for recovering the resistivity distribution inside a hydrocarbon reservoir by 1D and 3D inversions. The underlying mathematical theory of EM inversion is well established, but the practical application to real data requires thorough analysis of uncertainties in the inversion result. Therefore, we numerically investigate resolution capability in terms of the survey geometry, noise distortion, reservoir depth and resistivity distribution inside the reservoir. We use a deterministic inversion approach, in which gradients derived from the forward-model process are used to update a sequence of models. Receivers are either inverted separately or together and their inversion results are compared. Based on the results of the analysis, a target-oriented land CSEM acquisition field setup was designed for the Schoonebeek region in the Netherlands where steam is injected into an oil-bearing reservoir at a depth of ~700 m for enhanced oil recovery. The obtained data were inverted for the resistivity distribution inside the reservoir where the injected steam may lead to more complex resistivity patterns close to the injector and producer wells. We show how a sparse source-receiver configuration has the potential of resolving complex resistivity patterns inside the reservoir zone. Further, we discuss to what extent small-scale variations of resistivity can be detected.

3.2. INVERSION ALGORITHMS

3.2.1. 1D INVERSION

We try to find a model for which we can compute data that will best fit the measured data. Finding this best fitting model requires iterative (forward) modeling where after every iteration the model can be updated. This was done using a reflectivity forward modeling code (Streich and Becken, 2011; Streich et al., 2011). To minimize the number of iterations necessary to find the best fitting model we use a Gauss-Newton type method to compute model updates based on an objective function that we seek to minimize. The objective function is given by

$$f_{1D} = \|\mathbf{W_d}(\mathbf{d} - F(\mathbf{m}))\|^2 + \mu\|\mathbf{W_m}(\partial_\mathbf{z}(\mathbf{m} - \mathbf{m_0}))\|^2 \tag{3.1}$$

where the first term is the misfit of the model's computed response $F(\mathbf{m})$ to the data $\mathbf{d}$ that are the real and imaginary parts of the measured electric-field data. The data vector $\mathbf{d}$ can contain data from multiple transmitters, receivers, and frequencies. The data weights are defined as $\mathbf{W_d} = diag(w_i)$, where the weights w_i are calculated by multiplying error estimates with the absolute value of the data. They weigh the relative contribution of each datum to the misfit. Data with large errors are down-weighted to limit their influence, whereas data with small errors will have a larger impact on the total misfit. The second term is a norm of the model roughness and is computed by applying a differencing operator $\partial_\mathbf{z}$, a matrix of first derivatives with respect to depth, to the elements of the model vector $\mathbf{m}$. $\mathbf{m_0}$ is a reference model, e.g. the starting model. We use a bounded logarithmic transform of the conductivity $\sigma_{h,v}$ to the model parameters (Grayver et al., 2013), where $\sigma_{h,v}$ represents horizontal and vertical conductivity. For the logarithmic transform, upper and lower conductivity bounds of 10^{-4} S/m (10000 Ωm) and 1.5 S/m (2/3 Ωm) were used. $\mathbf{W_m}$ is a diagonal weighting matrix that weighs the model variations and can consist of different measures of the model norm (Farquharson and Oldenburg, 1998); μ is a regularization parameter that weighs the data- and model-dependent

terms of the objective function and contains a reduction exponent that gradually decreases the regularization ("cooling") at each iteration (Haber et al., 2000). The regularization parameter at iteration n is computed as $\mu = \frac{\mu_i}{(n+1)^p}$ where the regularization parameter μ_i weighs the data- and model-dependent terms and p is a parameter that defines by how much the influence of regularization is reduced at each iteration. For the modeling study, a simple least-squares weighting of the model variations, $\mu_i = 0.05$ and $p = 1.67$ were used. By minimizing the first order derivative of the conductivity depth profile in addition to minimizing the data misfit, the regularization seeks to generate a smooth model. Although there is no physical argument in using a smoothing constraint, smooth models are less likely to result in over-interpretation of the data since they will not contain small-scale features that are poorly constrained by the data. Our algorithm is similar to Occam inversion (Constable et al., 1987; deGroot Hedlin and Constable, 1990; Key, 2009), but does not include a search for the optimum regularization parameter. We found that in most cases field data cannot be fit to within a prescribed error level and searching for an adequate regularization parameter would return very small values of the objective function, leading to instable models. The algorithm is stable and rapidly convergent: a smoothed version of the true structure is typically recovered in 12-16 iterations.

The misfit x_{rms} is defined as the global root mean square error (rms):

$$x_{rms} = \frac{1}{n}\sqrt{\sum_{i=1}^{n} W_{d_i}[d_i - F_i(\mathbf{m})]^2} \tag{3.2}$$

where n is the number of data points. The inversion is terminated if the target rms is reached, or if either the objective function or the rms cannot be reduced during several subsequent iterations.

3.2.2. 3D INVERSION

The forward modeling algorithm used in the 3D inversion code consists of solving the second order partial differential equations (Mulder, 2006; Plessix et al., 2007):

$$i\omega\mu_0\bar{\sigma}\mathbf{E} - \nabla\times\nabla\times\mathbf{E} = -i\omega\mu_0\mathbf{J_s} \tag{3.3}$$

where $\mathbf{E}(\omega,\mathbf{x})$ represents the electric-field components as a function of angular frequency ω and position $\mathbf{x}$, the complex conductivity $\bar{\sigma} = \sigma + i\omega\epsilon$ includes conductivity $\sigma(\mathbf{x})$ and electric permittivity ϵ, and μ_0 is the magnetic permeability; μ and ϵ are assumed to be constant at their free-space values. We do not consider frequency-dependent conductivity variations; induced polarization effects are irrelevant for the fairly resistive geological settings studied here. The current source is $\mathbf{J_s}(\omega,\mathbf{x})$. Equation 3.3 is discretized using a finite volume-type discretization scheme resulting in a linear system of the form $\mathbf{AE} = \mathbf{F}$, where $\mathbf{A}$ is the discretized Maxwell operator, $\mathbf{E}$ represents the vector of the electric-field components on the discretized model, and $\mathbf{F}$ is the source vector. A conjugate-gradient iterative scheme, the BiCGStab2 scheme, preconditioned by a multigrid solver (Mulder, 2006) is employed to solve the large and sparse, but symmetric and non-Hermitian matrix $\mathbf{A}$. For multifrequency, multisource CSEM modeling, the code is parallelized over sources and frequencies. For further details about the forward modeling engine, the reader is referred to Plessix et al. (2007).

The inverse problem seeks to find a conductivity model that minimizes the weighted least-squares functional

$$f_{3D} = \frac{1}{2}\|\mathbf{W_d}(\mathbf{d} - F(\mathbf{m}))\|^2 + R. \tag{3.4}$$

$F(\mathbf{m})$ is obtained by solving Equation 3.3 and $\mathbf{d}$ contains the electric-field data. To balance the update of the shallow and deeper parts, a model weighting scheme that mainly depends on depth, is employed (Plessix and Mulder, 2008). We invert for the logarithm of the conductivity and impose upper and lower hard conductivity bounds. The data weights $\mathbf{W_d}$ are computed from the data amplitudes and noise. R is a regularization term given by $R = \sum \alpha_n(|\mathbf{m} - \mathbf{m}_0|^2)$, where n are the spatial directions and α_n are positive numbers that are calibrated such that the magnitude of the regularization term remains a small fraction of the total objective function value throughout the inversion. The objective function is then solved by employing a quasi-Newton method, the limited-memory BFGS method (Byrd et al., 1995) and a box average filter is applied to the gradient of the objective function in order to smoothen spatially rapid variations and geometry imprints arising from sparse source and receiver spacing or fine model discretization. For computational efficiency, we terminated all inversions after a maximum of 25 iterations, when in most cases convergence had slowed down and we were not expecting further significant model updates and misfit reductions.

In the following, vertical transverse isotropic (VTI) inversions were carried out for both 1D and 3D inversion using horizontal electric-field components E_x and E_y under the assumption that horizontal and vertical resistivities are different. If not mentioned explicitly, we focus on the vertical and do not show the horizontal resistivity, since the inversion is more sensitive to the vertical resistivity inside the resistive reservoirs of interest.

3.3. SYNTHETIC 3D RESOLUTION TESTS

3.3.1. RESOLUTION AND SENSITIVITY ANALYSIS

The Schoonebeek reservoir layer is located at about 700 - 800 m depth and its structure is well known from well logs, 3D seismic data and production data. We found from forward modeling tests that strongest reservoir responses should be obtained, while maintaining acceptable signal amplitudes, at source-receiver offsets between approximately 3 and 5 km.

Detailed numerical resolution and sensitivity analysis were carried out based on known properties of the Schoonebeek oil field in The Netherlands with the objective of obtaining high resolution towards a resistive reservoir target zone.

Resolution is the measure for the distance that two separated objects should have, to be identified as two objects and not as one single object. Thus, two objects can be resolved when their separation is larger than the minimum separation distance and their contrast to the background is higher than a predefined value. An object is detectable when amplitude differences of data with and without this object are sufficiently large and the phase differences are above the detection limit. An object can therefore be detectable but not resolvable.

We modeled a range of complex structures inside the Schoonebeek reservoir target zone to understand (i) the minimum size of a feature that is still detectable taking into

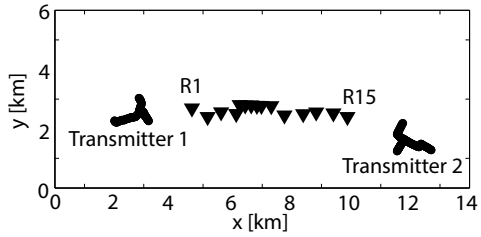

Figure 3.1: Source and receiver positions used for synthetic studies and field example.

account a specific acquisition geometry limited by various logistical constraints, and (ii) resolution limits and the capability to recover resistivity values.

To minimize impact and cost of the survey, we aim for a sparse field setup with few source locations and a small number of receivers. Synthetic sources and receivers were placed at positions where actual field deployment is possible such that the survey covers one of the locations where steam is being injected into the reservoir (Figure 3.1). The source available for our survey was a transmitter that feeds currents with a fixed phase relationship into three grounded electrodes. The overall source polarization can be adjusted by simply applying a constant phase shift to the three source currents (see Appendix A). We refer to this phase shift as the source polarization angle. Notice that the actual spatial orientation of the source polarization is determined by the combination of source geometry and the polarization angle applied. For the following synthetic calculations, if not mentioned otherwise, we modeled data for two transmitter positions and 15 receivers using source polarization angles of –30°, 30° and 270°. For forward modeling tests and as a background model for our 3D studies, we use a 1D background resistivity model that was obtained by taking the shallow subsurface resistivity information for the top 150 m from regional well-log data and resistivity at greater depths from 1D real-data CSEM inversion results of the Schoonebeek region (Figure 3.2). We tried a range of other starting models, but they gave poor convergence of the 3D inversion for field data and thus we limit our study to the mentioned background model. In Figure 3.3, we display examples of data d_1 calculated for the model shown in Figure 3.2, and data d_2 for a model containing a resistive block, consistent with well-log resistivities of oil-saturated parts of the reservoir, at depths of 785 - 800 m. The obtained electric-field amplitudes and phases for both models are shown in Figures 3.3a-3.3d for 12 frequency values per receiver. The normalized amplitudes of the differences calculated as $|\frac{d_2-d_1}{d_1}\times 100|$ are plotted in Figures 3.3e and 3.3f and their phase differences in degrees calculated as $|arg(d_2)|-|arg(d_1)|$ are plotted in Figure 3.3g and 3.3h. For increasing offsets the sensitivity towards the resistive body inside the reservoir increases, whereas overall amplitudes decrease by about two orders of magnitude. Further, the largest differences occur at frequencies of about 1 Hz for the electric-field component E_y. Even though the largest differences occur near the minima of the electric field, the signal-to-noise ratio for a typical noise-floor estimate of 10^{-10} V/m (Tietze et al., 2015), is still well above 1. Assuming a threshold of ~2° for a detectable phase difference and a threshold of ~5% for a detectable amplitude difference then the modeled differences in the N-S component

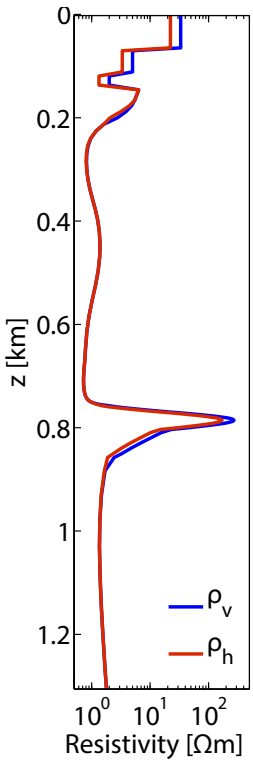

Figure 3.2: The 1D horizontal and vertical resistivity profile obtained from 1D CSEM inversion results of the Schoonebeek region and well log data, and used as background model for 3D synthetic inversions.

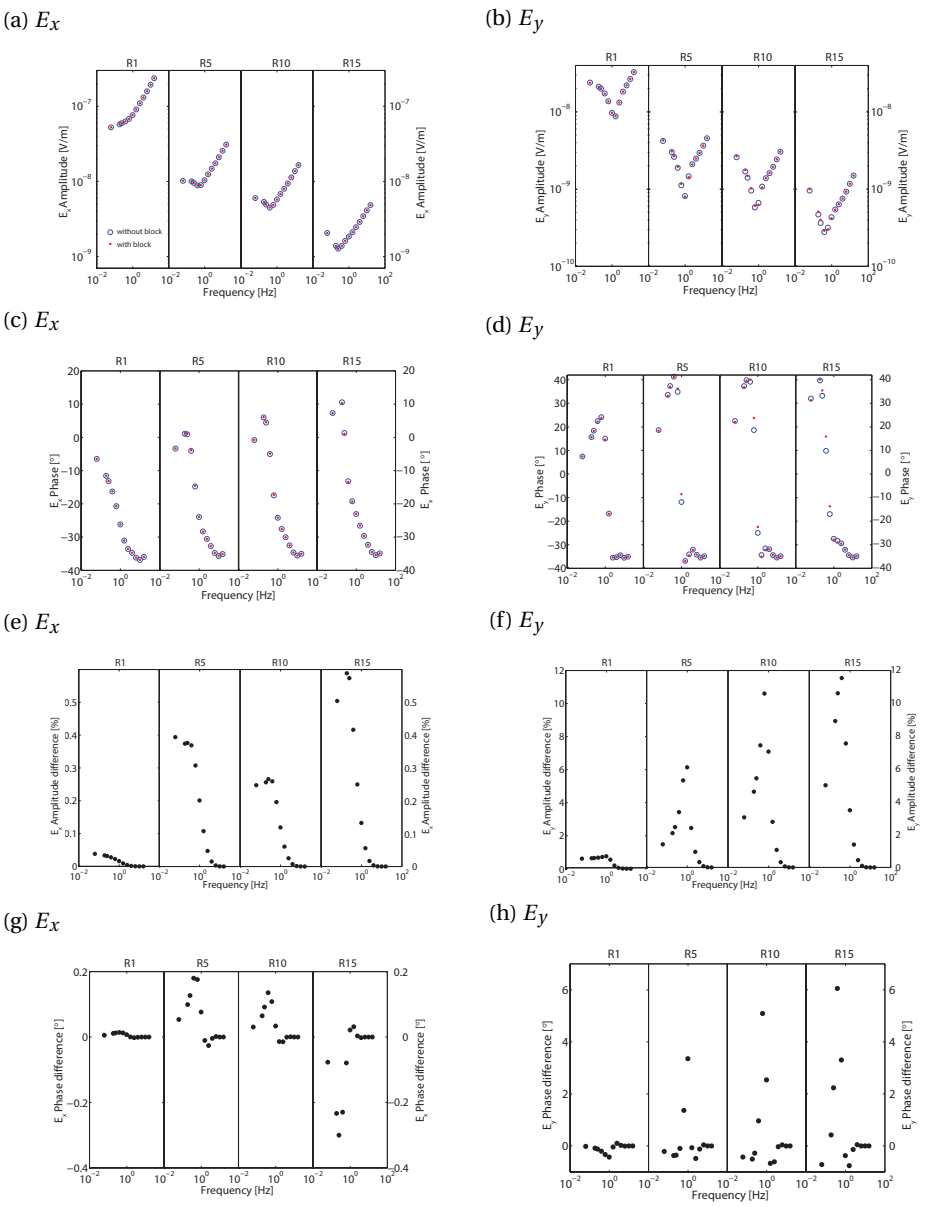

Figure 3.3: Electric-field data for transmitter 1 and for receiver position R1, R5, R10 and R15 with a source polarization angle of 30°. Electric-field amplitudes for (a) the N-S component E_x and (b) the E-W component E_y for the model shown in Figure 3.2 in blue and for the same Schoonebeek model with a block of dimensions 5000 m × 2000 m × 18 m and a horizontal and vertical resistivity of 200 and 333 Ωm, respectively, added inside the reservoir in red; (c) and (d) show the phase behavior; (e) and (f) show the amplitude of the difference between the model with and without resistive body in %; (g) and (h) show the difference in phase.

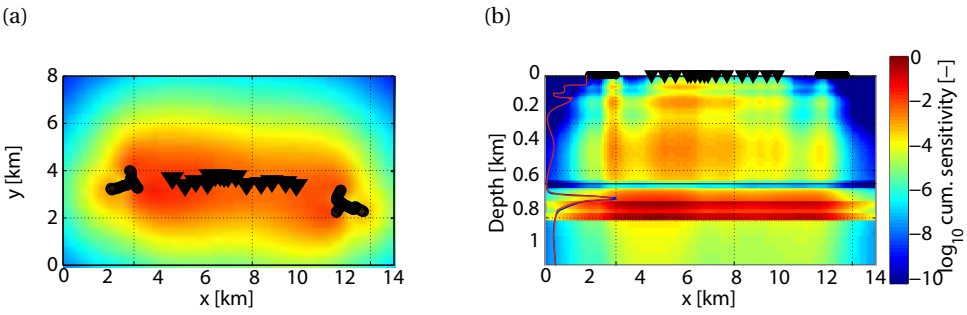

Figure 3.4: (a) Depth slice at reservoir level (785 m) of the normalized cumulative sensitivity to vertical resistivity. (b) Depth section of normalized cumulative sensitivity at y = 4 km. Black lines indicate the positions of the sources and black triangles indicate positions of the receivers. As reference, the 1D horizontal and vertical resistivity profile of Figure 3.2 is plotted on the left.

E_x are too small to be detectable. Differences in the E-W component E_y are sufficient for frequencies between 0.1 and 1 Hz and for source-receiver offsets larger than about 3.5 km. These results are important when considering appropriate survey geometry and frequency layout for real data collection.

To be able to resolve resistive or conductive structures at reservoir depth, the survey geometry has to be chosen such that the sensitivity to this depth range is sufficiently high. We first calculated the cumulative sensitivity as a weighted ℓ^2-norm resulting in a single sensitivity value for each model parameter that includes sensitivities with respect to all data values:

$$C(m_i) = \Big(\sum_{j=1}^{n} |W_{d_j} \frac{\partial F_j(m)}{\partial m_i}|^2 \Big)^{\frac{1}{2}} \tag{3.5}$$

where n is the number of data points counted over sources, source polarizations, receivers, and frequencies, $F_j(m)$ is the electromagnetic field at data point j, $\frac{\partial F_j(m)}{\partial m_i}$ is the Fréchet derivative of the data with respect to the model parameter m_i and $W_{d_j} = \frac{1}{F_j(m)+\epsilon}$ are data weights with $j = 1, ..., n$ and the absolute error floor is $\epsilon = 10^{-10}$ V/m. The cumulative sensitivities are normalized by their maximum value.

Horizontal and vertical sensitivity sections for the 1D resistivity profile from Figure 3.2 and the survey geometry from Figure 3.1 are depicted in Figure 3.4. In Figure 3.4a the logarithm of the normalized cumulative sensitivity to vertical resistivity at a depth level of 785 m is plotted, showing a high-sensitivity region between both transmitters and within an approximately 2-km wide corridor around the receiver locations, indicating that structures close to the receiver line should be detectable. Figure 3.4b shows the logarithm of normalized cumulative sensitivity in a vertical plane along the receiver line computed for the same conductivity model and survey geometry. Sensitivity is highest around the target depth of about 750 m. The sensitivity to the reservoir is high because of its high overall resistivity.

3D inversion solutions, especially for surveys with limited amounts of data and a sparse source receiver configuration, are highly non-unique. Every solution depends

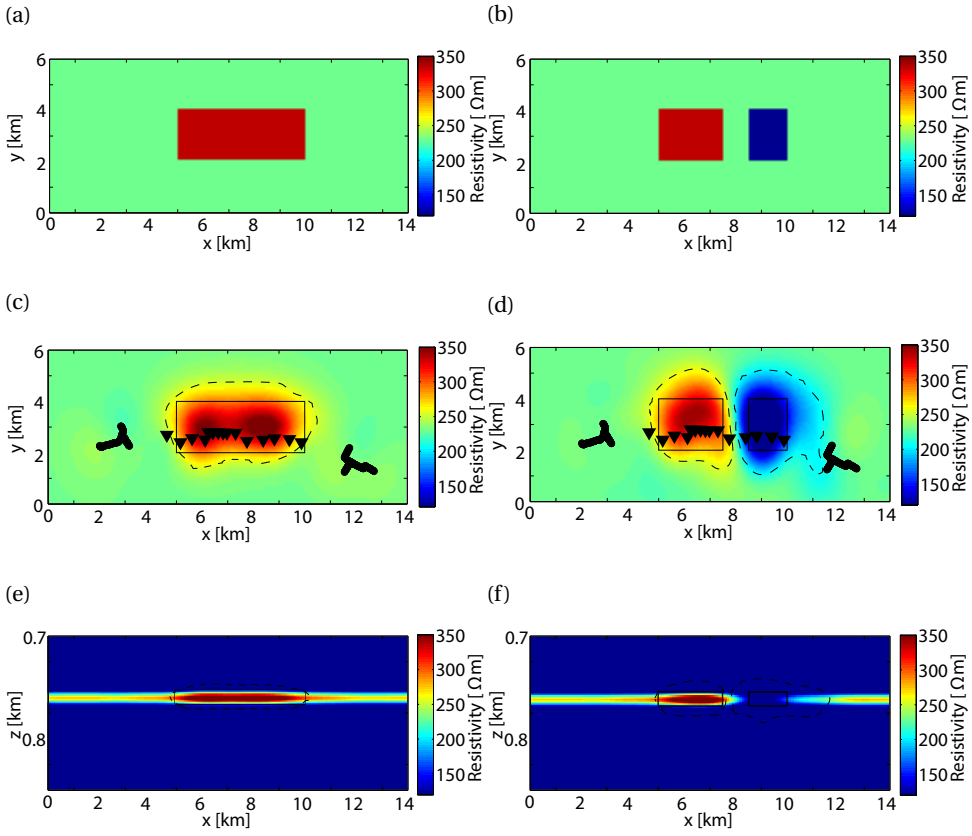

Figure 3.5: Inversion results after 25 iterations using the starting model shown in Figure 3.2 as the background model. (a) One-block scenario, (b) two-block scenario and (c),(d) corresponding inversion results. Depth slices at reservoir depth of 785 m are shown in (a)-(d) whereas (e) and (f) show the depth section around the reservoir. The black triangles are the receiver positions and the black circles highlight the transmitter locations projected onto the depth slice. The black rectangles indicate the borders of the inserted bodies and the black dashed lines indicate the borders of the inserted bodies after inversion. Note that a linear scale for resistivity was applied.

on the regularization and inversion parameters chosen. In order to test data distribution and the inversion algorithm for the ability to recover a known structure by using a limited survey geometry, we inverted two synthetic data sets created from two different model scenarios. Resistive and conductive bodies with certain dimensions were inserted into the reservoir layer to simulate a possible scenario of local resistivity variation due to steam injection. Again the 1D resistivity profile shown in Figure 3.2 was used as a background model. In the first scenario, one large block with dimensions of 5000 m × 2000 m × 18 m and horizontal and vertical resistivities ρ_h = 200 and ρ_v = 333 Ωm, respectively, was inserted into the reservoir (Figure 3.5a). In the second scenario, we inserted two somewhat smaller blocks, horizontally separated by 1 km. The block dimensions and resistivities were 2500 m × 2000 m × 18 m; ρ_h = 200 Ωm, ρ_v = 333 Ωm and 1500 m × 2000 m × 18 m; ρ_h = 20 Ωm, ρ_v = 33 Ωm (Figure 3.5b). We computed data for these two models with the source and receiver geometry shown in Figure 3.1. The inversion domain contains 201×208×142 cells with lateral dimensions of 100 × 100 m and variable thicknesses, while automatic frequency-dependent regridding (Plessix et al., 2007) is used to reduce the computational cost for forward modeling and gradient calculations. One inversion run requires approximately 40 GB of memory and takes about 24 h to complete the 25 iterations on an Intel Xeon 12-core 2.6 GHz cpu. Assuming that we have good knowledge about the background resistivity, we start the 3D inversion from the 1D model result of Figure 3.2. Figure 3.5c and 3.5d show depth slices inside the reservoir at 785 m depth for an inversion result after 25 iterations for the single-block and double-block model scenarios. The boundaries of the objects after inversion, indicated by black dashed lines, were in the following defined such that they coincide with a resistivity change of 10% from the background resistivity. Both inversions (Figures 3.5c-3.5f) detect the bodies and can resolve the bodies in resistivity and location although the vertical and lateral extent of the bodies are slightly larger than their true extent. The vertical resolution for both modeled scenarios is high (Figure 3.5e and 3.5f). Most likely, the high resistivity of the background model and associated high sensitivity at the reservoir depth has helped focusing the images. The acquisition design is thus capable of resolving large conductive and resistive structures at the reservoir depth.

To further evaluate the 3D inversion performance of the acquisition design, we tested the ability to resolve small and complex structures (Figure 3.6). Two scenarios are discussed: two highly resistive bodies of 1 km × 1 km separated by 500 m with ρ_v = 1000 Ωm; $\rho_h = \rho_v/2$ (Figure 3.6a) and a complex model with two highly resistive blocks and two blocks more conductive than the background reservoir and of different shapes with $\rho_{v,1}$ = 1000 Ωm, $\rho_{v,2}$ = 100 Ωm and $\rho_h = \rho_v/2$ (Figure 3.6b). Figures 3.6c and 3.6d show the inversion results at a depth of 785 m and Figures 3.6e and 3.6f show the inversion results for a vertical section in the depth range of the reservoir layer. Whereas Figure 3.5 shows absolute resistivities, Figure 3.6 focuses on model updates. The anomalies with small separation are difficult to resolve. This is illustrated by the resistivity profile along the black line in Figure 3.6c and by the dashed black line indicating the border of the resolved body with a resistivity increase of at least 10%. The two blocks are too close to each other to obtain two separate resistivity maxima. The complex scenario with four bodies can hardly be resolved horizontally and vertically assuming that amplitude differences lower than 10% are considered not to be detectable. Both inversions terminate before

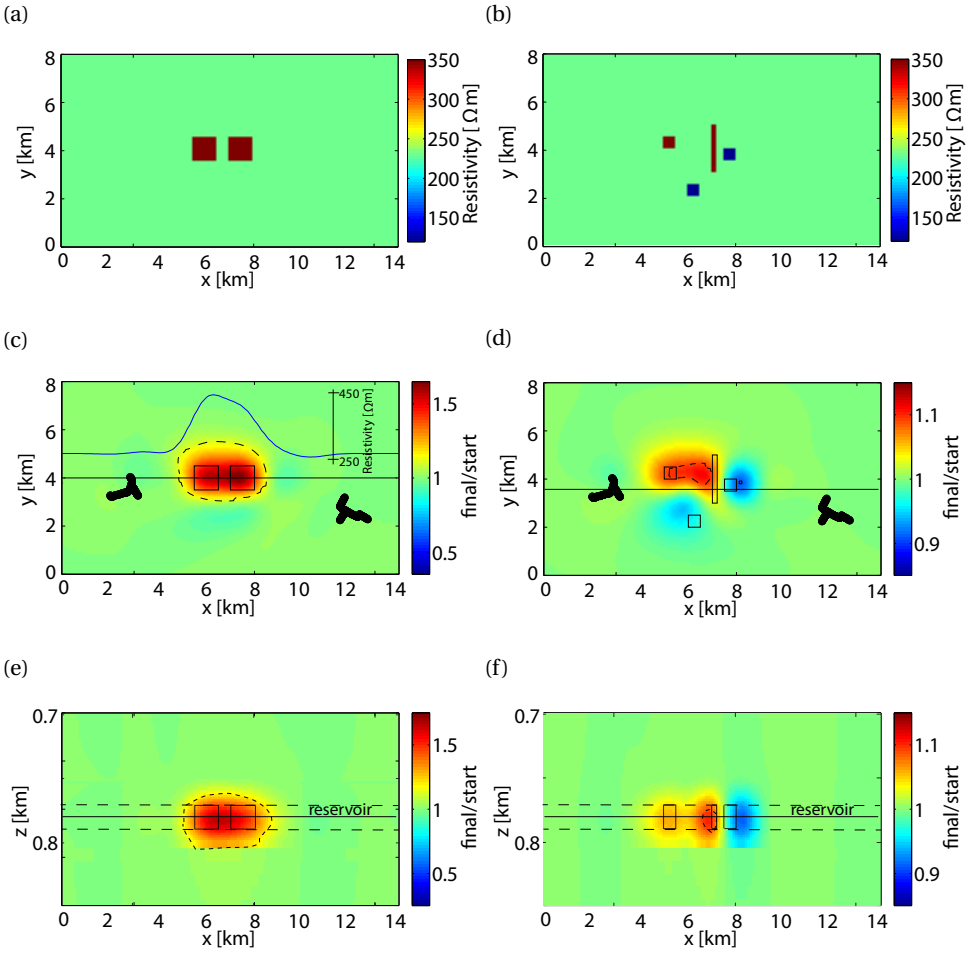

Figure 3.6: 3D inversion results of the models shown in (a) and (b). (c) and (d) show depth slices at reservoir depth of 785 m and (e) and (f) show the depth section around the reservoir. The solid black lines in (c) and (d) show the vertical cross-section plotted in (e) and (f) and the solid black lines in (e) and (f) show the depth level of the depth slices plotted in (c) and (d). The black rectangles indicate the borders of the inserted bodies and the black dashed lines indicate the borders of the inserted bodies after inversion.

reaching the true resistivity values. Additional receivers perpendicular to the receiver line and two additional sources north and south of the receiver line were tested, but adding receivers hardly improved resolution. Two additional sources, however, resulted in improved resolution for those bodies placed outside the receiver plane. Unfortunately, it is logistically impossible to add such sources in the field survey area. But since our primary interest is to resolve structures close to and underneath the receiver line, where we have resolution, the lack of resolution further away from the receiver plane is not of big concern.

3.3.2. CHOICE OF SOURCE POLARIZATION

To study the influence of source polarization on the quality of the inversion result, we analyzed synthetic data for single polarizations. Figure 3.7 displays 3D inversion results of three different polarizations of 30°, –30° and 270° using data for transmitter 1, not considering transmitter 2. The dashed black lines indicate the borders of the resistive block after inversion. Only for a polarization of 270°, the resistivity and location of the resistive body are recovered accurately (the easternmost part cannot be recovered because of poor coverage), whereas its shape and amplitude are distorted when using source polarizations of 30° or –30°. To achieve better resolution, a range of several different source polarizations can be used and inverted together (Figure 3.7d) as dependent polarizations in the data may deteriorate inversion results (Grayver et al., 2014).

3.3.3. INFLUENCE OF NOISE ON 3D INVERSION

A major aspect that influences the resolution is man-made EM noise. To assess the impact of field noise on resolution, uncertainties estimated from real data were used on synthetic data by applying weights to the data during the 3D inversion based on uncertainty information. An example of synthetic data with assigned uncertainties is shown in Figure 3.8, and inversion results are displayed in Figure 3.9. During inversion, data points with low signal-to-noise ratios are down-weighted, whereas data points with high signal-to-noise ratio are up-weighted to avoid significant model updates in regions where data misfits are high due to poor data quality. Estimated signal-to-noise ratios of the real data were up to 65 dB. Data points for which the real data had estimated errors larger than 10% (i.e. a signal-to-noise ratio less than 20 dB) were neglected. These synthetic inversion results can be compared with the results obtained from noise-free synthetic data (Figures 3.6c and 3.6d), where the data weights were computed based on data amplitude only, not considering uncertainty information. The objective functions were reduced to ~3% (Figure 3.9a) and ~4% (Figure 3.9b) of their initial values for both the noise-free and the noisy scenarios. Using realistic data uncertainties results in similar misfits but the shapes of the resolved bodies differ slightly and the obtained resistivity updates for both scenarios are by ~3% less when compared to the noise-free scenarios. The rms values (Figure 3.9e) are low, since we have used error estimates from field data, whereas our synthetic observed data are noise-free and thus have lower error levels than the field data. Internal rescaling in our inversion makes absolute error levels practically insignificant. However, by using these error estimates we modify relative weights of the data (down-weight low-quality, up-weight high-quality data points). These tests demonstrate that this slightly reduces the detectability of target structures.

(a) Polarization 30°

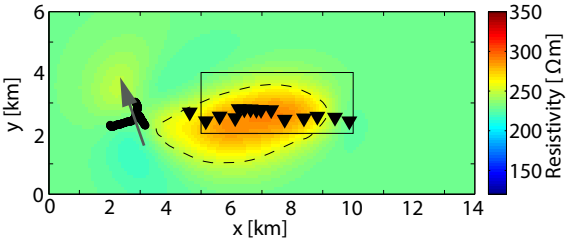

(b) Polarization –30°

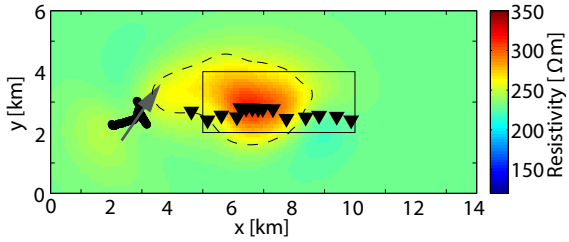

(c) Polarization 270°

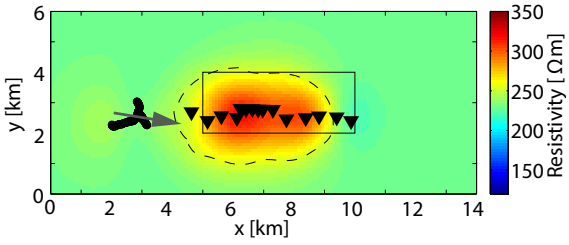

(d) All polarizations combined

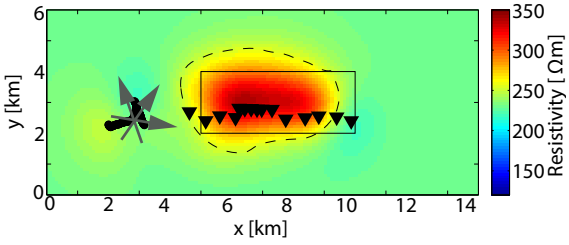

Figure 3.7: Dependence of the 3D inversion result on source polarization. Three different source polarizations are shown (see Appendix A): (a) 30°, (b) –30°, (c) 270° and (d) all source polarizations combined. The synthetic 1-block model from Fig 3.5a was used for this study. The gray arrows indicate the approximate dipole orientation of the source signal.

3.3.4. SUMMARY

We have shown that CSEM data from a survey consisting of a single receiver line of 15 receivers with a length of about 6 km and two transmitters approximately in-line with the receiver positions, is sensitive to and capable of resolving a resistivity distribution

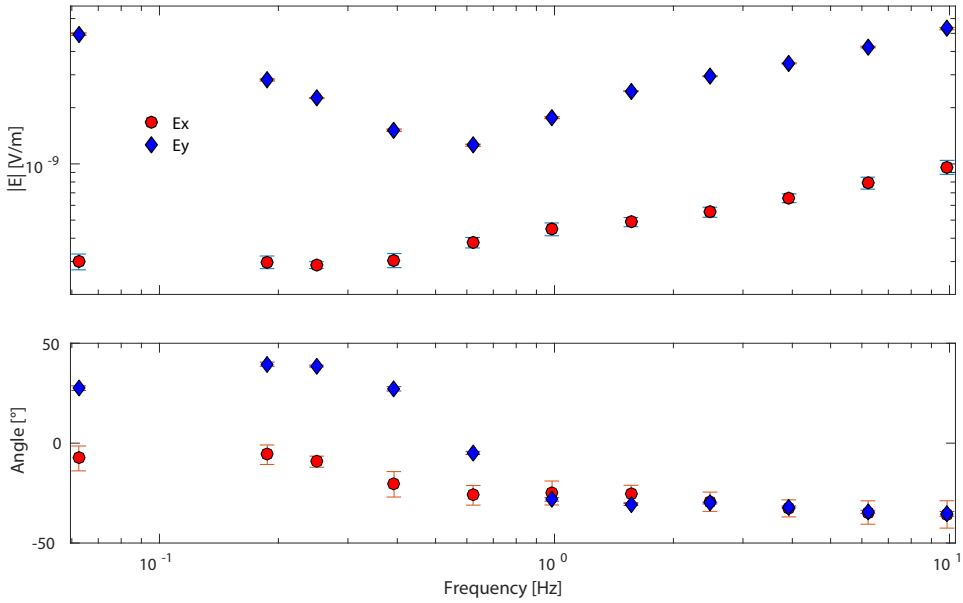

Figure 3.8: Example of synthetic data with error estimates from field data assigned. Data are for the two-block model from Figure 3.6a, transmitter 1 with polarization 270°, and receiver 11 (see Figure 3.1).

inside a reservoir within a roughly 2 km wide corridor around the receiver plane. This setup further allows resolving resistive and conductive features introduced by injected fluids. Whereas resistive bodies can be recognized and located if the background resistivity distribution is well known beforehand, their spatial dimensions and absolute resistivity cannot be resolved accurately, especially for small bodies inside the reservoir. The bodies are smeared out by the inversion and the obtained resistivities are lower than the true values. The survey geometry used caused some decrease in resolution away from the receiver line and stronger smoothing of complex structures. Additional sources at positions perpendicular to the receiver line would have resulted in improved resolution of the 3D bodies. For the 3D inversion, a 1D starting model resembling the true resistivtiy structure is advantageous. Such a background model can be derived from 1D inversion results, well-log and geologic information.

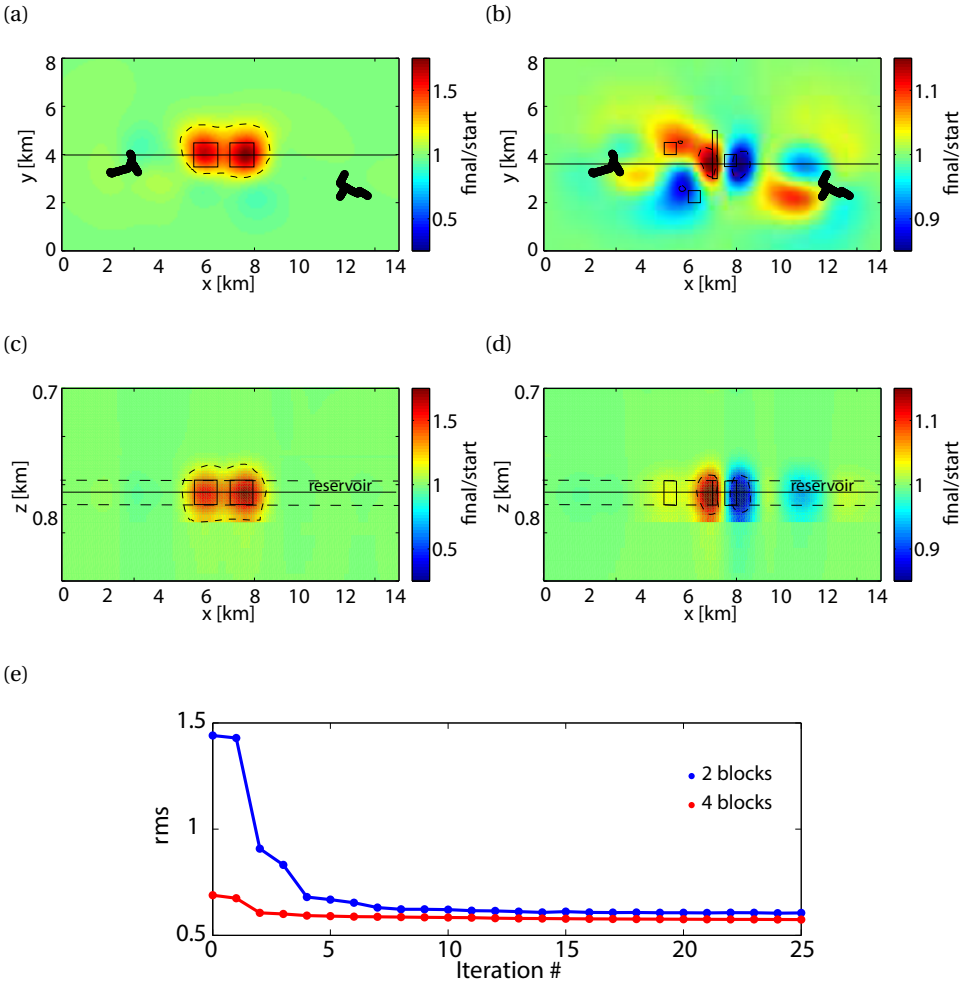

Figure 3.9: Influence of data uncertainties on inversion result. Data uncertainties obtained during processing are used as noise estimates. Inversion results for the model of Fig. 3.6a are shown in (a) and (c) and inversion results for the model of Fig. 3.6b are shown in (b) and (d). (a) and (b) show depth slices at reservoir depth of 785 m and (c) and (d) show the depth section around the reservoir. (e) shows the rms data misfits achieved. The noise-free scenarios are depicted in Figs. 3.6c-3.6f, respectively.

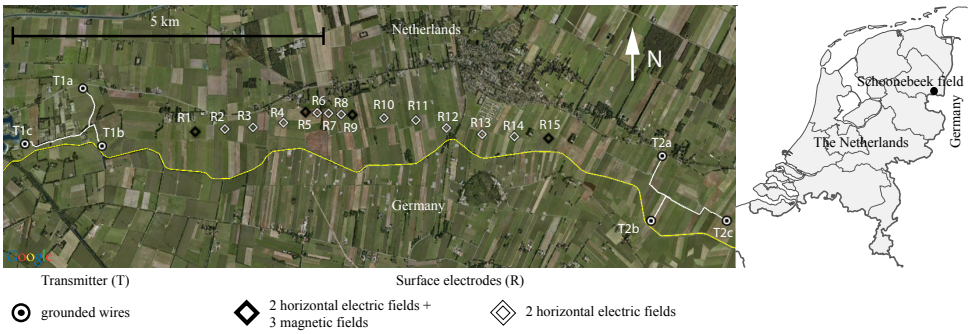

Figure 3.10: Location of field survey and detailed survey layout. Two transmitters are located west and east of the receiver line, respectively.

3.4. FIELD EXAMPLE AT SCHOONEBEEK

The actual CSEM field survey experiment was carried out at the Schoonebeek oil field in the Netherlands in 2014 with focus on an area where steam is injected into a reservoir for enhanced oil recovery (Michou et al., 2013). The reservoir, which underwent major changes due to 50 year production history (Rondeel et al., 1996), is located at a depth of about 700 m near the center of the receiver line and deepens to more than 800 m towards both transmitter locations. Source and receiver locations, as discussed in the modeling studies above, were used.

3.4.1. SURVEY DESIGN

Given the limited accessibility (i.e., border to Germany in the south and town of Schoonebeek in the north) and economic considerations, our acquisition setup was limited to two sources at each end of the receiver line. Our modeling study showed that by adding more receivers perpendicular to the receiver array did not improve the resolution. Figure 3.10 shows the geometry of the CSEM survey. There are 15 receivers at the surface spaced by roughly 0.5 km, with a denser spacing of 0.2 km towards the central part of the line. At 11 stations, only the horizontal electric-field components E_x (NS-oriented) and E_y (EW-oriented) were measured. At four stations, the three magnetic-field components were measured by deploying induction coils in all three spacial directions. The recording system used was the short-period automatic magnetotelluric (S.P.A.M. Mk. IV) data acquisition instrument developed by the German Research Centre for Geosciences (GFZ; Klose et al. (2011)). The CSEM source is a horizontal electric dipole source that generates horizontal and vertical current flow in the subsurface. It has the ability to generate multiple current polarizations without physically moving the source, as explained above and in Appendix A. Both transmitter locations east and west of the receivers were chosen such that the transmitter cables could be laid out along vehicle-accessible tracks in approximately T-shaped geometries resulting in approximately uniform azimuthal distribution of the CSEM source fields. To acquire useful CSEM data with sufficiently high signal-to-noise ratio, we transmitted square-wave signals at different base frequencies. We transmitted periods of 16, 8, 4, 2, 0.5 s to sample the entire

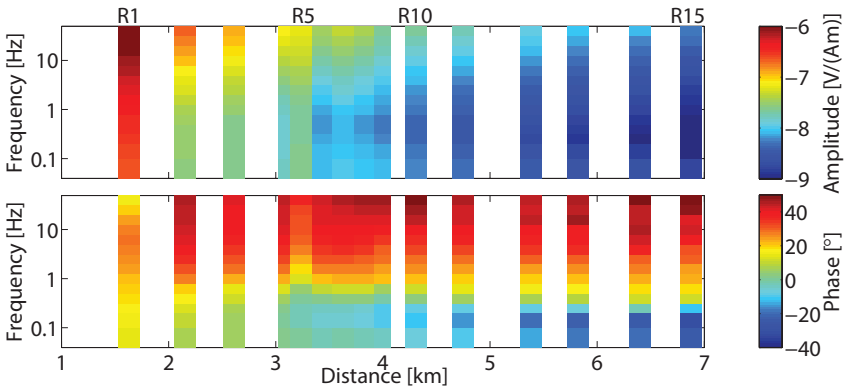

Figure 3.11: Response functions for component $T_{1,2}^{E_x}$ and for transmitter location 1 for all 15 receiver stations as a function of distance from source center and frequency.

frequency band that gives us information on the reservoir. At each position the source transmitted currents with amplitudes up to ~38 A at 560 V for 15-20 hours. We generated different source polarizations (–30°, 30°, 90°, and 270°) at Schoonebeek by adjusting the angle ϕ in equation 3.6. For more details about the source properties the reader is referred to Streich et al. (2013).

In the following, we only show electric-field data although we used magnetic-field data for quality control.

3.4.2. DATA PROCESSING

The data were processed in order to obtain response functions between the source and receivers. Some preprocessing was applied to improve signal-to-noise ratios. First, a notch filter was applied to remove the 50 Hz signal and associated harmonics, followed by a high-pass filter to remove signals at frequencies lower than the primary source frequency. All time-domain receiver and transmitter data are processed using identical filter parameters. Subsequently, the data were split into short time windows, and transformed to and stacked in the frequency domain to effectively remove time-variable noise. In calculating response functions, data from different source periods and polarizations were combined. The calculation effectively deconvolved the source currents, while not accounting for the source geometry or length of source wires. Bivariate response functions were obtained by choosing two of the three measured source currents fed into the three source electrodes (the third one is linearly dependent, yet the choice of currents may influence response function quality due to noise characteristics of the data) according to Equation 3.9. To reduce the influence of noise, we use a robust processing scheme, a technique routinely used for magnetotelluric (MT) processing (e.g., Egbert and Booker, 1986; Chave and Thomson, 1989; Ritter et al., 1998; Streich et al., 2013). Obtained uncertainty estimates are used for automated data preselection and weighting during inversion. In addition, data with errors higher than 10% of the amplitudes were neglected. A more detailed description can be found in Appendix B.

Response functions for transmitter location 1 and for E_x and E_y are plotted in Fig-

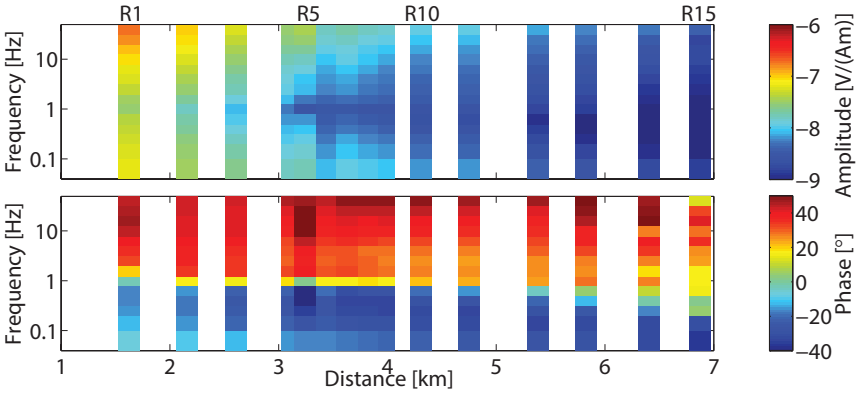

Figure 3.12: Response functions for component $T_{2,3}^{E_y}$ and for transmitter location 1 for all 15 receiver stations as a function of distance from source center and frequency.

ures 3.11 and 3.12. Figure 3.11 shows the response functions $T_{1,2}^{E_x}$, which is the horizontal electric-field component E_x, deconvolved from the source waveform, for the source polarized such that currents only flow through source electrodes 1 and 2 while the current on electrode 3 is zero. Figure 3.12 shows the response functions $T_{2,3}^{E_y}$ for E_y and the source polarized such that only currents I_2 and I_3 flow through source electrodes 2 and 3 while the current I_1 on electrode 1 is zero.

The amplitude and phase changes of the response functions $T_{1,2}^{E_x}$ (Figure 3.11) and $T_{2,3}^{E_y}$ (Figure 3.12) are smooth over the frequency spectrum of 1/16 to 100 Hz as well as between neighboring stations; this is to be expected from the diffusive nature of EM fields. Further, amplitudes decay with distance from the source. The closest receiver, station R1 in Figure 3.11, however, shows much higher amplitudes and different phase characteristics on the E_x component. These data, strongly influenced by near-source effects, could not be fitted by the inversion.

Low signal-to-noise ratios are a strong limitation to the measurements at Schoonebeek due to abundant EM noise sources. Attempts at quantifying ambient noise levels were made prior to the first CSEM survey. Noise levels were found to be strongly time-variant (e.g., related to activities on nearby drill pads). Specific noise sources were identified as being nearby production sites, a pipeline running approximately N-S between receivers R6 and R7 and common urban infrastructure. Station R5 suffered from anomalous responses, strongly different from those recorded at the neighboring stations, possibly related to a nearby dairy factory or a well casing located less than 100 m from the receiver. Station R15 suffered from strong noise, likely related to very nearby production facilities. As we did not succeed in removing this noise, stations R1, R5 and R15 would prevent the inversions of the entire data set from progressing and thus could not be considered. Numerous well steel-casings present in the survey area are very likely to influence the measurements but are difficult to quantify numerically and are therefore not considered at this time.

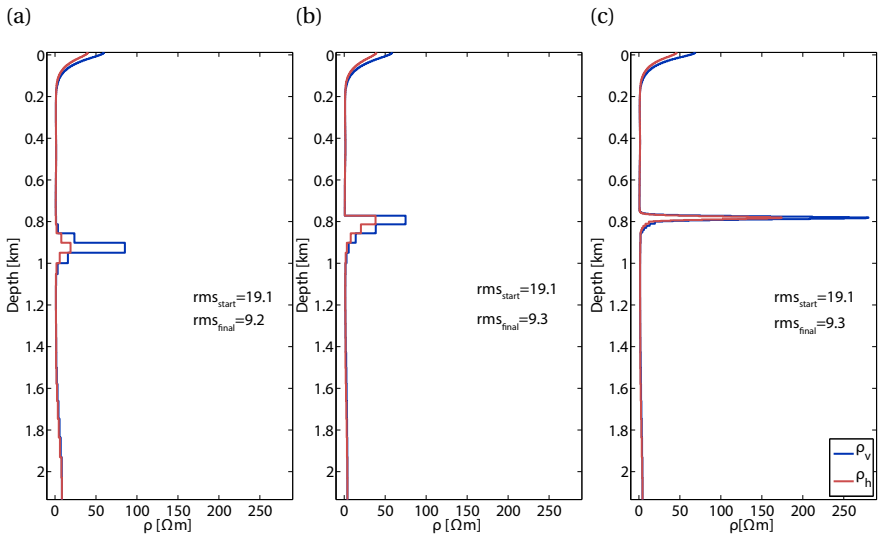

Figure 3.13: 1D inversion results using (a) a coarse depth spacing with 83 layers of increasing thickness with depth, (b) the same depth intervals but freeing the regularization constraint at expected reservoir depth of 780 m and (c) fine layering of 2 m around reservoir depth.

3.4.3. 1D INVERSION

We first invert our data (see Figure 3.11 and 3.12) for the resistivity distribution assuming a horizontally layered earth. The aim of the 1D inversion is to obtain a plausible starting model for a 3D inversion. Both single-receiver and multi-receiver inversions with joint sources were carried out for our two-component receivers. For a single-receiver inversion, the inversion was carried out separately for every source-receiver pair. Transmitted signals with different polarizations but the same source location are inverted together. For multi-receiver inversions the entire data set is inverted jointly resulting in one average resistivity model of the subsurface. The number of layers was set to 83 where layer thicknesses were allowed to vary with depth. To resolve the thin reservoir and its known high resistivity compared to its surroundings, layer thicknesses around reservoir level were set to 2 m. Resistivity anisotropy (ρ_v/ρ_h) was constrained towards a ratio of 1.2, based on geological information and inversion parameter testing. A regularization parameter $\mu_i = 1.2$ and $p_c = 1.67$ and resistivity bounds of 2/3 Ωm and 10000 Ωm were used, and frequencies above 10 Hz were neglected for the following 1D inversions (see theory section on 1D inversion). We use 12 iterations to obtain our final inversion result.

The horizontal electric-field data were inverted for the anisotropic resistivity distribution using either a homogeneous half-space starting model or a starting model with a more complex near-surface resistivity distribution derived from recent well-log data. Figure 3.13 shows three different inversion results obtained by changing the layer thicknesses in the starting model and by relaxing the regularization constraint at reservoir depth. Other inversion parameters were kept untouched. We obtain a smooth resistivity model with high vertical resistivity inside the reservoir (Figure 3.13a). Sensitivity to

the horizontal resisitivity in the reservoir is low and thus may explain why the inversion returns fairly low horizontal resisitivity values. The reservoir is smoothed out to a vertical extent of about 200 m, much thicker than the expected extent of ~20 m. Since we are interested in deriving a suitable and realistic 1D model as input for 3D inversion, we need to constrain our inversion to obtain a model closer to the real structure. One way of doing so is to use depth constraints imposed by seismic structure to regularize the CSEM inversion (Brown et al., 2012). This can be done by removing the regularization constraint (roughness penalty) at the expected depth of the reservoir (Myer et al., 2012). Figure 3.13b shows a resistivity model obtained after removing the smoothness constraint at the top of the reservoir at ~780 m. We obtain a reservoir with similar maximum vertical resistivity as before, but exhibiting a sharp boundary at the depth level where regularization was removed. At the bottom of the reservoir, a sharp contrast could be introduced in the same way. However, we prefer the inversion to be less constrained by a fixed depth level and sharp contrasts in the model may cause artifacts in subsequent 3D inversion. Therefore, we introduce a fine layering of 2 m around the expected reservoir level (700 - 900 m), while keeping increasing layer thickness with depth elsewhere. Figure 3.13c shows that the vertical extent of the reservoir is much smaller now than for the previous models. In addition, the vertical resistivity of about 280 Ωm is much closer to values suggested by resistivity logs. The final rms errors for all three models are given in the figures and are similar to each other.

Independent of the regularization and the chosen constraints, the transverse resistance, i.e. the integral of resistivity times layer thickness over the reservoir interval, should be better defined than resistivity and layer thickness individually, and should be similar for all inversion models (Constable and Weiss, 2006; Key, 2012). We obtain the following values for the vertical transverse resistance of the reservoir: 6200 Ωm^2 for the smooth model from Figure 3.13a, integrating over a depth range from 800 m to 1050 m, 5600 Ωm^2 for the model in Figure 3.13b (integration range 750 to 950 m), and 5400 Ωm^2 for the model in Figure 3.13c (integration range 750 to 900 m). The transverse resistance values are fairly similar but not identical. These results illustrate the ambiguity of the inversion together with the conclusions of Salako et al. (2015) that the best resolved parameter in CSEM is an estimate of bulk electrical resistivity for the reservoir.

Since we have near-surface resistivity values from a shallow well log acquired prior to the CSEM survey near receiver R7 (see Figure 3.1), we also tested fixing the near-surface and only allowing updates for the deeper layers. The resulting resistivity profile is depicted in Figure 3.14a. Comparing this model to a synthetic model obtained solely from well-log information (see Figure 3.14b) we find that the reservoir is located at similar depths, and the resistivity variations above the reservoir follow a similar trend. Layers below the reservoir are not resolvable by our inversion due to limited penetration depth and the resistive nature of the reservoir and thus are not interpreted.

To obtain the final model to be used for our 3D inversion, response functions from both sources and all receivers were inverted jointly.

Misfits between synthetic and real data, as defined in equation 3.2 but without summing over frequency and space, are shown in Figure 3.15. It can be seen that the misfits improve over the entire frequency spectrum for both horizontal electric-field components. Receiver R1, R5 and R15 are not plotted here, since they were not used in the

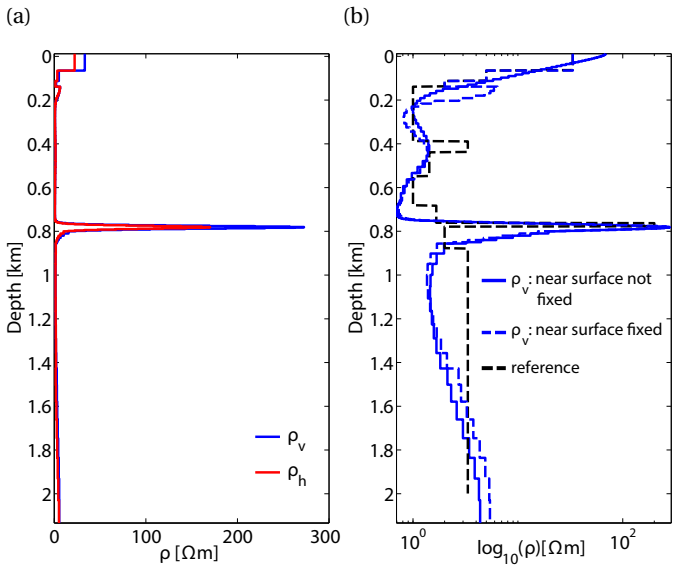

Figure 3.14: (a) 1D subsurface resistivity profile with fixed near-surface layers and (b) comparison of 1D subsurface resistivity profile with and without fixed near-surface layers to 1D subsurface resistivity profile obtained from well-log data. For better visibility the resistivity is plotted in logarithmic scale.

inversion (see discussion of these receivers above).

So far we have treated the geology of the Schoonebeek area as being horizontally layered. Figure 3.16 highlights the depth of the base of the Bentheim sandstone at Schoonebeek, in which the reservoir is located. The horizon was picked from seismic images and clearly indicates complex fault structures and a dipping reservoir. The reservoir depth is shallower than 700 m in the center of our profile and increases to more than 800 m at the sides. Therefore, inverting each receiver separately may reveal a higher resolution per receiver position. In Figure 3.17 each receiver was inverted separately for transmitter location 1. The inversion indicates slightly increasing reservoir depths away from the center of the profile, which is in agreement with the regional geology (see Figure 3.16). Because the resistive reservoir extends far beyond the acquisition layout and data from a source-receiver pair are mainly affected by the structures in between, anomalies from the reservoir get stronger with increasing source-receiver distance as more of the anomalously resistive body enters the volume being sampled (Myer et al., 2012). This may explain that the reservoir resistivities seen by receivers R2 and R4 closest to the source are lower than those of the other receivers (Figure 3.17).

As a final 1D inversion test, we investigate the dependency of inversion results on source polarization. Response functions computed directly by applying Eq. 3.9, assuming zero transmitter current on one source electrode, correspond to polarizations of 30, 90, 150, 210, 270 and 330°. Inversions shown in Figures 3.13, 3.14 and 3.17 used three of these polarizations simultaneously (30, 330(–30) and 270°, corresponding to $\mathbf{T}_{1,2}$, $\mathbf{T}_{1,3}$ and $\mathbf{T}_{2,3}$ according to Eq. 3.9). Data for other source polarizations can be generated by

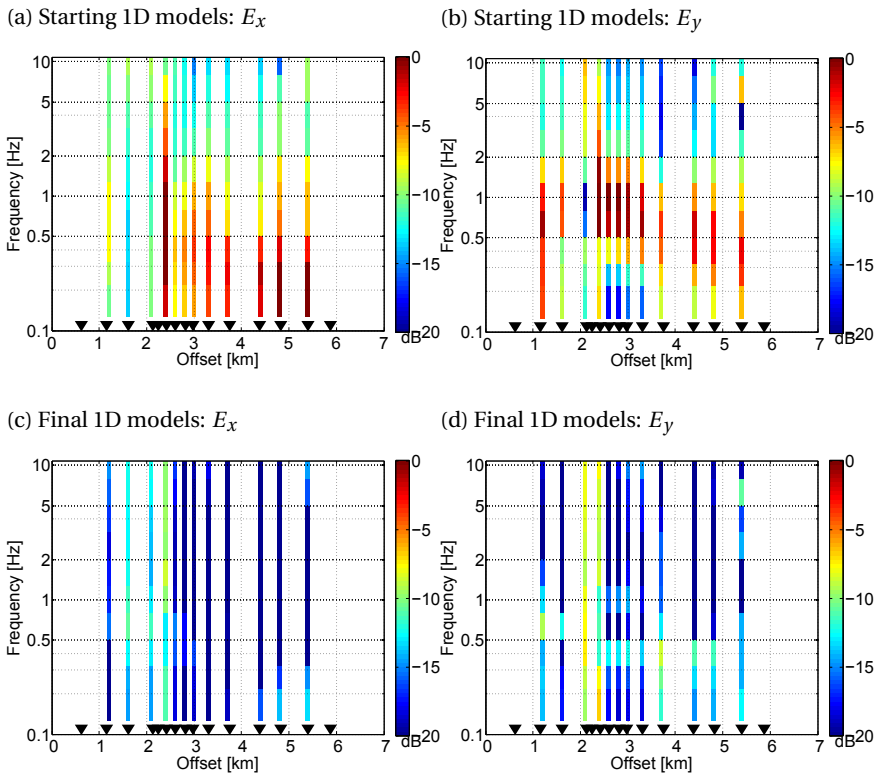

Figure 3.15: Data misfits for transmitter 1 before (a) and after (c) inversion for E_x for source polarization 30° and misfits before (b) and after (d) inversion for E_y for source polarization 270°.

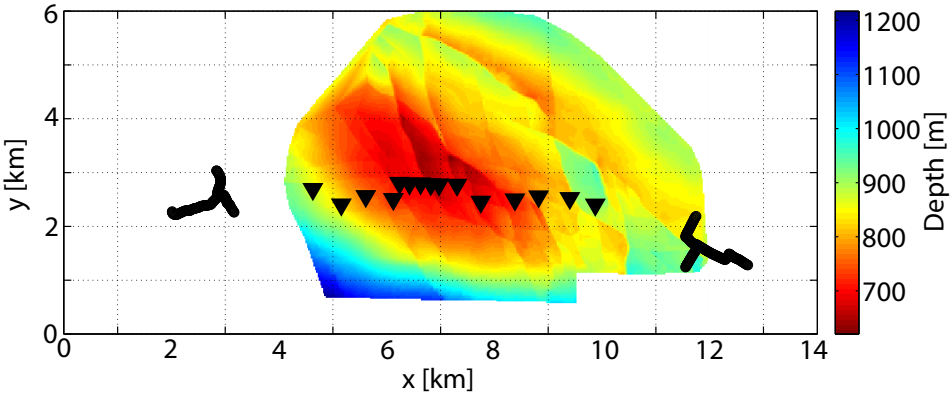

Figure 3.16: Depth of base of Bentheim sandstone. Black triangles and lines indicate the survey geometry.

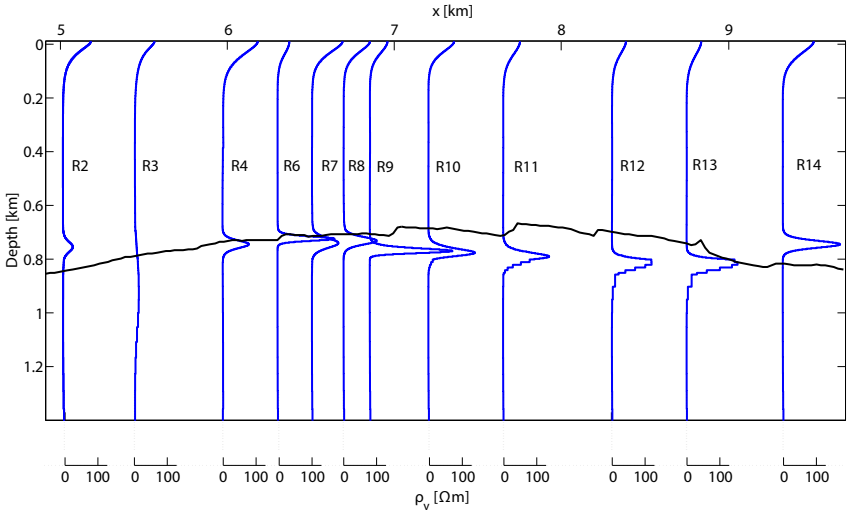

Figure 3.17: 1D inversion results for transmitter location 1, inverting each receiver separately. For reference, the black line indicates the depth of the base of Bentheim sandstone as shown in Figure 3.16.

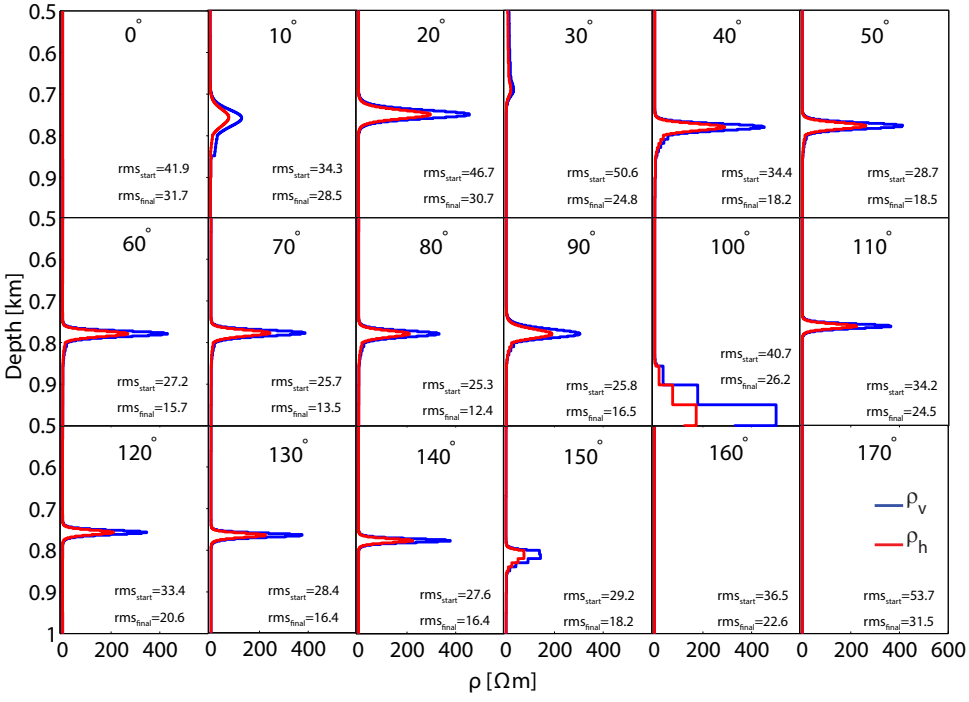

Figure 3.18: Dependence of the 1D inversion result on source polarization for the horizontal electric-field components E_x and E_y and for transmitter location 1 using all receiver stations. Start and final rms errors are given for each polarization.

numeric source rotation (Streich et al., 2013). Figure 3.18 shows inversion results for 18 different source polarizations, inverting for a single polarization at a time. This shows that the 'native' polarizations of 30, 90 and 150° provide poorer images of the reservoir than many of the other polarizations tested. The quality of inversion results may thus be enhanced by choosing a different set of polarizations. Start and final rms errors give a further indication about the quality of inversion results. For most of the 18 polarizations, lowest errors correspond with polarizations where reservoir is best resolved. For further inversions, we use polarizations of 30, -30 and 270°.

For the 1D inversion, we can conclude that the reservoir can be clearly resolved. Modifying the roughness constraint to allow for jumps in resistivity or introducing small layering around the reservoir location may add structure to the inversion model. Changes of the reservoir depth along the profile agree with known geology. However, as not every source-receiver pair images the reservoir clearly, 3D models obtained by interpolating individual-receiver inversion results tend to contain a more blurry image of the reservoir. This was found to be disadvantageous for subsequent 3D inversion. Therefore, we used the 1D subsurface resistivity profile with fixed near-surface layers obtained from multi-receiver inversion with joint sources (Figure 3.14) as input starting model for our 3D inversion.

3.4.4. 3D INVERSION

Resistivity heterogeneities inside the reservoir due to steam injection are expected to exhibit rather complex 3D patterns. Overall, steam injection is likely to reduce reservoir resistivity (Mansure et al., 1993; Butler and Knight, 1995). However, reservoir simulation data suggest (Streich, 2016) that areas of increasing as well as decreasing resistivity are expected at Schoonebeek due to simultaneously on-going processes of different magnitudes, length and timescales. Temperature increase, gradual condensation of steam, displacement of highly resistive oil as well as the reduction of salt concentration due to mixing of steam with saline water are some of the processes that may lead to compartmentalization of the reservoir with different zones showing increasing and decreasing resistivity, respectively (Tøndel et al., 2014). Thus, 3D inversion of the electromagnetic data is needed. Because 3D inversion of our sparse data set is strongly under-determined, and our 3D inversion uses a quasi-Newton algorithm (contrary to Gauss-Newton for the 1D inversion), choosing an appropriate starting model is important. We therefore study the influence of different starting models to the inversion result. At first, we use our best 1D inversion model from Figure 3.14a, ignoring the known dip of the reservoir (Fig. 3.19a). As a second attempt, we use a 2D model built by extracting the reservoir topography underneath the receiver line from the horizon shown in Figure 3.16. The top 580 m are left unchanged from the 1D model. At depths below 580 m, resistivities are defined by shifting the 1D resistivity column vertically such that the resistivity maximum coincides with the depth of the picked horizon (Fig. 3.20a). Third, we use a 3D model in which the 1D resistivity column is shifted vertically, as for the 2D model, but this time the depths of the entire Bentheim sandstone horizon were used, and the model was modified from the 1D column at depths below 400 m (Fig. 3.21a). The applied starting model is used as a reference model for the regularization, i.e. the difference of the model vector $\mathbf{m}$ from an a-priori model $\mathbf{m_0}$ is considered, resulting in a regularization based on the deviation

from the starting model. For our real data we applied the same parameters that were used for the synthetic inversion studies.

Figure 3.19 shows 3D inversion results using the 1D starting model. The starting and final resistivity model as well as the resistivity updates expressed as $\rho_{final}/\rho_{start}$ are plotted in logarithmic scale. Assuming an average or typical resistivity for the reservoir, the resistivity updates may give an indication about lateral variations within this reservoir. Trajectories of one steam injection (red) and two adjacent oil production (blue) wells are included for reference. Steam injection and production through these wells is expected to locally affect reservoir resistivities. There are many more wells in the field though, and the impact of the casings on our data certainly needs to be assessed further.

Due to the high resistivity of the reservoir, model updates are concentrated inside the reservoir where the sensitivity of the measurements is expected to be the highest (see Fig. 3.4). Fig. 3.19 indicates that reservoir resistivity is increased especially between x = 5~7 and 8~10 km. For the 2D starting model (Fig. 3.20), model updates focus on the reservoir and show a general increase in reservoir resistivity along the entire receiver array, but most strongly at the dipping flanks of the reservoir. For the 3D starting model (Fig. 3.21), the inversion result shows strong resistivity increase especially east of the production and injection wells. The inversion result from the 3D starting model (Fig. 3.21) is most consistent with our expectations. The model updates in Figure 3.21c suggest a gap in the resistor near the well where intermittent water injection during decades of production and recent steam injection took place. This has most likely created a more conductive region around the injection well. Surface measurements alone, though, are not capable of distinguishing between the type of the injected fluid. Thus, supplementary borehole-to-surface measurements (Wirianto et al., 2010), measurements of the vertical electric field and/or high-resolution seismics (Michou et al., 2013; Hornman and Forgues, 2013) are required to image the reservoir and its fluid content in more detail.

The misfit is measured by employing the least-square functional as described in Eq. 3.4. Figures 3.22 and 3.23 show the starting and final data misfits for the horizontal electric-field components E_y and for all three inversion scenarios. Although the starting data misfits between starting model and data are higher for the more complex 2D and 3D models (see Figure 3.22), the final misfit values for the 3D starting model are consistently lower indicating a better data fit for all receivers (see Figure 3.23). The development of rms values throughout the inversions for each starting model is depicted in Figure 3.24. Again, using a more complex starting model results in a higher starting misfit, but leads to better overall data fitting and lower final data misfits in the case of the 3D starting model. The rms values are significantly reduced compared to those obtained from 1D inversion, but we do not achieve ideal rms values of 1. This may indicate that we have somewhat overestimated signal-to-noise ratios in our data. Further iterations of these inversions (not shown) did not reduce the rms values significantly, while introducing structure we do not consider geologically meaningful.

Since we are interested in lateral resistivity variations inside the reservoir, we show in Figure 3.25 depth slices through the reservoir. The resistivity structure found within the resistive reservoir is similar for the more complex starting models (Figure 3.25b and 3.25c) and shows highly resistive zones between x = 4~6 km and 10~12 km close to transmitter 2. Using a simple 1D starting model instead, results in high-resistivity

(a) Starting resistivity model

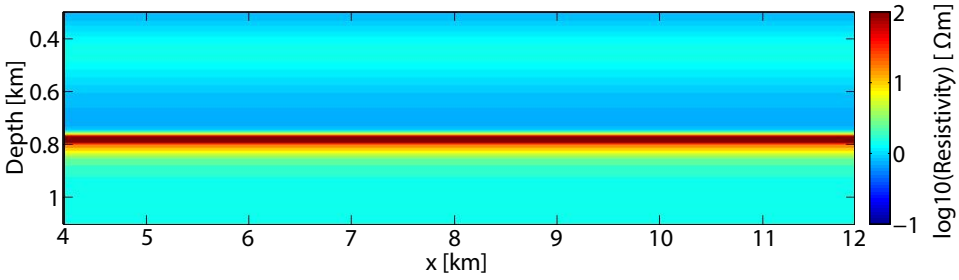

(b) Final resistivity model

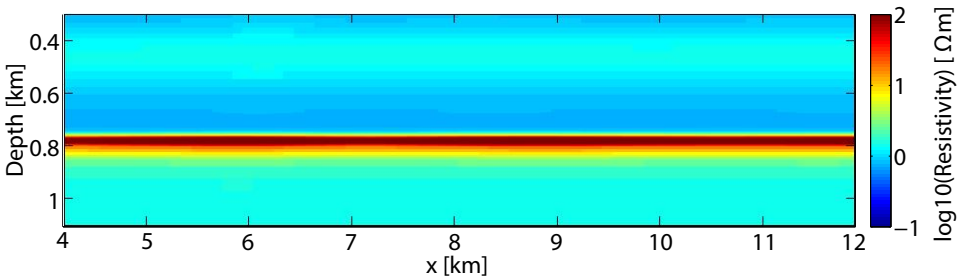

(c) Ratio between final and starting model

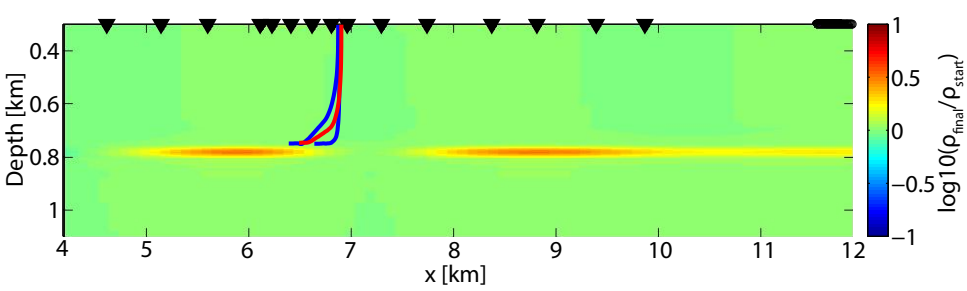

Figure 3.19: Depth sections at y = 3 km (see Fig. 3.1) through (a) 1D starting model derived from 1D inversion results, and (b) resistivity model after 3D inversion of E_x and E_y data. Resistivity updates are shown in (c). Red and blue lines are trajectories of steam injection and production wells projected into the section. Black dots and triangles indicate source and receiver locations, respectively.

(a) Starting resistivity model

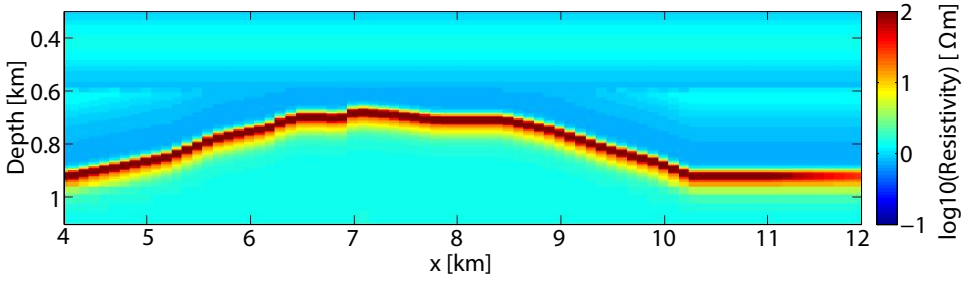

(b) Final resistivity model

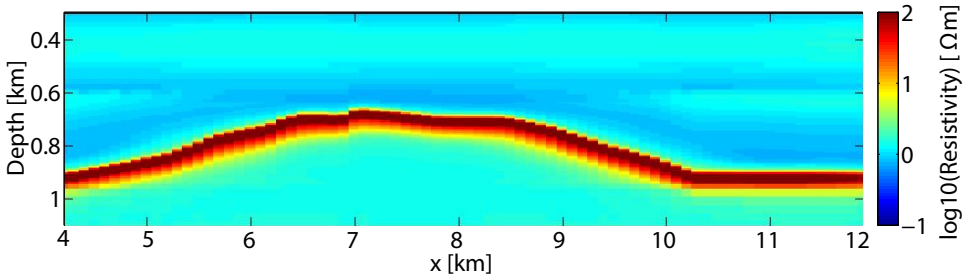

(c) Ratio between final and starting model

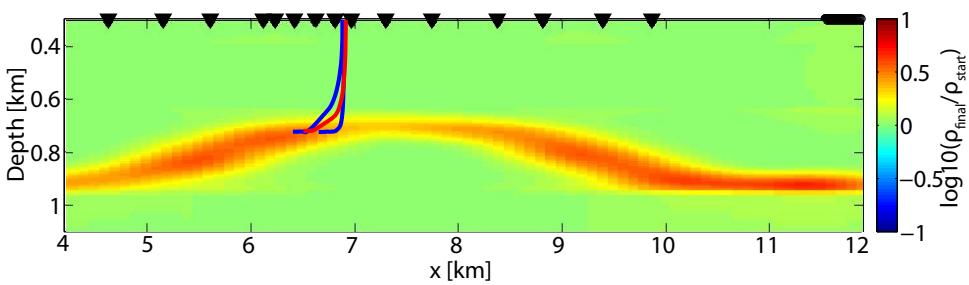

Figure 3.20: Depth sections at y = 3 km through (a) 2D starting model derived from 1D inversion results and the horizon shown in Fig. 3.16, and (b) resistivity model after 3D inversion of E_x and E_y data. Resistivity updates are shown in (c). The projected well trajectories are plotted in blue (production wells) and red (injection well).

(a) Starting resistivity model

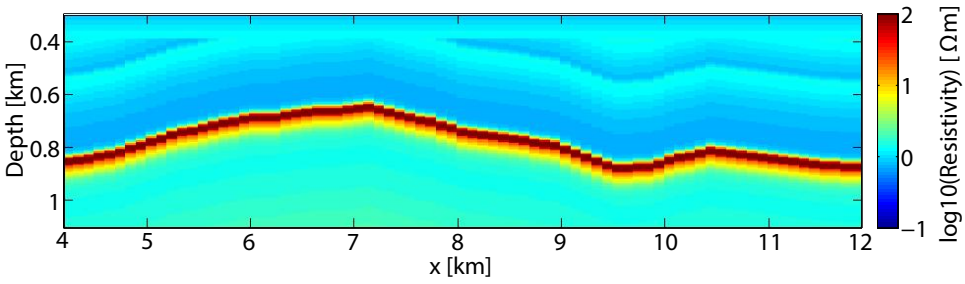

(b) Final resistivity model

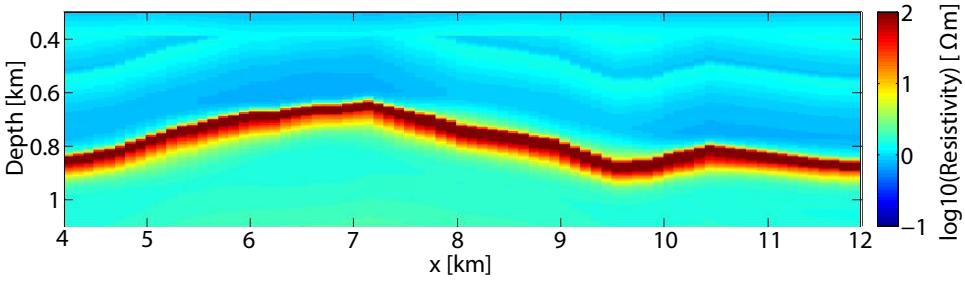

(c) Ratio between final and starting model

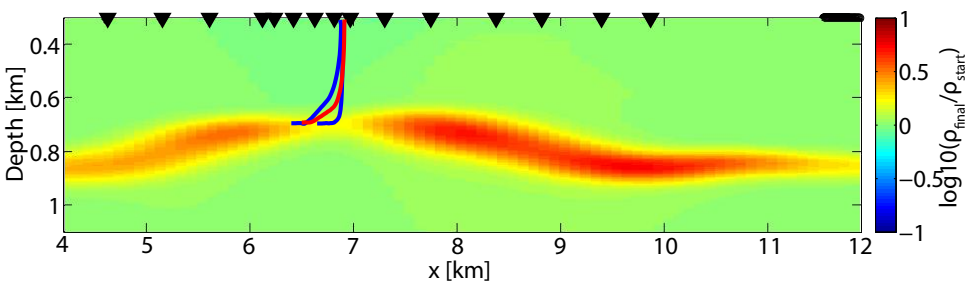

Figure 3.21: Depth sections at y = 3 km through (a) 3D starting model, and (b) resistivity model after 3D inversion of E_x and E_y data. Resistivity updates are shown in (c). The projected well trajectories are plotted in blue (production wells) and red (injection well).

(a) 1D starting model

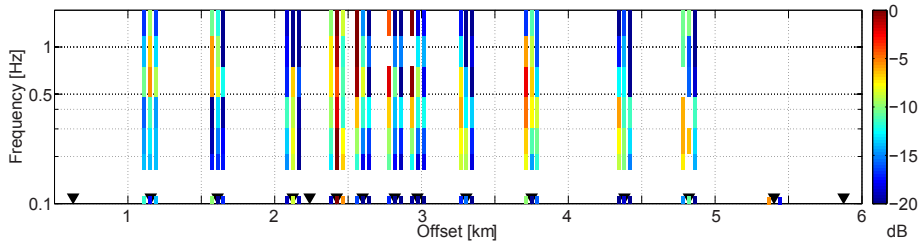

(b) 2D starting model

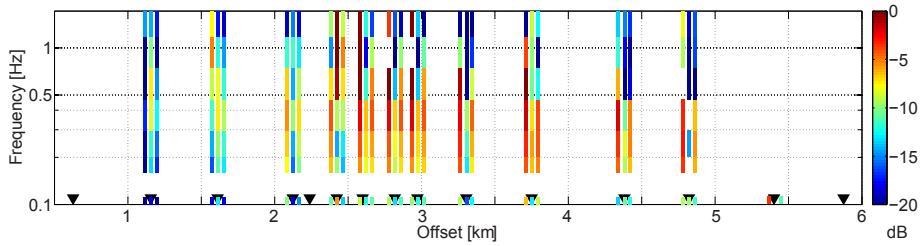

(c) 3D starting model

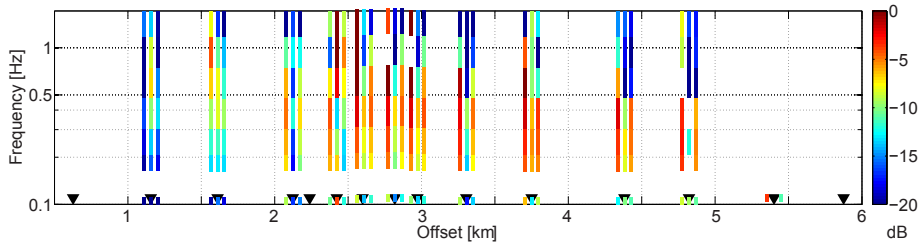

Figure 3.22: Data misfits for transmitter 1 before inversion for E_y and for all three source polarizations using a (a) 1D, (b) 2D and (c) 3D starting model.

(a) 1D starting model

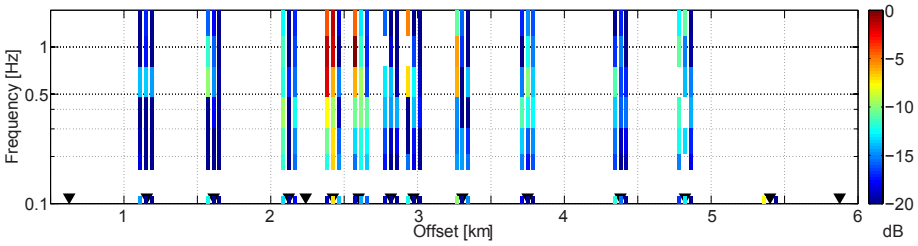

(b) 2D starting model

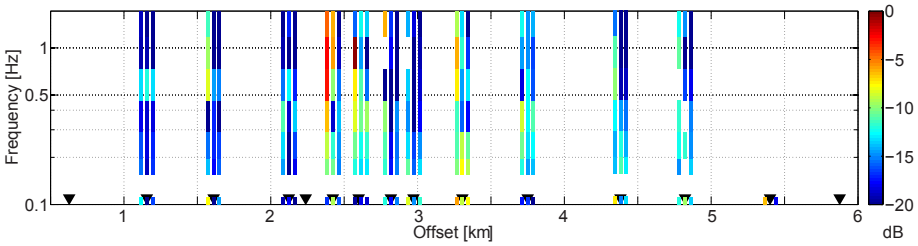

(c) 3D starting model

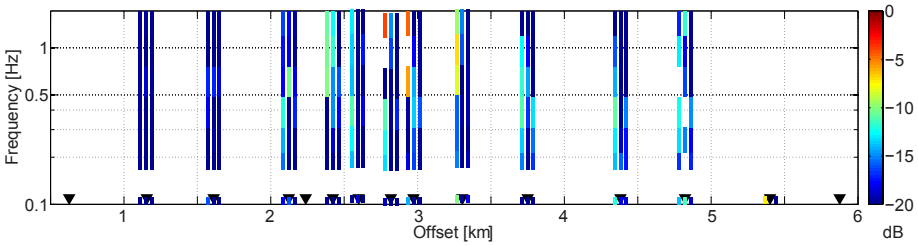

Figure 3.23: Data misfits for transmitter 1 after inversion for E_y and for all three source polarizations using a (a) 1D, (b) 2D and (c) 3D starting model.

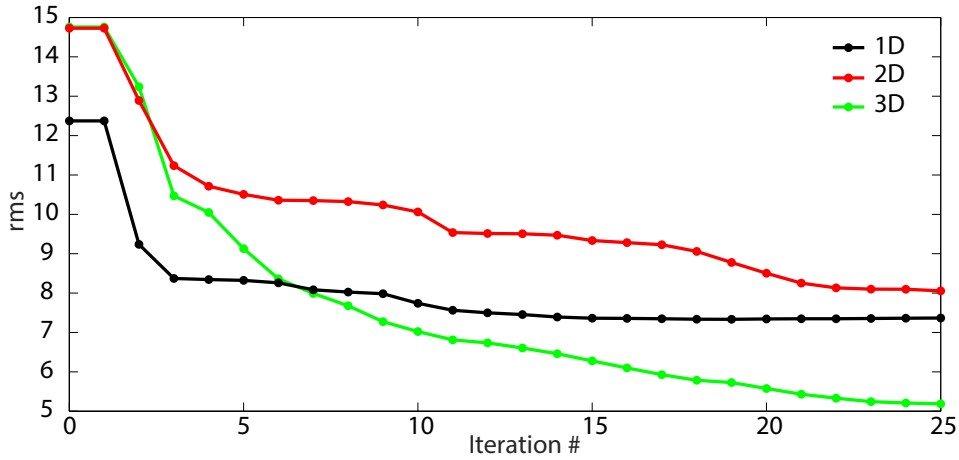

Figure 3.24: Development of the rms values for the three starting models.

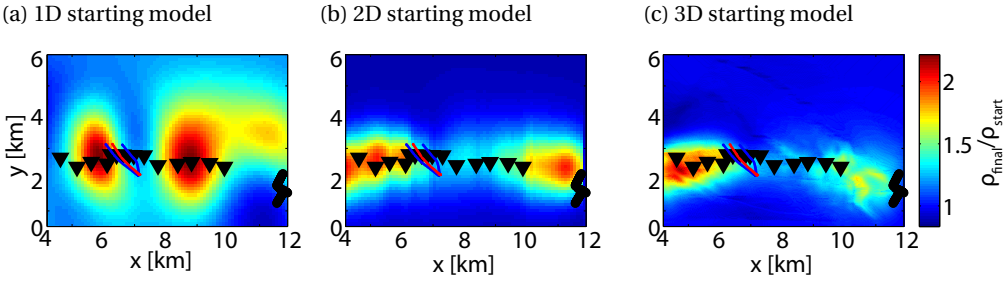

Figure 3.25: Map view of resistivity updates done by 3D inversion from (a) 1D, (b) 2D and (c) 3D starting model, extracted at the depths where starting resistivity is maximal, representing a layer of variable depth for the 2D and 3D starting models. Black triangles and lines indicate survey geometry and red and blue lines indicate well trajectories.

zones closer to the center of the array which are wider in y direction than the region that should be resolvable according to our sensitivity analysis (see Fig. 3.4).

Since our array is sparse and only 2D, the 3D inversion is highly influenced by the choice of starting models. The differences of the inversion results due to the complexity of the starting model indicate that inaccurate depth information is likely to be compensated by adapting the resistivity inside the reservoir. As Constable et al. (2014) stated, we confirm that a single model cannot be considered as "preferred", but multiple models together may provide a good understanding of the information contained in the data. However, acquisition imprints from source and receiver distributions and the (so far) disregarded impact of steel well casings and pipelines limit the resolution capability of the inversion, apparently more so than suggested by our synthetic studies. This can likely be attributed to a more complex structure of the true subsurface. Indications of small-scale resistivity variations near the steam injection well are not visible in the inversion results in Figures 3.19 - 3.25. Doubtlessly, denser sources and receivers with better areal coverage will better constrain the background resistivity, thereby providing a clearer and more accurate image of the reservoir. Nevertheless, the results give an indication of resistivity variations inside the reservoir. Incorporating seismic data acquired at the site in the EM data may reduce the uncertainty in our interpretation (MacGregor et al., 2012).

One complication that has not been considered in this study, but needs to be considered in future further interpretation of these data, is the effect of steel well casings and pipelines on the data (e.g. Kong et al., 2009; Swidinsky et al., 2013; Commer et al., 2015; Patzer et al., 2017). We observed a signal-enhancing effect on receiver R5 where a steel-cased borehole is near-by. Commer et al. (2015)) included highly conductive steel infrastructure in their earth modeling algorithms and confirmed our observations that these casings changes the signal distribution. Swidinsky et al. (2013)) showed the influence of steel borehole casings in the vicinity of a CSEM system and concluded that boreholes should either be positioned broadside with respect to the CSEM array or drilled at least 200 m away from the CSEM array to minimize the casing effects, which is conform to our observations.

3.5. CONCLUSIONS

Our modeling study on survey geometry, resolution analysis, and depth penetration using cumulative sensitivity show that small resistive anomalies can be recognized but their size and resistivity are difficult to recover. However, complex structures cannot be resolved when assuming real-data uncertainties or noise conditions.

We could show that the highly resistive Schoonebeek reservoir can be clearly identified using a simple line survey geometry and horizontal electric-field data. From the multiple 1D and 3D inversions carried out, we also find indications of resistivity variation within the reservoir. However, small-scale resistivity structure which may occur due to steam injection cannot be resolved using this data set alone.

Unconstrained 1D inversion can in general recover the correct reservoir depth. The introduction of fine layering around the predicted reservoir depth resulted in a geologically plausible 1D model that could be used as input for 3D inversion. Lateral variations and small resistive or conductive bodies inside the reservoir, however, could not be resolved as was already anticipated from the synthetic studies.

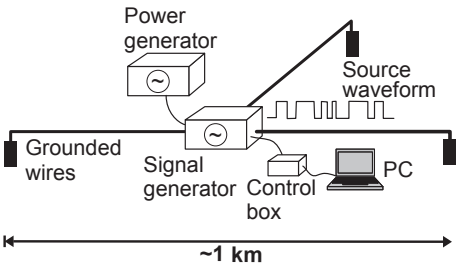

(a)

(b)

Figure 3.26: (a) Sketch of CSEM source (after Streich et al. (2010)). (b) Land CSEM transmitter; 400 V power generator (yellow) that supplies three-phase, 50 Hz AC current. Inside white trailer a high-power, high voltage programmable signal generator creates desired waveform.

Interpretation of the 3D structure in the obtained inversion models is difficult without further constraints. Most likely, the results show actual reservoir structure with an imprint of acquisition geometry. Unaccounted features from metal infrastructure may have further limiting effects.

To be able to detect small-scale resistivity variations or time-lapse changes induced due to hydrocarbon production or steam injection, we would require better EM data coverage and more accurate knowledge of the background resistivity model. Additional information can be gathered from well-logs, geological information, different EM data such as the vertical electric field E_z or from other geophysical data (e.g., seismic). Closer integration of the EM data with seismic data acquired at the site may further reduce the uncertainty in our interpretation.

APPENDICES

A. TRANSMITTER SPECIFICATIONS

The overall configuration of the transmitter can be seen in Figure 3.26. The CSEM transmitter developed by Metronix GmbH and the German Research Centre for Geosciences (GFZ) is powered by a 400 V generator that supplies three-phase 50-Hz alternating currents. The currents are fed into a programmable signal generator. Custom waveforms can be designed to spread the transmitted energy across a band of discrete frequencies in a more even manner than the linear amplitude decrease of the traditional square wave (Myer et al., 2011; Mittet and Schaug-Pettersen, 2008). During most of our survey we still use square wave signals with different source base frequencies, since this proved to be best suited for elevating signal levels above ambient noise levels in the survey area. The overall source strength is determined by the length of the grounded electric source wires(about 1 km for our survey, see Figure 3.1) and the current amplitudes that can reach up to 40 A. In Schoonebeek, the electrode contact resistances were reduced such that maximum currents of about 38 A were achieved.

The three-phase CSEM transmitter can easily generate multi-polarization signals. The three currents fed into the three grounded electrodes are phase-shifted to each other

by 120°. The current I_k on electrode $k \in \{1,2,3\}$ can be written as (Streich et al., 2013)

$$I_k = I_0 \cos[(k-1) * 120° + \phi] \tag{3.6}$$

where I_0 is the time-dependent source waveform and ϕ is the polarization angle. By electronically adjusting the polarization angle, multi-polarization fields are generated without redeploying the transmitter. Transmitter cable locations are recorded by GPS, and exact source geometry is included into forward calculation and data inversion (Streich et al., 2011).

B. RESPONSE FUNCTION CALCULATION

The electric field **E** in the frequency domain at position **r** is a superposition of the fields due to each part of the source and can be rewritten in terms of response functions according to (Streich et al., 2013)

$$\mathbf{E}(\mathbf{r}) = \sum_{k=1}^{3} I_k i\omega\mu_0 \int_{L_k} \bar{\bar{\mathbf{G}}}^{EJ}(\mathbf{r}|\mathbf{r}') \cdot d\mathbf{l}' = \sum_{k=1}^{3} I_k \mathbf{T}_k^{\mathbf{E}} \tag{3.7}$$

where $i = \sqrt{-1}$, ω is the angular frequency and μ_0 is the free-space magnetic permeability. The integration is carried out over the individual length of the grounded wires L_k and $\bar{\bar{\mathbf{G}}}^{EJ}$ is the Green's tensor for electric fields due to electric dipole sources. $\mathbf{T}_k^{\mathbf{E}}$ are the response functions for a given source geometry that are independent of the current waveform. They contain information on the subsurface resistivity, but cannot be measured directly. Convolving these response functions with the three source currents and superposing them (3.7) leads to the fields that are recorded. From equation (3.6) it follows that the three source currents are linearly dependent with

$$\sum_{k=1}^{3} I_k = 0. \tag{3.8}$$

Therefore, the response functions $\mathbf{T}_k^{\mathbf{E}}$ cannot be determined separately from each other and one of the currents has to be eliminated; in case I_3 is eliminated, we get:

$$\mathbf{E}(\mathbf{r}) = I_1(\mathbf{T}_1^{\mathbf{E}} - \mathbf{T}_3^{\mathbf{E}}) + I_2(\mathbf{T}_2^{\mathbf{E}} - \mathbf{T}_3^{\mathbf{E}}) = I_1\mathbf{T}_{1,3}^{\mathbf{E}} + I_2\mathbf{T}_{2,3}^{\mathbf{E}} \tag{3.9}$$

resulting in bivariate CSEM response functions $\mathbf{T}_{1,3}^{\mathbf{E}}$ and $\mathbf{T}_{2,3}^{\mathbf{E}}$. The relation between the horizontal electric-field data and the two source currents for one pair of currents and electric fields can be expressed in matrix form as

$$\begin{pmatrix} E_x \\ E_y \end{pmatrix} = \begin{pmatrix} T_{1,3}^{E_x} & T_{2,3}^{E_x} \\ T_{1,3}^{E_y} & T_{2,3}^{E_y} \end{pmatrix} \begin{pmatrix} I_1 \\ I_2 \end{pmatrix}. \tag{3.10}$$

The system of equations is highly over-determined with tens (for the lowest frequencies) to a few thousands (for the highest frequencies) of observations whereas all observations are explained by just a set of response functions T, i.e., a 2×2 matrix of complex value. We can determine response functions by a robust weighted least-squares averaging over

data from different source currents and source fundamental frequencies (Streich et al., 2013). Standard least-square processing is not robust, because a very small number of strongly biased data can lead to significant bias of the estimated parameters. Therefore, iteratively calculated weights are assigned to reduce the influence of outliers (Huber and Ronchetti, 1981). This is done by multiplying eq. 3.10 on both sides by $\begin{pmatrix} WI_1^* & WI_2^* \end{pmatrix}$ leading to

$$\begin{pmatrix} E_x WI_1^* & E_x WI_2^* \\ E_y WI_1^* & E_y WI_2^* \end{pmatrix} = \begin{pmatrix} T_{1,3}^{E_x} & T_{2,3}^{E_x} \\ T_{1,3}^{E_y} & T_{2,3}^{E_y} \end{pmatrix} \begin{pmatrix} I_1 WI_1^* & I_1 WI_2^* \\ I_2 WI_1^* & I_2 WI_2^* \end{pmatrix}, \tag{3.11}$$

where $W = \mathrm{diag}(w_i)$ are real valued data weights, * denotes the complex conjugate and $WI^* = \sum_{i=1}^N w_i I_i^* / \sum_{i=1}^N w_i$, with N being the number of observations. The determinant of the right most square matrix in eq. 3.11 is

$$\begin{vmatrix} I_1 WI_1^* & I_1 WI_2^* \\ I_2 WI_1^* & I_2 WI_2^* \end{vmatrix} = \frac{(\sum_{i=1}^N w_i |I_{1,i}|^2)(\sum_{i=1}^N w_i |I_{2,i}|^2) - |\sum_{i=1}^N w_i (I_{1,i} I_{2,i}^*)|^2}{(\sum_{i=1}^N w_i)^2} \neq 0 \tag{3.12}$$

and thus the matrix in the right-hand side of eq. 3.11 is invertible and the least-squares problem solvable. Data points that poorly fit an expected robust distribution are assigned smaller weights. How to determine these weights for the robust weighting is explained in detail by Egbert and Booker (1986) and Chave and Thomson (1989).

REFERENCES

Brown, V., G. M. Hoversten, and K. Key, 2012, Seismically regularized controlled-source electromagnetic inversion: Geophysics, **77(1)**, E57–E65.

Butler, D. B., and R. J. Knight, 1995, The effect of steam quality on the electrical behavior of steam-flooded sands: A laboratory study: Geophysics, **60**, 998–1006.

Byrd, R. H., P. Lu, J. Nocedal, and C. Zhu, 1995, A Limited Memory Algorithm for Bound Constrained Optimization: SIAM Journal on Scientific Computing, **16**, 1190–1208.

Chave, A. D., and D. J. Thomson, 1989, Some comments on magnetotelluric response function estimation: J. Geophys. Res, **94**, 215–14.

Commer, M., G. M. Hoversten, and E. S. Um, 2015, Transient-electromagnetic finite-difference time-domain earth modeling over steel infrastructure: Geophysics, **80**, E147–E162.

Commer, M., and G. A. Newman, 2008, New advances in three-dimensional controlled-source electromagnetic inversion: Geophysical Journal International, **172**, 513–535.

Constable, S., 2010, Ten years of marine CSEM for hydrocarbon exploration: Geophysics, **75**, 75A67–75A81.

Constable, S., A. Orange, and K. Key, 2014, And the geophysicist replied: "Which model do you want?": Geophysics, **80**, E197–E212.

Constable, S., and C. J. Weiss, 2006, Mapping thin resistors and hydrocarbons with marine EM methods: Insights from 1D modeling: Geophysics, **71**, G43–G51.

Constable, S. C., R. L. Parker, and C. G. Constable, 1987, Occam's inversion: a practical algorithm for generating smooth models from electromagnetic sounding data: Geophysics, **52**, 289–300.

Darnet, M., M. C. K. Choo, R. . Plessix, M. L. Rosenquist, K. Yip-Cheong, E. Sims, and J. W. K. Voon, 2007, Detecting hydrocarbon reservoirs from CSEM data in complex settings: Application to deepwater Sabah, Malaysia: Geophysics, **72**, WA97–WA103.

deGroot Hedlin, C., and S. Constable, 1990, Occam's inversion to generate smooth, two-dimensional models from magnetotelluric data: Geophysics, **55**, 1613–1624.

Dell'Aversana, P., S. Colombo, B. Ciurlo, J. Leutscher, and J. Seldal, 2012, CSEM data interpretation constrained by seismic and gravity data: An application in a complex geological setting: First Break, **30**, 43–52.

Egbert, G. D., and J. R. Booker, 1986, Robust estimation of geomagnetic transfer functions: Geophysical Journal International, **87**, 173.

Ellingsrud, S., T. Eidesmo, S. Johansen, M. Sinha, L. MacGregor, and S. Constable, 2002, Remote sensing of hydrocarbon layers by seabed logging (SBL): Results from a cruise offshore Angola: The Leading Edge, **21**, 972–982.

Fanavoll, S., P. T. Gabrielsen, and S. Ellingsrud, 2014, CSEM as a tool for better exploration decisions: Case studies from the Barents Sea, Norwegian Continental Shelf: Interpretation, **2**, SH55–SH66.

Farquharson, C. G., and D. W. Oldenburg, 1998, Non-linear inversion using general measures of data misfit and model structure: Geophysical Journal International, **134**, 213–227.

Grayver, A., R. Streich, and O. Ritter, 2013, Three-dimensional parallel distributed inversion of CSEM data using a direct forward solver: Geophysical Journal International, **193**, 1432–1446.

Grayver, A. V., R. Streich, and O. Ritter, 2014, 3D inversion and resolution analysis of land-based CSEM data from the Ketzin CO2 storage formation: Geophysics, **79**, E101 E114.

Haber, E., U. M. Ascher, and D. Oldenburg, 2000, On optimization techniques for solving nonlinear inverse problems: Inverse problems, **16**, 1263.

Hornman, K., and E. Forgues, 2013, Permanent reservoir monitoring with onshore surface seismic: Presented at the Second EAGE Workshop on Permanent Reservoir Monitoring 2013–Current and Future Trends.

Huber, P., and E. Ronchetti, 1981, Robust Statistics, ser: Wiley Series in Probability and Mathematical Statistics. New York, NY, USA, Wiley-IEEE, **52**, 54.

Key, K., 2009, 1D inversion of multicomponent, multifrequency marine CSEM data: Methodology and synthetic studies for resolving thin resistive layers: Geophysics, **74**, F9–F20.

———, 2012, Marine electromagnetic studies of seafloor resources and tectonics: Surveys in Geophysics, **33**, 135–167.

Klose, R., G. Schmidt, O. Ritter, and G. Dawes, 2011, What is SPAM four for?: Protokoll über das 24. Schmucker-Weidelt-Kolloquium für Elektromagnetische Tiefenforschung, 24. Schmucker-Weidelt-Kolloquium für Elektromagnetische Tiefenforschung (Neustadt a. d. Weinstraße 2011), 127–134.

Kong, F. N., F. Roth, P. A. Olsen, and S. O. Stalheim, 2009, Casing effects in the sea-to-borehole electromagnetic method: Geophysics, **74**, F77–F87.

Li, Y., and D. W. Oldenburg, 1998, 3-D inversion of gravity data: Geophysics, **63**, 109–119.

MacGregor, L., S. Bouchrara, J. Tomlinson, U. Strecker, J. Fan, X. Ran, and G. Yu, 2012, Integrated analysis of CSEM, seismic and well log data for prospect appraisal: A case study from West Africa: First Break, **30**, 77–82.

Mansure, A. J., R. F. Meldau, and H. V. Weyland, 1993, Field examples of electrical resistivity changes during steamflooding: SPE Formation Evaluation, **8**, 57–64.

Michou, L., T. Coléou, and Y. Lafet, 2013, 4D Seismic inversion on continuous land seismic reservoir monitoring of thermal EOR: 75^{th} EAGE Conference & Exhibition. (Extended Abstract).

Mittet, R., and T. Schaug-Pettersen, 2008, Shaping optimal transmitter waveforms for marine CSEM surveys: Geophysics, **73**, F97–F104.

Mulder, W., 2006, A multigrid solver for 3D electromagnetic diffusion: Geophysical Prospecting, **54**, 633–649.

Myer, D., S. Constable, and K. Key, 2011, Broad-band waveforms and robust processing for marine CSEM surveys: Geophysical Journal International, **184**, 689–698.

Myer, D., S. Constable, K. Key, M. E. Glinsky, and G. Liu, 2012, Marine CSEM of the Scarborough gas field, Part 1: Experimental design and data uncertainty: Geophysics, **77**, E281–E299.

Newman, G. A., 2014, A review of high-performance computational strategies for modeling and imaging of electromagnetic induction data: Surveys in Geophysics, **35**, 85–100.

Oldenburg, D. W., E. Haber, and R. Shekhtman, 2013, Three dimensional inversion of multisource time domain electromagnetic data: Geophysics, **78**, E47–E57.

Patzer, C., K. Tietze, and O. Ritter, 2017, Steel-cased wells in 3-D controlled source EM modelling: Geophysical Journal International, **209**, 813.

Plessix, R. E., M. Darnet, and W. A. Mulder, 2007, An approach for 3D multisource, multifrequency CSEM modeling: Geophysics, **72**, SM177–SM184.

Plessix, R. E., and W. A. Mulder, 2008, Resistivity imaging with controlled-source electromagnetic data: Depth and data weighting: Inverse Problems, **24**, 034012 (22pp).

Ritter, O., A. Junge, and G. J. Dawes, 1998, New equipment and processing for magnetotelluric remote reference observations: Geophysical Journal International, **132**, 535–548.

Rondeel, H., D. Batjes, and W. Nieuwenhuijs, 1996, Geology of Gas and Oil under the Netherlands: Springer Netherlands. (as Rondeel, H.E., Batjes, D.A.J., Nieuwenhuijs, W.H., Synopsis: Petroleum Geology of the Netherlands - 1993).

Salako, O., C. MacBeth, and L. MacGregor, 2015, Potential applications of time-lapse CSEM to reservoir monitoring: First Break, **33**, 35–46.

Schwarzbach, C., and E. Haber, 2013, Finite element based inversion for time-harmonic electromagnetic problems: Geophysical Journal International, **193**, 615–634.

Streich, R., 2016, Controlled-Source Electromagnetic Approaches for Hydrocarbon Exploration and Monitoring on Land: Surveys in Geophysics, **37**, 47–80.

Streich, R., and M. Becken, 2011, Sensitivity of controlled-source electromagnetic fields in planarly layered media: Geophysical Journal International, **187**, 705–728.

Streich, R., M. Becken, U. Matzander, and O. Ritter, 2011, Strategies for land-based controlled-source electromagnetic surveying in high-noise regions: The Leading Edge, **30**, 1174–1181.

Streich, R., M. Becken, and O. Ritter, 2010, Imaging of CO2 storage sites, geothermal reservoirs, and gas shales using controlled-source magnetotellurics: Modeling studies: Chemie der Erde - Geochemistry, **70**, 63–75.

———, 2013, Robust processing of noisy land-based controlled-source electromagnetic data: Geophysics, **78**, E237–E247.

Swidinsky, A., R. N. Edwards, and M. Jegen, 2013, The marine controlled source electromagnetic response of a steel borehole casing: Applications for the NEPTUNE Canada gas hydrate observatory: Geophysical Prospecting, **61**, 842–856.

Tietze, K., O. Ritter, and P. Veeken, 2015, Controlled-source electromagnetic monitoring of reservoir oil saturation using a novel borehole-to-surface configuration: Geophysical Prospecting, **63**, 1468–1490.

Tøndel, R., H. Schütt, S. Dümmong, A. Ducrocq, R. Godfrey, D. LaBrecque, L. Nutt, A. Campbell, and R. Rufino, 2014, Reservoir monitoring of steam-assisted gravity drainage using borehole measurements: Geophysical Prospecting, **62**, 760–778.

Wirianto, M., W. A. Mulder, and E. C. Slob, 2010, A feasibility study of land CSEM reservoir monitoring in a complex 3-D model: Geophysical Journal International, **181**, 741–755.

Zhdanov, M. S., M. Endo, L. H. Cox, M. Čuma, J. Linfoot, C. Anderson, N. Black, and A. V. Gribenko, 2014, Three-dimensional inversion of towed streamer electromagnetic data: Geophysical Prospecting, **62**, 552–572.

4

REPEATABILITY ANALYSIS OF A LAND TIME-LAPSE CONTROLLED-SOURCE EM SURVEY

Profound knowledge of the resistivity distribution inside the reservoir can help during production of an oil or gas field to evaluate dynamic processes inside this target zone. A way of monitoring these changes is the use of the Controlled-Source ElectroMagnetic (CSEM) method. Therefore, land CSEM time-lapse measurements were carried out on top of the Schoonebeek oil field in the Netherlands to evaluate its potential for monitoring reservoir changes due to steam injection. A baseline and two repeat surveys, consisting of two transmitters and fifteen receiver stations, were realized over a period of nearly two years. This time range is too short to expect resistivity changes in the reservoir to be detectable in surface stations but is well suitable for testing the repeatability of the baseline survey, a crucial requirement for successful future time-lapse measurements. The data sets were acquired using the same transmitter and receiver locations and were identically processed to minimize geometry and processing effects between the three surveys. Technical challenges due to high cultural EM noise, near-surface heterogeneities and large metallic objects in the vicinity of the receiver and source locations led to complex data interpretation. Repeatability analysis showed that the electric-field data obtained from the three surveys are within a few percent to each other for most of the receiver stations. We have found that due to the inhomogeneous near-subsurface and especially due to abundant metallic objects in the ground, even minor discrepancies in the actual receiver position of less than 1 m may lead to significant changes in the measured electric field and thus proper source handling and accurate receiver repositioning are essential for obtaining good repeatability.

4.1. INTRODUCTION

One method used for enhanced oil recovery (EOR) is the so-called steam-assisted gravity drainage (SAGD) where high-pressure steam is injected into the reservoir to stimulate

oil drainage into a lower, laterally offset wellbore. The efficiency of the oil displacement mainly depends on the oil's viscosity, rock characteristics and on the pattern of injectors and producers. Thus, effective reservoir management requires close monitoring of the steam evolution during injection and production to avoid a heterogeneous and inefficient displacement process with areas of bypassed oil and to detect possible unwanted leakages (Salako et al., 2015).

The preferred geophysical method that is routinely applied for production monitoring is the seismic technique, due to its wave-field nature. This method has recently been successfully applied for steam injection monitoring (Michou et al., 2013). However, this may require substantial experimental effort (Zwartjes et al., 2015) so developing less expensive monitoring techniques is desirable.

Another geophysical method that is promising for time-lapse measurements and can provide information that supplements 4D seismic techniques is the Controlled-Source ElectroMagnetic (CSEM) method (e.g. Orange et al., 2009; Constable, 2010). While the seismic method is sensitive to pressure effects, the CSEM method is sensitive to strong changes in the resistivity of the subsurface. The CSEM method is able to detect changes in fluid saturation and salinity between injected and displaced fluids that may have insufficient seismic property contrast to distinguish hydrocarbon-bearing from steam-saturated rocks (Lien and Mannseth, 2008; Orange et al., 2009; Wright et al., 2002). This makes the CSEM method potentially suitable for reservoir monitoring, provided that the resistivity change can be detected in the presence of repeatability errors and noise. Wirianto et al. (2010) numerically modeled time-lapse changes using the rather complex SEG/EAGE overthrust model (Aminzadeh et al., 1997) for an oil reservoir in the model much deeper than the Schoonebeek field. Although the physical changes in their model due to water injection were quite dramatic, they did not find very large time-lapse signals. In addition, they looked at slightly less perfect displacement of oil by water and the time-lapse signal disappeared almost completely. However, they showed that time-lapse changes may be detectable with the proper setup for their deep reservoir. Since the EM field is diffusive for the frequency range used in the CSEM method (about 0.1 to 10 Hz), the spatial resolution capability is low.

While continuous EM recordings on a larger scale are quite common, time-lapse CSEM reservoir monitoring on land is rather new and studies with real-data issues are rare in the literature (Girard et al., 2011; Tietze et al., 2015; Vilamajó et al., 2015).However, a small number of synthetic feasibility studies on land CSEM monitoring have been published (Wirianto et al., 2010; Colombo and McNeice, 2013; Tietze et al., 2015; Vilamajó et al., 2015). From these studies, it can be concluded that the absolute difference signal magnitude of the EM signal appears sufficient to be detectable with current acquisition design and available hardware. However, these past studies seem to be too optimistic by either assuming best-case scenarios or by downplaying noise issues and overestimating the available hardware.

Wave-field methods such as the seismic method are frequently used in parallel with other geophysical methods such as diffusive-field methods (e.g., CSEM methods) or potential-field methods (e.g., gravity methods) for a joint interpretation or joint inversion of the data with the objective of enhancing depth resolution and improving subsurface characterization (e.g., Den Boer et al., 2000; Haber and Oldenburg, 1997; Abubakar

et al., 2012; Brown et al., 2012; MacGregor et al., 2012; Liang et al., 2012). Combining such geophysical methods may lead to better-constrained subsurface models.

In this chapter, we focus on the repeatability potential of land CSEM measurements and highlight the importance of high-accuracy and high-quality measurements. Therefore, a land CSEM survey and two repeat surveys were acquired at the heavy oil-field of Schoonebeek in the Netherlands, where steam is injected into the hydrocarbon reservoir as an EOR method. Pre-existing knowledge of the reservoir depth, structure and thickness can provide constraints to the CSEM method. Thus, CSEM can be applicable in regions with well-known geological settings such as the producing oil field in Schoonebeek.

The Schoonebeek area was chosen for time-lapse repeatability studies to test the potential of the CSEM method to replace and/or support the seismic method for reservoir monitoring. Since the three surveys were acquired over a time period of less than two years, only minor changes in the measured electromagnetic signal due to the injected steam are expected (<1-2%) as highlighted in Streich (2016) in Figure 11 for a time period of 7 months using resistivity estimated from reservoir simulation data and petrophysical relations. In addition, resistivity changes are expected to be complex with anticipated regions of increased resistivity near the injection well as a consequence of gradually condensing steam and mixing with saline formation water, and decreased resistivity away from the injector as a consequence of the displacement of highly resistive oil. However, the rise in temperature, especially near the injection wells, may counterbalance most of the resistivity increase (Salako et al., 2015; Batzle and Wang, 1992). As steam injection generally includes several processes, the entire process is rather complex (Tøndel et al., 2014). Since steam injection was stopped in June 2015 and only resumed after completion of the third survey, the period of the actual steam injection during the surveys was about 1.3 years and the expected changes inside the reservoir are likely too small to be detectable by the horizontal electric-field data which are not sensitive enough to deal with such small changes. In this chapter, we want to study the influence of the mentioned challenges on data acquisition and on the repeatability of the measurements. Recorded changes in the data are likely linked to near-surface effects that may be altered due to different weather conditions, due to errors in receiver and source positions or due to different source polarization used while transmitting. Further, the repeatability studies were used to optimize the setup to detect minor time-lapse changes in future time-lapse measurements.

We expect the changes due to steam injection to be too small to be visible in the raw field data given the ambient EM noise levels. Changes, however, may be detectable in inversion results since information related to steam injection may still be present in the data albeit hidden in the data. Therefore, the results will primarily be analyzed with respect to the repeatability of the survey, but we will also examine if EM signal changes between the surveys may be related to the injection of steam.

4.2. MODELING CSEM TIME-LAPSE POTENTIAL

Modeling studies were performed considering the acquisition setup discussed in Chapters 2 and 3. Although time-lapse changes in the real-data example are expected to be too small to be detectable, we focus the modeling study on the ability to detect small

resistivity changes with the proposed land CSEM method and acquisition setup. We simulate simple 1D examples with either increasing or decreasing reservoir resistivity to better understand how resistivity variations due to steam injection may influence measurements in real data. Further, we show why time-lapse measurements are needed if we want to see small changes in the resistivity structure. Inversion by iterative forward modeling was done using the modeling code described in Chapter 3 (Streich and Becken, 2011; Streich et al., 2011; Hunziker et al., 2015; Mulder, 2006; Plessix et al., 2007). For a more detailed description of the inversion algorithms, the reader is referred to Chapter 3.

To better understand the influence of resistivity variations on the measurements, we simulate simple 1D synthetic examples with either increasing or decreasing reservoir resistivity. The assumption of 1D may highly overestimate changes compared to more realistic regionally confined 3D bodies. However, they give a good general picture about the influence of resistivity changes in the reservoir layer on measurable changes in the field at receiver level. For modeling time-lapse scenarios, we used the same 1D background model consisting of horizontal plane layers with a reservoir at 785 m depth as defined in Chapter 3. We first tested the capability of the proposed acquisition setup to monitor time-lapse changes. Therefore, results for a synthetic time-lapse 1D example for three receiver stations R2, R8 and R13 are shown in Figure 4.1. Figures 4.1a,c,e show electric-field amplitudes of $E^{timelapse}$ (SBK2) and E^{base} (SBK1) for a unit source current and one particular source polarization at source location T1 whereas Figures 4.1b,d,f show the differences of the electric-field amplitudes compared to the base case with reservoir resistivity of 200 Ωm. For the repeat survey, it is assumed that the reservoir resistivity of the base survey either increases to 250 Ωm or decreases to 167 Ωm. Small changes inside the reservoir either increase or decrease the modeled amplitudes depending on the frequency value by up to 10-15%.

Since time-lapse changes are complex and take place in a 3D Earth, we also simulated 3D changes. Therefore, two data sets were generated using the initial models as shown in Figure 4.2 and two small 3D bodies inside the reservoir, representing two zones with increased resistivity (Figure 4.3). On the left-hand side (Figure 4.3a, c and e), the imaged resistivity distribution inside the reservoir is shown that was obtained when using the correct background model as the initial model for our inversion (Figure 4.2a). On the right-hand side (Figure 4.3b, d and f), we show the resistivity distribution obtained inside the reservoir when taking a background model where reservoir resistivity was decreased by 50 Ωm as the initial model for our inversion (Figure 4.2b). For both survey times t_0 and t_1, the same starting model was used. Figure 4.3a depicts a depth slice inside the reservoir that shows the resistivity distribution after inversion for a model with two small bodies of dimension 200 m × 200 m × 18 m and ρ_h = 200 Ωm, ρ_v = 333 Ωm (shown as black squares). The scale of structures that can be resolved by the inversion is limited by the smoothness constraint and, as expected, the size of the body is too small to get a good estimate of the size and amplitude of this body with the setup used in Schoonebeek where the receiver spacing is up to 630 m. If the size of the bodies increases to 500 m × 500 m × 18 m (Figure 4.3c), the bodies are resolved much better and a good hint of their location and shape is given. When looking at the differences between the two scenarios, i.e. treating the scenario as a time-lapse example where a more resistive and a more conductive fluid is injected into the reservoir and two surveys are taken at time

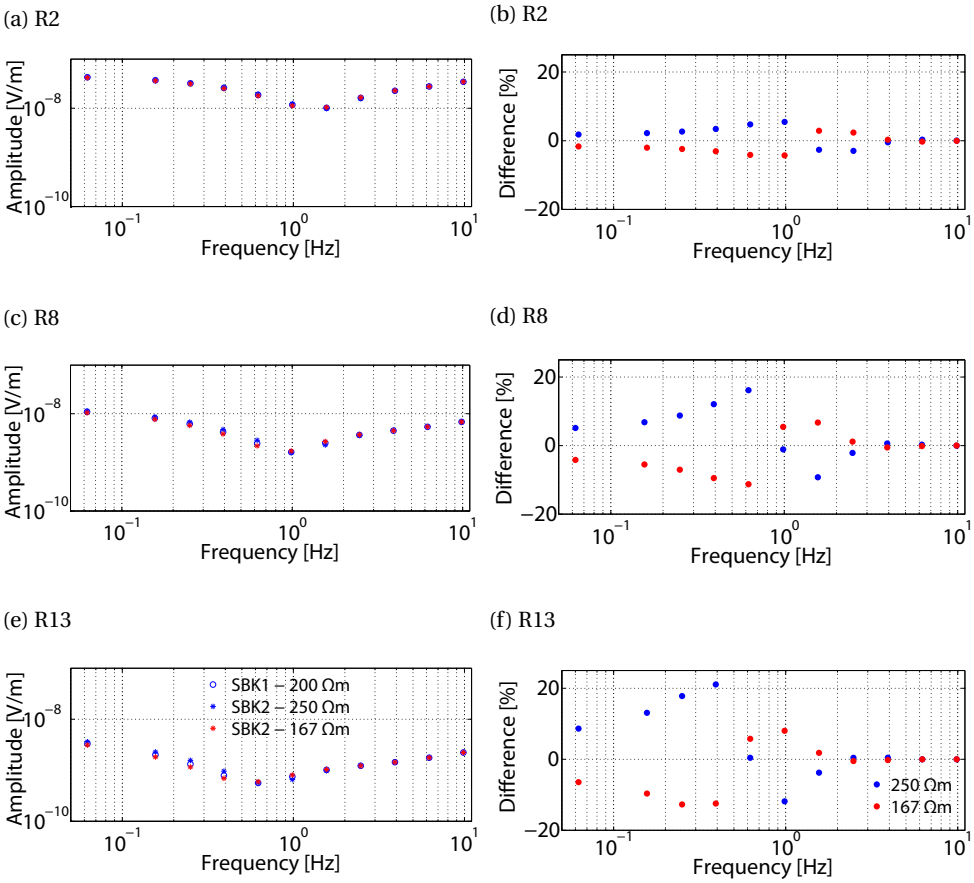

Figure 4.1: Synthetic time-lapse examples for three receiver stations (R2, R8 and R13 (see Figure 3.1)). (a), (c) and (e): electric-field amplitudes of $E_y^{timelapse}$ (SBK2) and E_y^{base} (SBK1) for unit source current and a source polarization of 30° at source location T1. (b), (d) and (f): Differences of electric-field amplitudes compared to base case with reservoir resistivity of 200 Ωm, i.e. $(E_y^{timelapse} - E_y^{base})/E_y^{base}$. For the repeat survey, it is assumed that the reservoir resistivity of the base survey either increases to 250 Ωm or decreases to 167 Ωm.

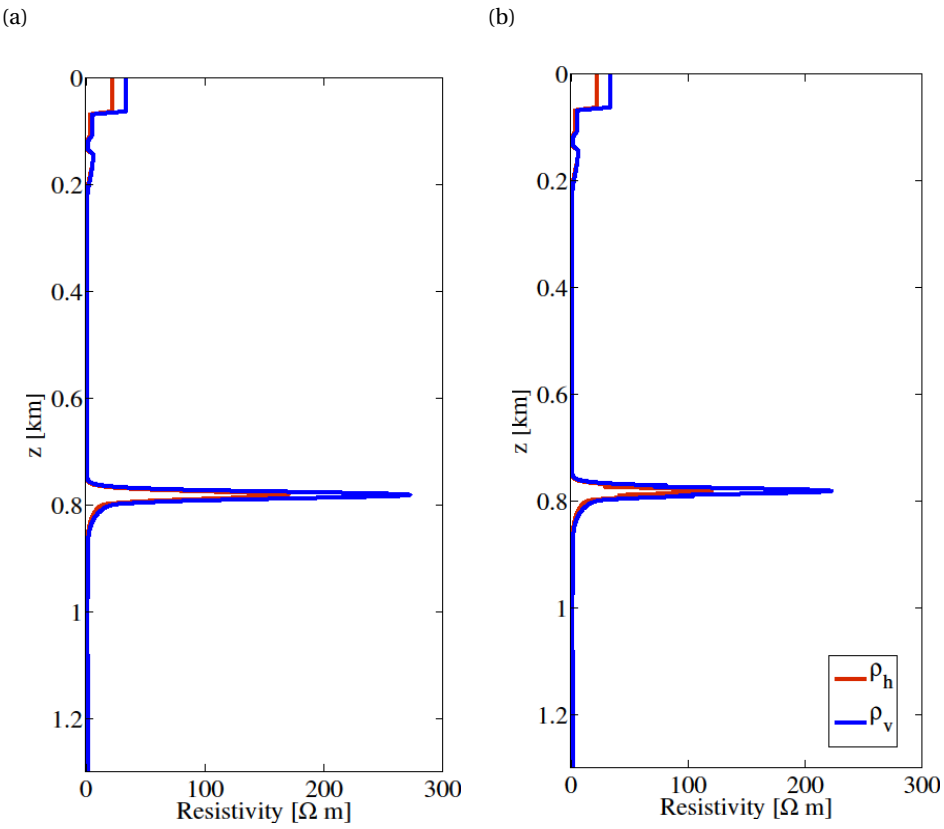

Figure 4.2: Starting 1D models for 3D inversion (a) for Figure 4.3a, c, and e; (b) for Figure 4.3b, d and f.

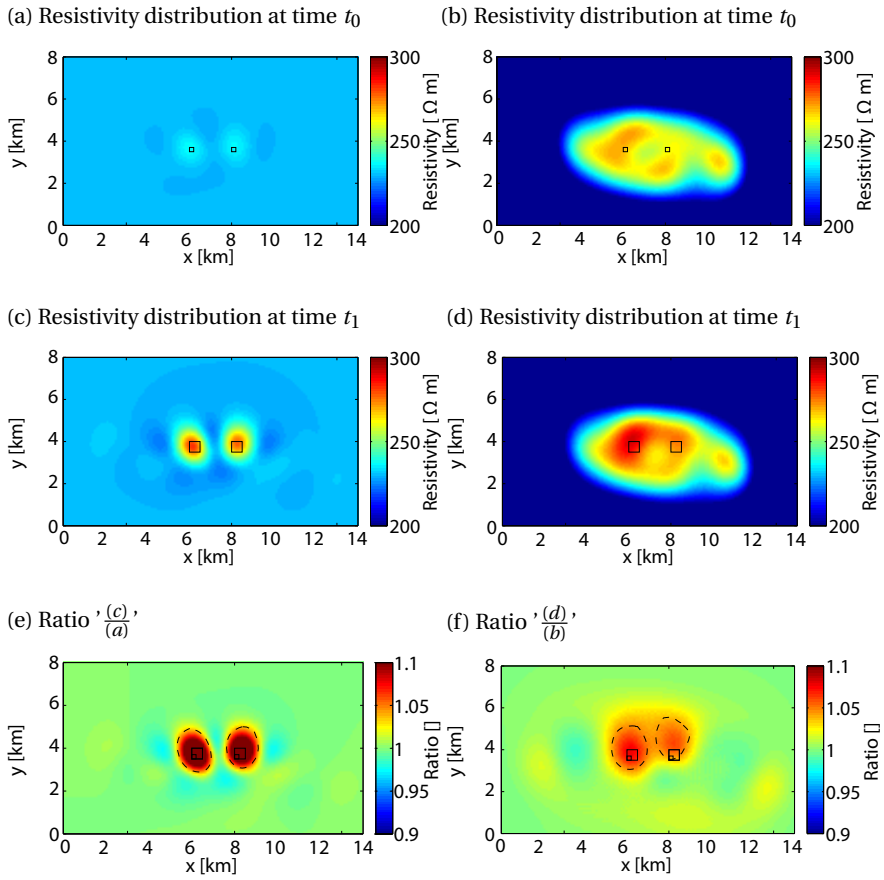

Figure 4.3: Synthetic time-lapse scenario showing resistivity distribution inside the reservoir layer at (a) and (b) time t_0 and (c) and (d) time t_1. Two resistive bodies with dimensions 200 m × 200 m × 18 m are simulated in (a) and (b). The body volume grows over time $t_1 - t_0$ to 500 m × 500 m × 18 m which is simulated in (c) and (d). Black squares indicate the extent of the two bodies. The ratios between the two scenarios are shown in (e) and (f), respectively. As starting model for the inversions, in (a), (c), and (e) the correct background model was used (Figure 4.2a); in (b), (d) and (f) the reservoir resistivity in the background model was decreased by 50 Ωm (Figure 4.2b).

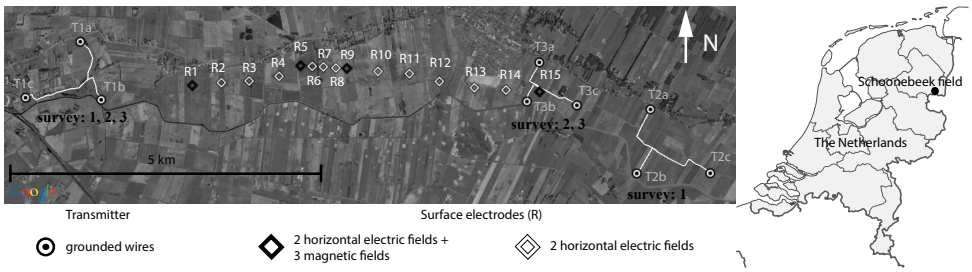

Figure 4.4: Location of field survey and detailed survey layout. Receivers are oriented in a west-east direction. Transmitters are located west and east of receiver line. Transmitter 1 west of receiver line is used for all surveys. Transmitter 2 was shifted to location of transmitter 3 after the first survey.

4

t_0 (base survey) and t_1 (repeat survey), we clearly see the relative change in resistivity at the location of the two bodies. Figure 4.3e shows the ratio between the two scenarios. Overall, the bodies are well visible and the locations of the bodies are well defined if the background resistivity distribution (inside the reservoir) is known. If the starting model was wrongly chosen (Figure 4.3b, d and f), the resistivity and size of the small bodies cannot be resolved and the two bodies cannot be distinguished by the inversion process suggesting that the results depend heavily on the reliability of the background model. The ratio plot, however, gives a good indication of the existence of the two resistive bodies. The boundaries of the objects after inversion, indicated by black dashed lines, were in the following defined such that they coincide with a resistivity change of 5% from the resistivity distribution at time t_0. Both inversions (Figures 4.3e and 4.3f) detect the resistivity change and can resolve the bodies in resistivity and location although the vertical and lateral extent of the bodies are slightly larger than their true extent. Thus, in time-lapse measurements, resistivity changes due to the growth of the bodies are well recognizable and locatable in this example. Even for small volume changes, not resolvable by the CSEM method alone, time-lapse measurements may still give reasonable results thus showing that time-lapse changes are visible with the proposed setup.

Although the expected changes are small, we have shown that by using ratios after inversion the changes are detectable and thus information about time-lapse changes is contained in the data. CSEM time-lapse measurements may thus have the advantage to detect changes that cannot be seen in other geophysical data sets.

4.3. RESULTS FROM REPEATABILITY MEASUREMENTS

For monitoring studies, it is crucial to have good repeatability between the field survey measurements commonly affected by noise and technical limitations. We expect only minor changes of maximal 1-2% in the data due to changes inside the reservoir layer between the three surveys. This might be too low to be detectable in the data assuming the high EM-noise levels as discussed in Chapter 3. In the following, a time-lapse land CSEM survey is discussed.

4.3.1. BASE AND MONITORING FIELD SURVEYS

The Schoonebeek field is a heavy oil field in the northwest Netherlands where steam-assisted gravity drainage is used for EOR. Three CSEM field surveys were carried out between 27 January - 7 February 2014, 17 November - 5 December 2014 and 16 November - 4 December 2015. Figure 4.4 shows the location of the three surveys (also referred to as SBK1, SBK2, and SBK3). The survey layout consists of 15 receiver stations at the surface. At 11 stations only the horizontal electric field components E_x and E_y were measured. In addition to the two horizontal electric-field components, the 3 magnetic field components were measured at the remaining 4 stations by deploying induction coils. All receivers were dismantled at the end of each survey and were set up at the same positions (where receiver mid points were kept identical, but individual sensor locations could not be repeated exactly as they were not measured during the first survey) at the beginning of the successive survey.

Two transmitter locations were chosen for each survey. Transmitter 2 was moved towards the receiver array after completion of the first survey because noise levels were found to be too high for the longer offsets. At each position, the source transmitted currents with amplitudes up to ~38 A at 560 V for a total of 15-20 hours during ~3-4 days. To acquire useful CSEM data with sufficiently high signal-to-noise ratio, we transmitted square-wave signals at different base frequencies. We transmitted periods of 16, 8, 4, 2, 0.5 s to sample the entire frequency band that gives us information on the reservoir at good signal strength. Because initial setup and testing took longer during survey 1, overall transmission time was shorter than during survey 2. The transmitted signal periods of the first and the two repeat surveys were slightly different. Long-period transmission sequences were repeated during survey 1 in order to assure that all receivers on the vertical array acquired sufficient data, including receivers that temporarily failed. This left relatively little time for transmitting signal at other periods. Long sequences of the 16-s signal were also transmitted during survey 2 and survey 3, yet there was time for transmitting additional source signals with shorter periods and thus improve signal-to-noise ratios at mid-range frequencies. In addition, during survey 1, we mainly transmitted signal at a few distinct source polarizations. This was a deviation from the original plan in order to allow for easier quality control during the survey (e.g., real-time stacking to make low-amplitude signals visible). During survey 2 and survey 3, when data quality appeared reasonably good, we reverted to the original plan and mostly let the source polarization rotate continuously at very long rotation periods (between 256 to 2048 times the periods of the source wavelets).

Source cables were GPS-tracked to allow for correct re-positioning. Receiver and source positioning was improved during the study period by more accurate measurement procedures as discussed in section 4.4.3 where aspects about the field setup that were found to affect the repeatability of the surveys are discussed. During survey 1 and 2, continuous steam injection and production led to strong cultural EM noise.

An unscheduled long-term production stop after the survey 2, increased the signal-to-noise ratio due to non-operating oil-field production infrastructure such as pumps. For further details about survey design, the reader is referred to Chapters 2 and 3.

4.3.2. PROCESSING

The data of all three surveys were identically processed following the procedure highlighted in Chapter 3 and Streich et al. (2013) to ensure best possible consistency between the processed data from the three surveys. The processing parameters were chosen such that the response functions (TF, 'transfer functions', termed like this in analogy to magnetotelluric transfer functions, but denoting here the transfer or response function between the generated CSEM signal and the recorded EM data) of each receiver and survey showed lowest error estimates. A Notch filter was applied to remove the 50 Hz signal and the associated harmonics. The TF for both horizontal electric fields E_x and E_y, and two source current combinations were processed and TF amplitudes and phases of all surface receivers were calculated for two chosen polarizations with the best signal-to-noise ratio for transmitter T1 and T3. Data from transmitter T3 could not be explained with 1D models and we suspect that transmitter T3 showed complex 3D effects most likely due to short source-receiver offsets for most of the receivers and thus 1D inversions were focused on data from transmitter T1. For all surveys and for all available source periods, the TF amplitudes and phases of the response function $T_{2,3}^{E_y}$ (see Section 3.4.2 in Chapter 3 for explanation of the notation) including their uncertainty estimates are plotted in Figure 4.5 for receiver R14 and source position T1, a source-receiver combination with large offsets. Uncertainties for the second and third survey are lower over the entire frequency spectrum, as can be seen by comparing Figure 4.5b and Figure 4.5c with Figure 4.5a. This indicates higher signal-to-noise ratios of the repeat surveys, which likely is a result of (1) the broader range of source signal periods that were transmitted during the second survey, (2) the longer overall transmission times and/or (3) the stop in oil production during the 3^{rd} survey observable by an increased signal-to-noise ratio between survey 2 and survey 3.

As mentioned above, square-wave signals with a range of base frequencies were transmitted. Different base frequencies have different odd harmonics. In order to process and interpret data from different source fundamental frequencies together, a fixed set of analysis frequencies is chosen on the basis of the different acquisition frequencies. Data were split into short time windows, and transformed to and stacked in the frequency domain to effectively remove time-variable noise. It was done by stacking all data within narrow frequency bands by interpolating the affected frequencies to a centered analysis frequency. The interpolation is necessary to align the different frequencies and different rotation frequencies used for each survey. This is achieved by choosing 14 analysis frequencies for further processing. However, we observed that interpolation led to small differences when using data originating from different base frequencies. To avoid inaccuracies and to allow the best comparability of the surveys, only data from base frequencies of 1/16 Hz and 1/4 Hz, which were chosen base frequencies during all surveys and recorded by all receivers, were used. Since recorded base frequencies of transmitter T3 were the same for survey 2 and 3, all available base frequencies could be used for this transmitter. We further observed that the overall amount of data (i.e., recording time per base frequency) appeared to have little influence on the error estimates.

In addition, some source signals were programmed to rotate in order to allow for a broad range of source polarizations leading to different source polarization directions between the two surveys. However, using different source polarizations and slow rota-

(a)

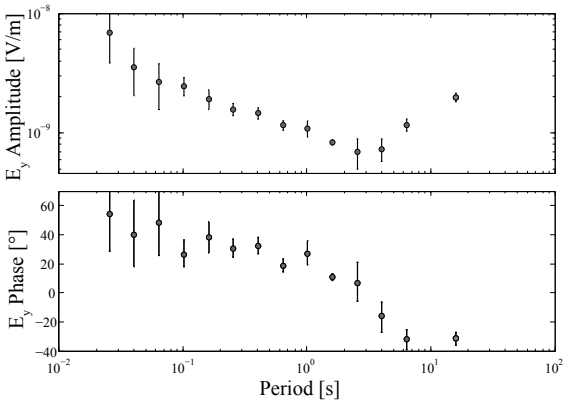

(b)

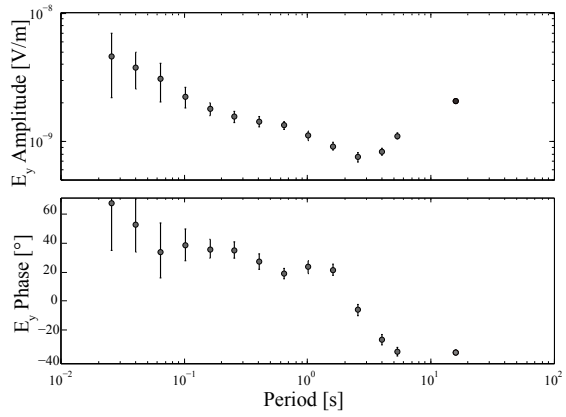

(c)

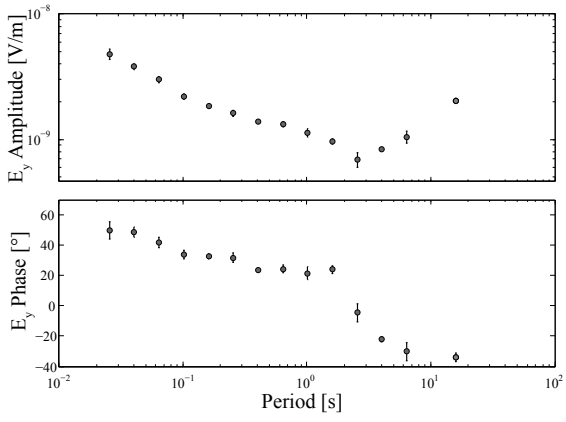

Figure 4.5: Amplitude and phase of $T_{2,3}^{E_y}$ including uncertainty estimates for (a) 1^{st}, (b) 2^{nd} and (c) 3^{rd} survey for receiver position R14 and transmitter T1.

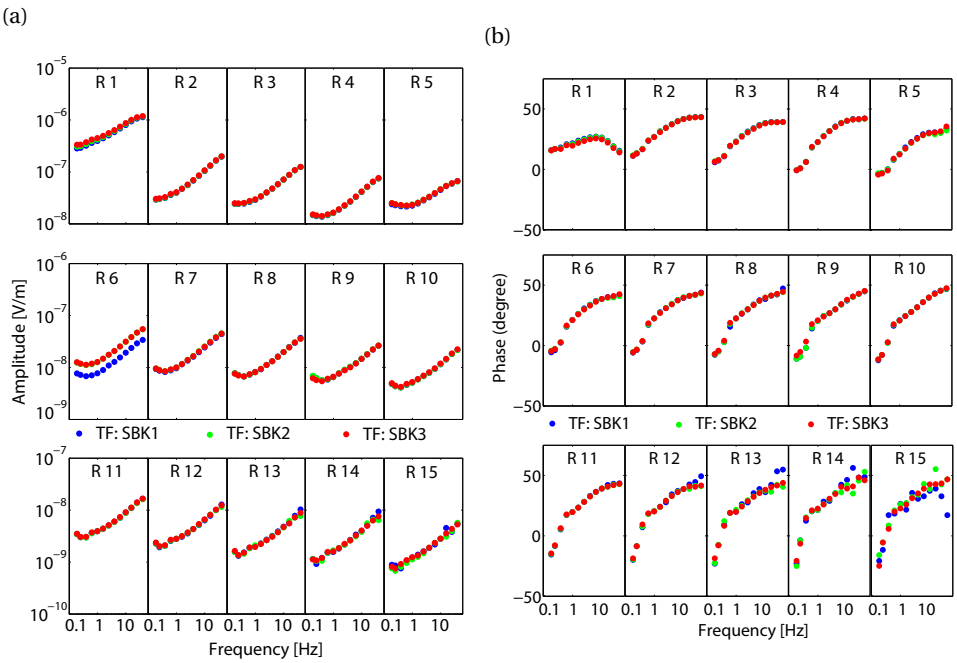

Figure 4.6: TF (a) amplitudes and (b) phases for transmitter 1 and for component $T_{1,2}^{E_x}$ obtained for the first, second and third survey. TF were processed for two source current combinations (I_1, I_3) and (I_2, I_3). Note change in amplitude for R6 (see main text for explanation) and note lower signal-to-noise ratios in phases of R14 and R15.

tion for comparison of the two surveys introduces additional slight differences between the data. The rotation modulates the signal, such that actual source frequencies are $f_0 \pm f_r$, $3f_0 \pm f_r$, etc., with source fundamental frequency f_0 and rotation frequency f_r. We used very small rotation frequencies and considered the frequency modulation to be negligible. Nevertheless, the small differences in source signal between the surveys may have resulted in differences in response functions that could not be eliminated during processing. This was an issue between surveys 1 and 2, while between surveys 2 and 3 we used exactly the same source signals with the same rotation frequencies.

Amplitudes and phases of resulting response functions are shown in Figures 4.6 and 4.7 for the horizontal electric-field components E_x and E_y, respectively. As a measure of repeatability, we used normalized rms differences such as the ones defined in section 4.2. No trend is visible between the receivers indicating that correlated noise sources were successfully removed from the data. The signal-to-noise ratio is low for the receivers furthest away from the transmitter. In addition, a noise source situated between receiver R14 and R15 (pump or pipeline) decreases the signal-to-noise ratio further.

For the sake of completeness, all TF amplitudes and phases for two polarizations are shown in Appendix A for source location T1 and for base frequencies of 1/16 HZ

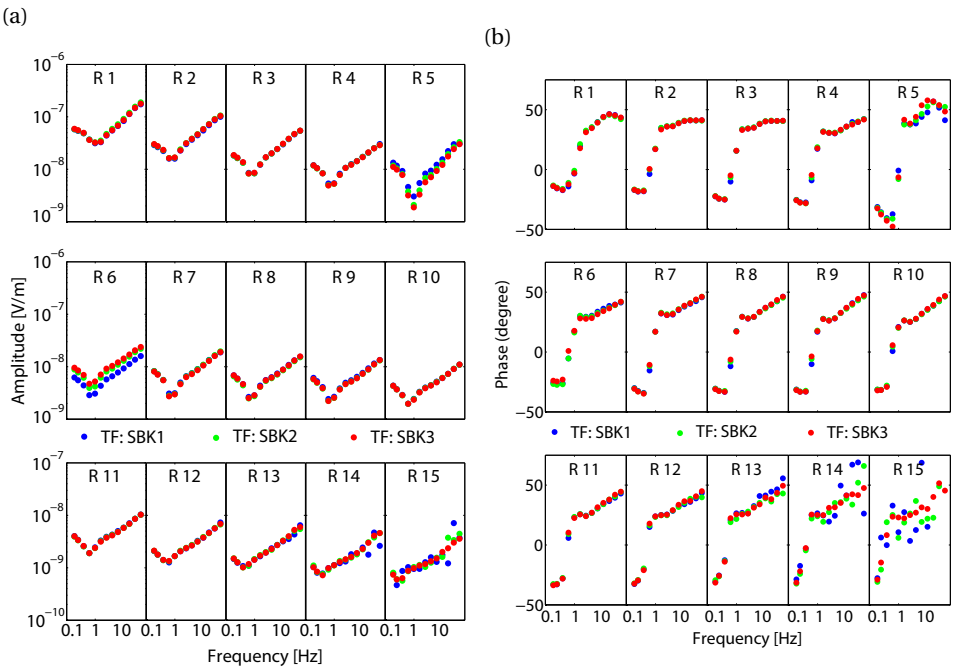

Figure 4.7: TF (a) amplitudes and (b) phases for component $T^{E_y}_{2,3}$ obtained for the first, second and third survey. TF were processed for two source current combinations (I_1, I_2) and (I_1, I_3). Note change in amplitude for R6 (see main text for explanation) and note lower signal-to-noise ratios in phases of R14 and R15.

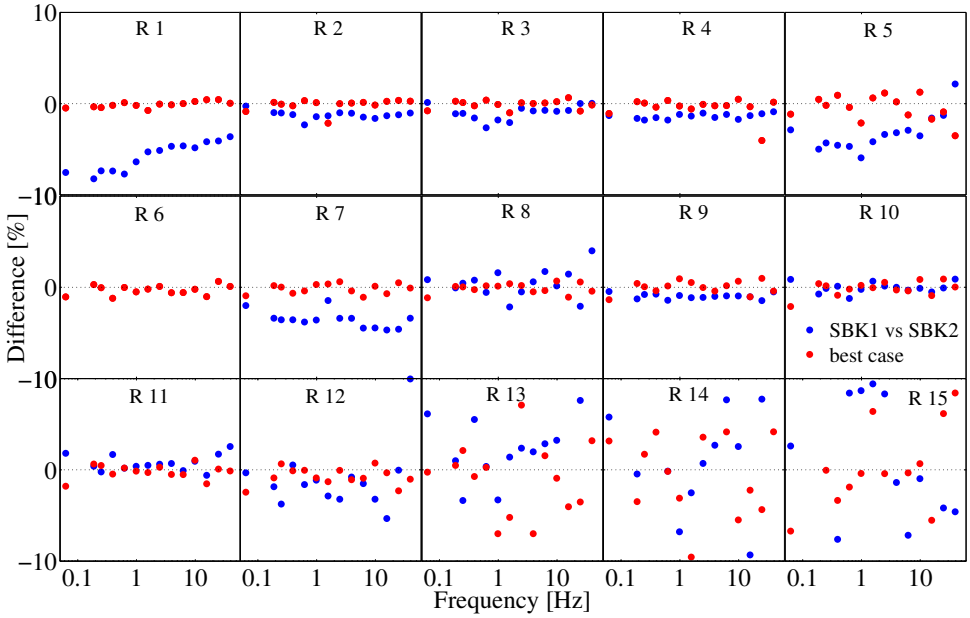

Figure 4.8: Comparison of the differences in amplitude for component $T_{1,2}^{Ex}$ between the first and the second survey for all receiver stations to a best-case scenario for transmitter T1. For the "same-survey variation" case, data from the second survey were equally split into two parts to simulate time-lapse data without actual time-lapse changes in the subsurface. Note that R6 is not included in comparsion of SBK1 versus SBK2.

and 1/4 Hz only, and in Appendix B for source location T3. Uncertainty estimates of the response functions for receivers close to the source are generally smaller than the difference between the response functions between the three surveys. For larger source-receiver offsets, error estimates are larger than the differences between the surveys. The differences between response functions of the three surveys at small source-receiver offsets can be either a consequence of changes in the subsurface such as near-surface time-lapse changes or changes inside the reservoir, or they can be the consequence of limited survey repeatability. Figure 4.8 depicts the differences in amplitude in % between the base and the first repeat survey. For comparison, a "same-survey variation" case is used. To this end, data from the first repeat survey were equally split into "two surveys" with a similar amount of data for the same base frequencies. By looking only at data from one survey (in this case from the repeat survey), we simulate a time-lapse data set with minimized source influence (identical source position), without receiver repositioning errors, and where we can expect more similar background noise. The "same-survey variation" case should ideally only show variations within one survey and thus is treated as a best-case simulation of survey repeatability, assuming that the overall amount of data of each half of the "same-survey variation" case is sufficient. Receivers R4 and R9 show slightly lower differences for the comparison between the two surveys (SBK1 vs. SBK2) than for the "same-survey variation" case, indicating that the influence of changes in acquisition and possible changes of the noise pattern over time are minimal at these receivers. How-

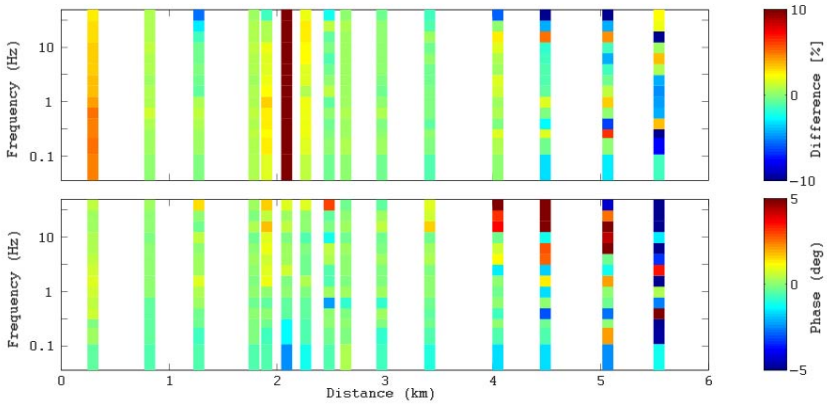

Figure 4.9: Differences in response function amplitude (in %) and phase (in °) between the first and second survey for all receiver stations for transmitter T1. Note high amplitude differences for R6 (see main text for explanation).

ever, changes for R6 are much larger than 10% as a consequence of a slight shift in the receiver position that happens to be close to a metal pipeline structure suggesting that even minor changes in receiver position can have a large impact on the measured amplitudes. For most of the receiver locations, differences are below 2–3% indicating that the repeatability errors with a maximum of 1% relative to the signal at the local receiver chosen by Wirianto et al. (2010) are realistic but too optimistic in a high-noise region. The differences, shown in Figure 4.8, are relatively high when we expect (from early feasibility modeling) changes in the reservoir to have effects on the order of only about 1% on the data, with larger effects only within very limited areas that cannot precisely be predicted. It can be clearly seen that the signal-to-noise ratio is low for the receivers farthest away from the transmitter.

Figure 4.9 shows the differences in the amplitude and phase spectra for the first two surveys for all receivers. A trend between the receivers is not visible. The lack of a pattern between the surveys also suggests that the observed changes may not be related to changes in the reservoir due to steam injection, but may simply be due to uncorrelated local noise sources.

4.4. REPEATABILITY OF INVERSION RESULTS

1D and 3D inversions of the three data sets were done using the above-mentioned forward modeling and inversion algorithms. As input for the inversions, the response functions of both horizontal electric-field components were used. For all inversions, the same receiver positions were used. Including different receiver locations for different surveys would lead to changes in the overall sensitivity and thus influences the region where updates are focused during our inversion. Receivers R1, R5 and R15 were not considered reliable due to bad data quality as a result of strong cultural noise originating

from e.g., pumps, a dairy factory, etc.

4.4.1. REPEATABILITY OF 1D-INVERSION RESULTS

The aims of the 1D inversion are (1) to check the repeatability of the survey and (2) to obtain a good starting model for the 3D inversion. Therefore, single- and multi-receiver 1D inversions were done for all three horizontal electric-field data sets using a simple 1 Ωm half-space as starting model. For the sake of data quality control, we first inverted each receiver separately for the three surveys. The results are shown in Figure 4.10 and in Figure 4.11. For a coarse depth spacing with 83 layers of increasing thickness with depth (Figure 4.10), our inversion approach that favors a smooth and smeared-out model cannot by definition resolve sharp boundaries or thin layers. When using such smooth 1D inversion models as starting points for a 3D inversion, we could not fit the data further and could barely image any 3D subsurface structure (these poor results are not shown in this study). However, for the Schoonebeek field, we know that the actual reservoir thickness is about 15 m and its resistivity determined in well logs varies between several 100 to more than 1000 Ωm. Since the inversion forces the solution to be smooth, the 1D inversion returned a lower resistivity reservoir that is smeared over a large depth range. Since we desire a "blockier" model for the 3D inversion which seems closer to reality, we need to input this as a constraint into the inversion. To produce a 1D inversion model in closer agreement with our a-priori knowledge of the reservoir, we defined a fine layering of 2 m around the reservoir depth (Figure 4.11). This produced 1D models with thin but smooth reservoirs that proved to be well-suited for input into subsequent 3D inversion. We had also tested regularizations without imposing a smoothness constraint around the reservoir depth and hence allowing the model to be "blocky" only at this specific depth. However, the resulting 1D models contained large jumps in conductivity between adjacent layers, causing artifacts and difficulty in further fitting the data in 3D inversion. Both obtained resistivity profiles of Figure 4.11 are similar for most of the receivers and surveys but are not consistent for all receivers. Separate-receiver inversion shows that the depth of reservoir and reservoir resistivity differ for each receiver. As previously mentioned, receiver R6 was slightly shifted to different locations resulting in fairly strong data differences (see Appendix A) and consequently different inversion results. Receiver R9 shows different inversion results for SBK1. This might be the result of external noise sources due to the removal of seismic monitoring equipment in the vicinity of the receiver location, or changes on the nearby production drill pad. It can also be noted that only for the last survey, while production of the Schoonebeek oil field was paused, R14 shows better-quality inversion results with higher resistivity around the reservoir. This is probably due to reduced noise levels when the pumps near this receiver were turned off, and thus data quality was improved.

Multi-receiver 1D inversions were done (1) for all transmitters separately and (2) for transmitters combined. For this study, a simple half-space model with a fixed near-surface was assumed as starting model. Inversion results for the first two surveys are shown in Figure 4.12. The transmitter location 3 is too close to the receiver array and thus lacks sufficient depth penetration for resolving the reservoir at its actual depth. As a direct consequence, the short-offset receivers R9-R15 could not be fitted by a 1D model during the 1D inversion and were neglected. Instead of the reservoir, a shallower artifact

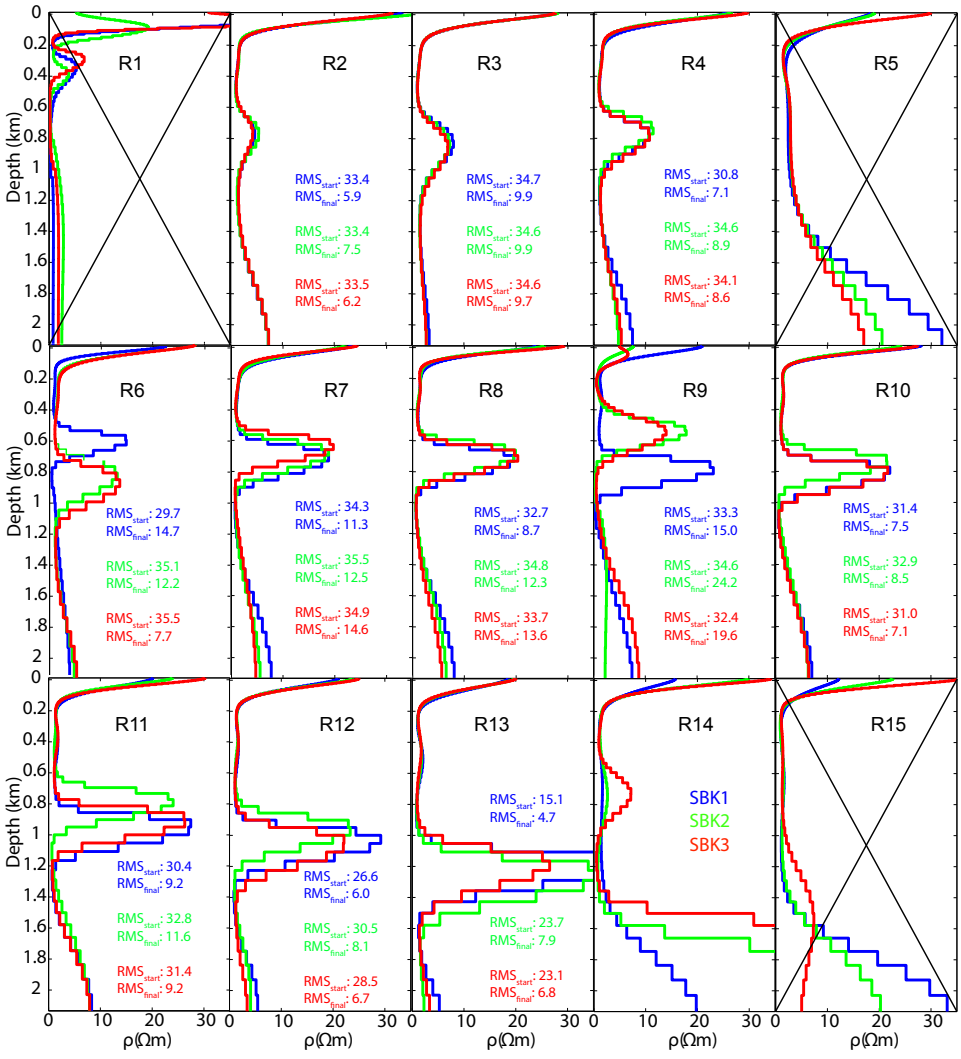

Figure 4.10: 1D subsurface resistivity profile per receiver after separate 1D inversion for each receiver for all three surveys using a coarse depth spacing with 83 layers of increasing thickness with depth and only source signals of period 4 and 16 s. R1, R5 and R15 should not be considered reliable due to bad data quality as a result of strong cultural noise.

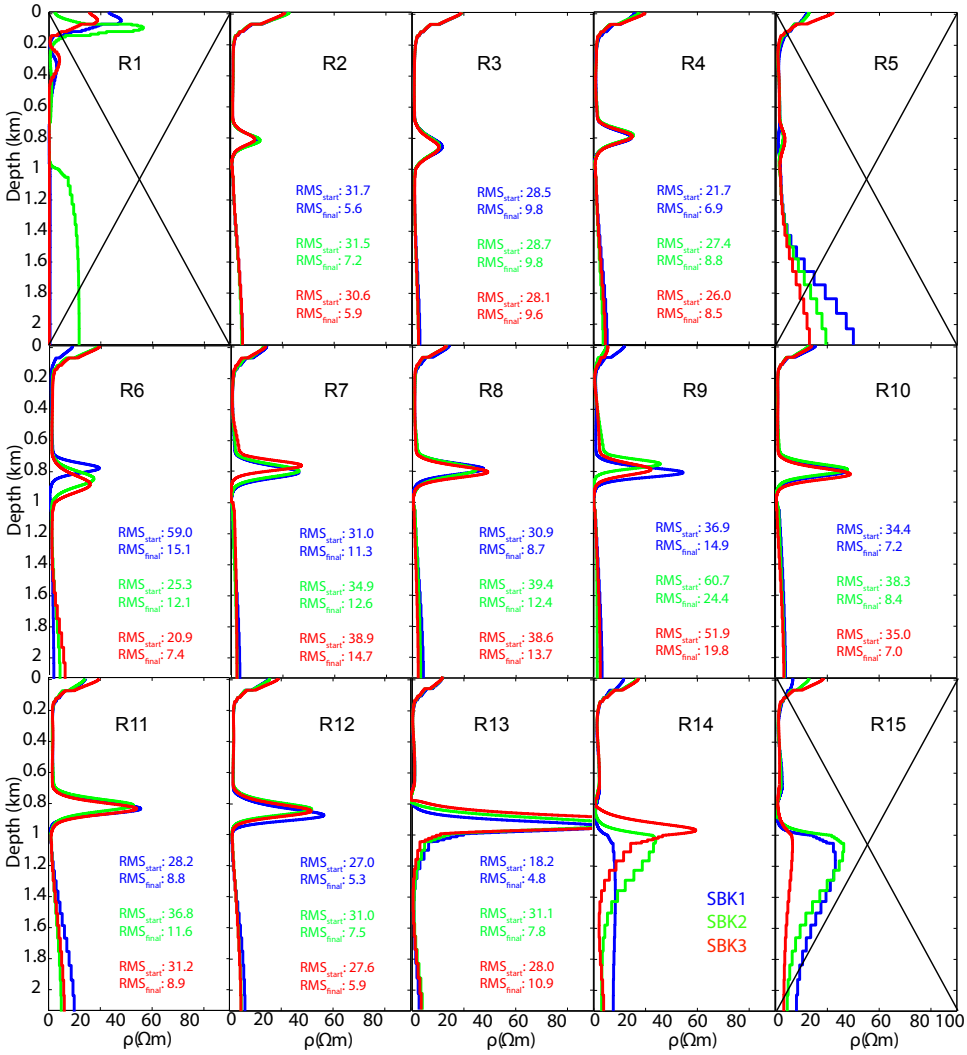

Figure 4.11: 1D subsurface resistivity profile per receiver after separate 1D inversion for each receiver for all three surveys using fine layering of 2 m around reservoir depth and only source signals of period 4 and 16 s. R1, R5 and R15 should not be considered reliable due to bad data quality as a result of strong cultural noise.

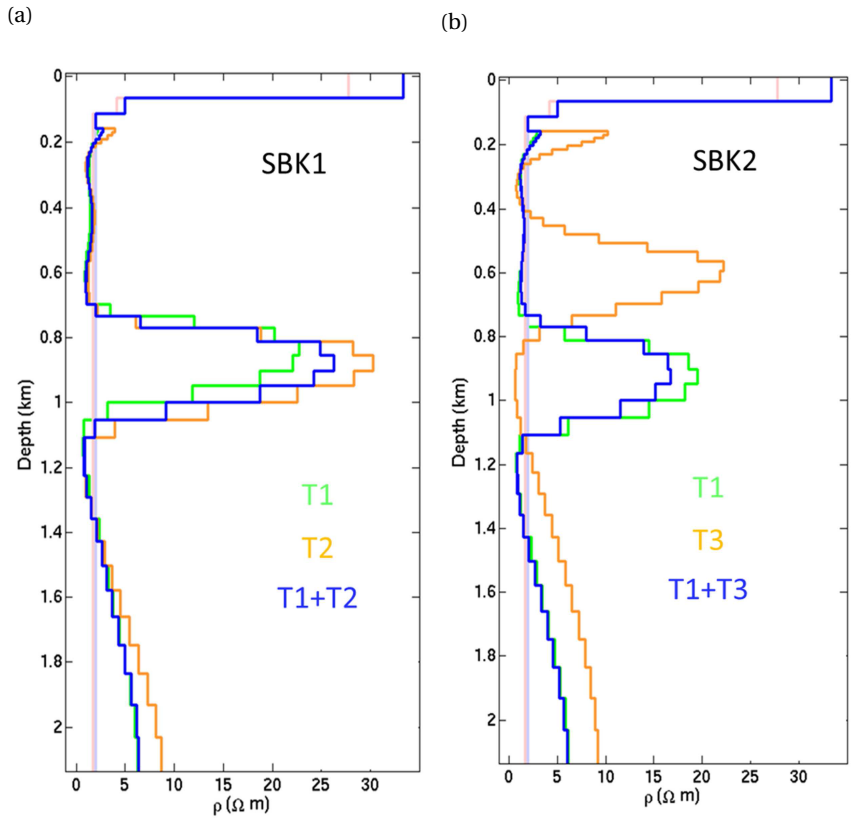

Figure 4.12: Comparison of 1D inversion results for different transmitters (green: only transmitter 1, orange: only transmitter 2 or 3, blue: both transmitters). Left panel shows the base survey (SBK1) and right panel shows the repeat survey (SBK2). The light-colored lines indicate the starting resistivity-depth profile.

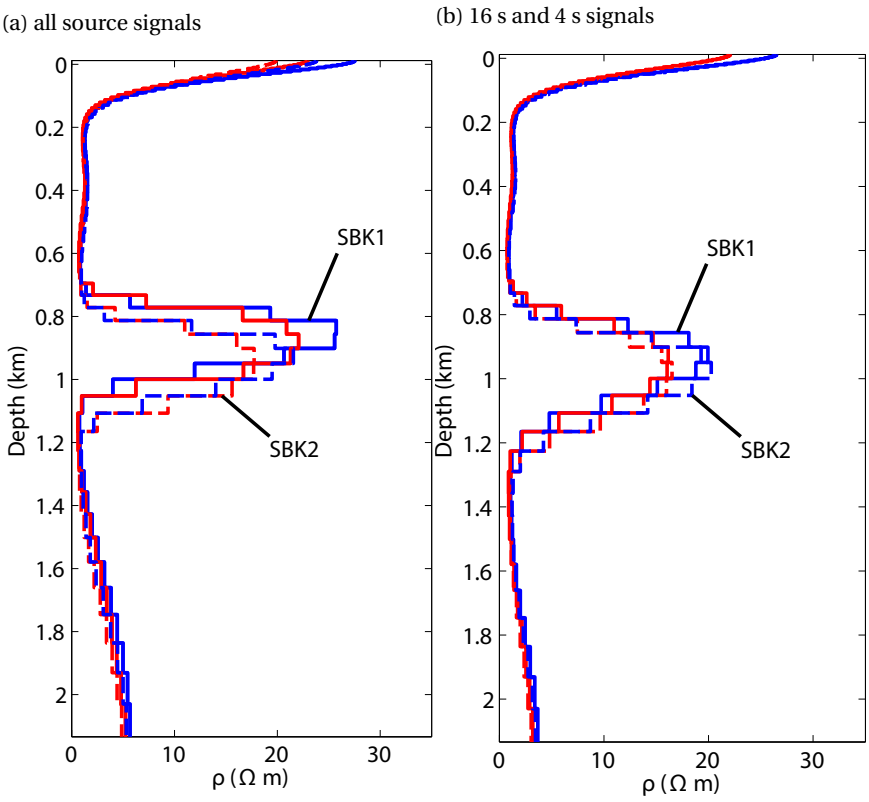

Figure 4.13: Comparison of 1D inversion results between survey 1 and survey 2 for different source signals. (a) all acquired source signals used and (b) only source signals with base frequencies of 1/16 Hz and 1/4 Hz used. Data for transmitter 1 only are shown.

appears when inverting E_x and E_y data from transmitter T3 alone. Therefore, time-lapse data for transmitter T3 are not considered further in the following 1D inversion tests.

The influence of different source base frequencies (discussed above) is shown in Figure 4.13. Figure 4.13a shows inversion results for survey 1 and 2 using all available source signals, whereas Figure 4.13b shows inversion results using only the base frequencies of 1/16 and 1/4 Hz that were available for both surveys. The latter results in more similar response functions and consequently the obtained inversion results are much closer to each other than when using all of the acquired data.

Inversion results for the three surveys and transmitter T1 are shown in Figure 4.14. All receivers were inverted jointly. For Figures 4.14a and 4.14b, the coarse depth spacing with 83 layers of increasing thickness with depth and the fine layering of 2 m around the assumed reservoir depth, were used, respectively. The inversion results show similar 1D subsurface resistivity profiles, with similar reservoir resistivities and depths: for the 1st survey, the maximum resistivity is smallest; for the 2nd survey, the maximum is larger

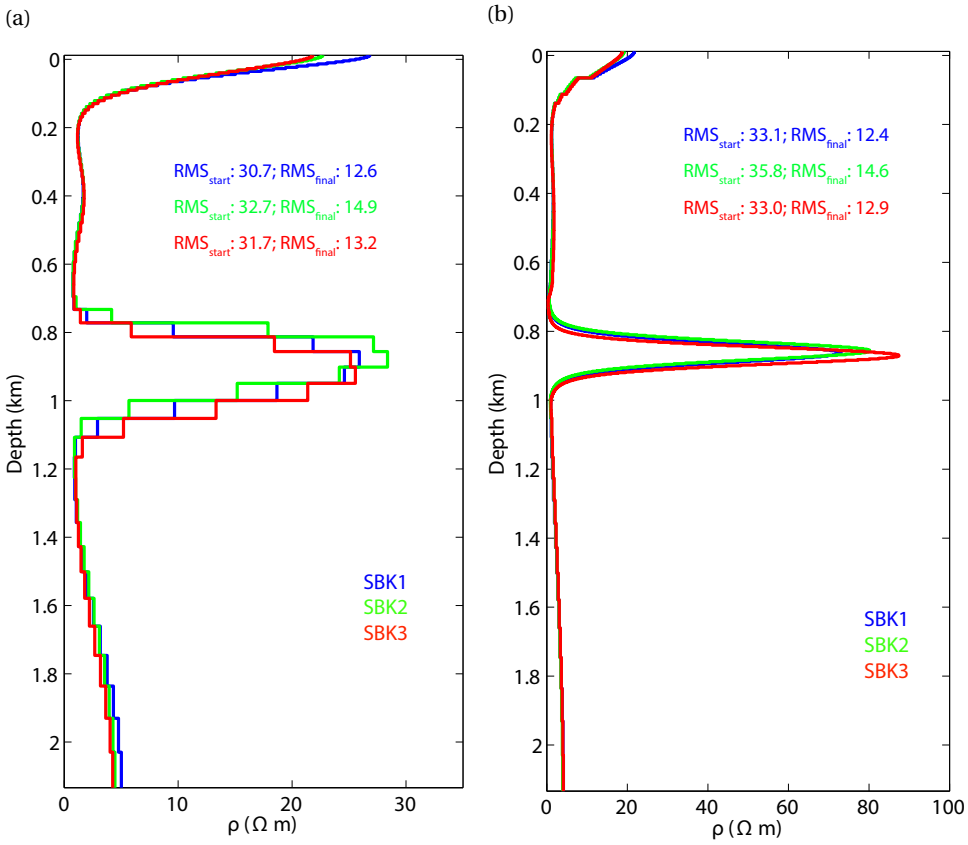

Figure 4.14: 1D subsurface resistivity profile after 1D inversion for all three surveys using (a) a coarse depth spacing with 83 layers of increasing thickness with depth, (b)) fine layering of 2 m around reservoir depth. For (a) a simple 1 Ωm halfspace model was used and for (b) a 3 Ωm halfspace model with additional near-surface structure was used. Receivers are inverted jointly for transmitter location 1 and only source signals of period 4 and 16 s.

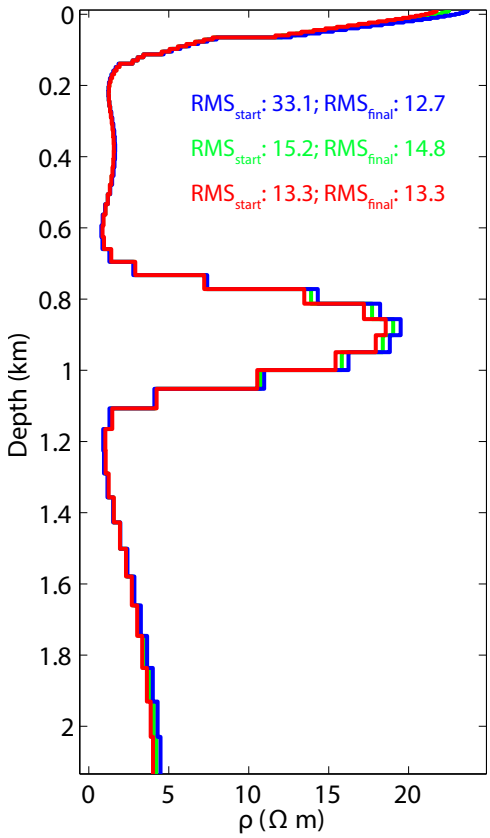

Figure 4.15: 1D subsurface resistivity profile after 1D inversion for all three surveys using a coarse depth spacing with 83 layers of increasing thickness with depth and only source signals of period 4 and 16 s. Previous inversion results were used as starting model input for next inversion.

and a bit shallower and for the 3rd survey, it's yet a bit larger and a bit deeper. A clear robust trend that could be related to changes in the reservoir is not observable, thus supporting our conjecture that changes due to the steam injection are indeed too small to be recognizable. Note that even if changes in the reservoir were large enough to be detectable, we would not necessarily expect to see them in 1D inversions.

For time-lapse inversions, the inversion result for the base survey (SBK1) was used as the starting model for the first repeat survey (SBK2) and the inversion result after the first repeat survey was used as the starting model for the second repeat survey (SBK3) (Figure 4.15). Since the three data sets are very similar and the inversion seeks to generate the smoothest possible model by applying a minimum-norm solution, the inversion has difficulties in updating the previous inversion result and consequently terminates after less than 5 iterations. Figure 4.15 shows minor updates that are limited to small changes in resistivity in the reservoir and the near subsurface. Strong caution must be taken not to over-interpret 1D inversion results since changes inside the reservoir due

to steam injection are expected to be complex in 3D and to be practically invisible in 1D models.

From the 1D-inversion tests done, we can conclude that the inversion results from each separate survey are repeatable provided that differences within 2-3% are acceptable. The inversion results for all surveys, even when starting from a simple homogeneous half-space, are similar. Their starting and final rms values are within ±2 for most of the receivers. Variations in the results may be due to different noise patterns, differences in the acquisition setup and are less likely due to changes inside the reservoir as a consequence of steam injection.

4.4.2. REPEATABILITY OF 3D-INVERSION RESULTS

The 3D inversions were done for two different starting models but exactly the same starting model was used to invert data from surveys 1, 2 and 3: (1) a simple 1D model derived from the 1D inversion results of Figure 3.19a and (2) a more complex 3D model obtained by combining internally available reservoir depth information (see Figure 3.21a) with our previously obtained 1D inversion results. This starting model was obtained by extracting the reservoir topography underneath the receiver line from the horizon shown in Figure 3.16. At depths below 400 m, resistivities are defined by shifting the 1D resistivity column vertically such that the resistivity maximum coincides with the depth of the picked horizon. In contrast to 1D inversions, choosing a structurally well-defined starting model is required in 3D, most likely because of the very small data set and huge number of model parameters that makes the problem highly under-determined. If we used a simple homogeneous half-space model, we would not detect the reservoir.

Figure 4.16 shows the resistivities found by the 3D inversion using the 1D starting model. Resistivities were extracted along the structure, at the depths where starting resistivity is maximal. The pattern of high and low resistivity with respect to the background 1D model is similar for all three surveys. However, data from survey 3 show the smallest variations and data from survey 1 the largest. This is in accordance with the amplitudes of the corresponding error estimates of the response functions. Comparing the obtained resistivity at $x = 4 - 6$ km of about $600 - 1000$ Ωm to resistivities estimated from reservoir simulation data and petrophysical relations (Streich, 2016) shows that predicted resistivities are of the same order of magnitude.

For the 3D starting model, the results displayed in Figure 4.17 are obtained. 3D inversion updates are limited to a narrower corridor around the receiver array than when using the 1D starting model. The area where no reservoir depth information was available is left blank (in these regions, 1D lateral extrapolation of the starting model was done, thus starting model and inversion results cannot be considered to be reliable). Maximum resistivities are higher compared to those found when using the 1D starting model (Figure 4.16) and are more focused on the area around receiver R1-R4. Highest resistivities are now found in survey 3.

Figure 4.18 shows depth sections for the 3D inversion results using the 3D starting model. Resistivity models and corresponding resistivity updates are shown for each survey. Resistivity updates done by the 3D inversion are most prominent at the reservoir flanks (mostly at the western flank since this flank is better illuminated by transmitter 1 than the eastern one) and are strongest for the third survey.

(a)

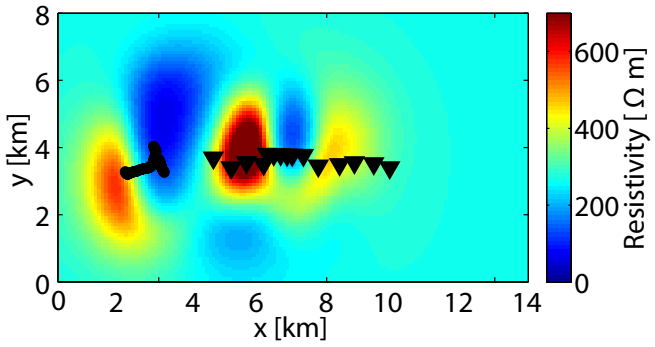

(b)

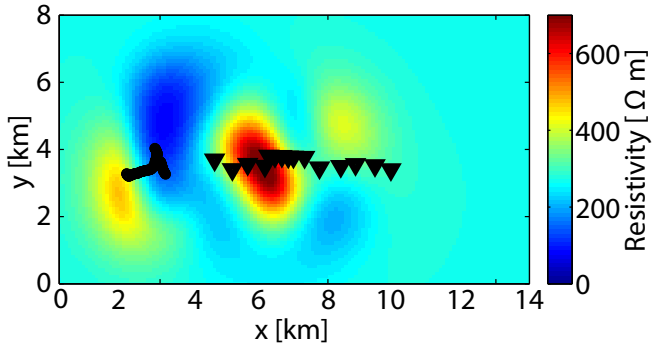

(c)

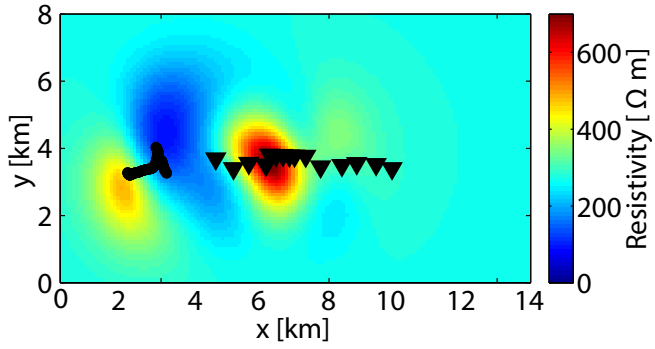

Figure 4.16: Resistivity found by 3D inversion from 1D starting model, extracted at the depths where starting resistivity is maximal for (a) survey 1, (b) 1^{st} repeat survey and (c) 2^{nd} repeat survey. Black lines/triangles indicate source/receiver locations.

(a)

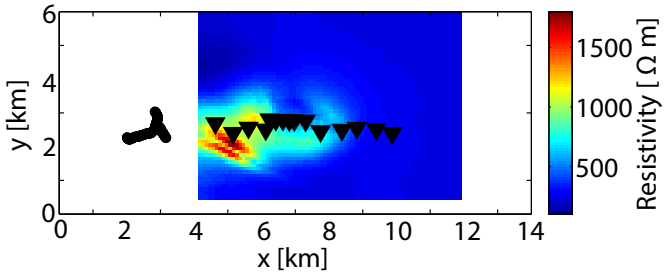

(b)

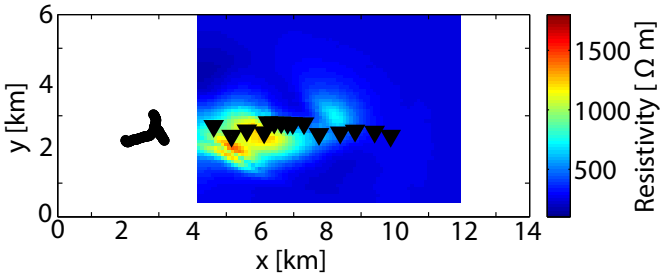

(c)

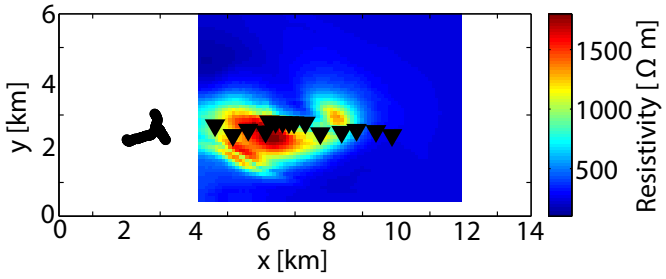

Figure 4.17: Resistivity found by 3D inversion from 3D starting model, extracted at the depths where starting resistivity is maximal for (a) survey 1, (b) 1^{st} repeat survey and (c) 2^{nd} repeat survey. Black lines/triangles indicate source/receiver locations.

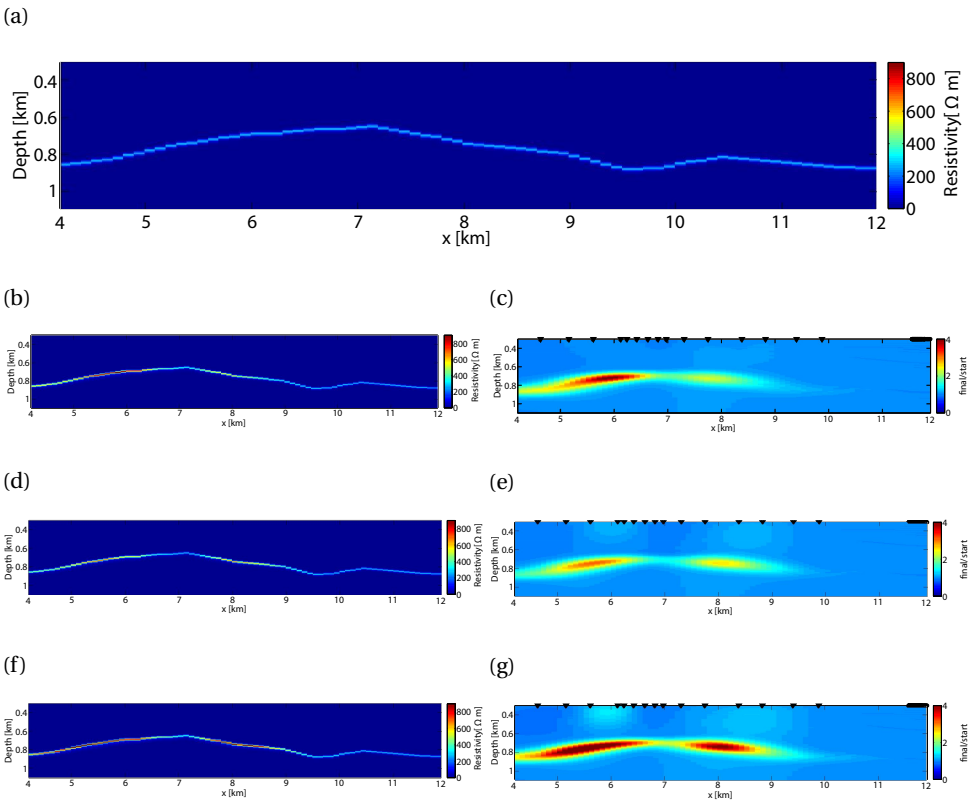

Figure 4.18: Vertical sections at y = 3 km. (a) 3D starting model derived from 1D inversion and reservoir depth information; (b), (d) and (f) resistivity models after inversion of E_x and E_y data for SBK1, SBK2 and SBK3, respectively. Corresponding resistivity updates relative to starting model are shown in (c), (e) and (g). The data fits f for each survey are: f_{start}: 35.9/f_{final}: 3.8 (SBK1); f_{start}: 57.0/f_{final}: 6.0 (SBK2) and f_{start}: 35.3/f_{final}: 3.5 (SBK3)

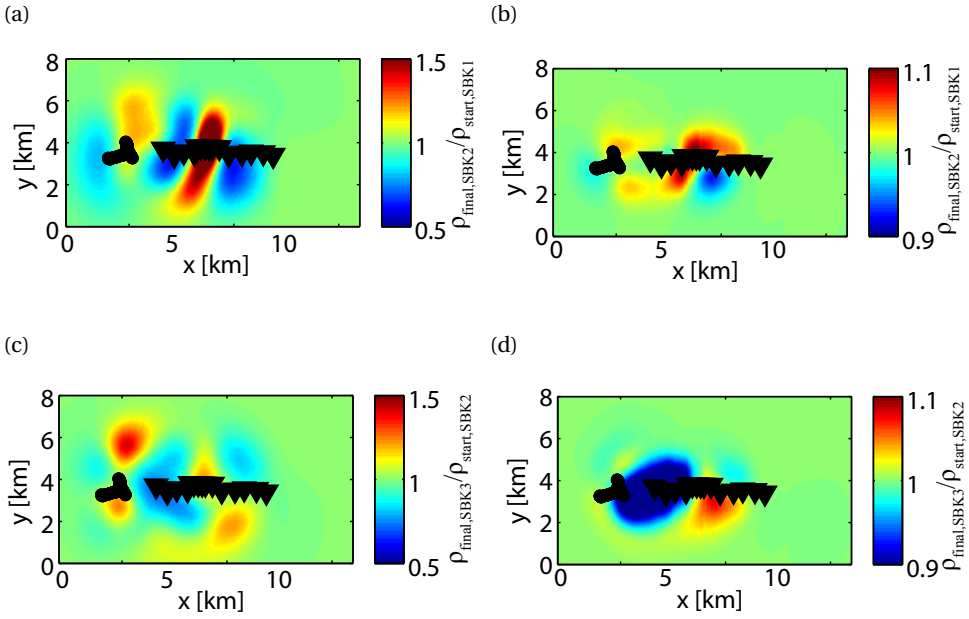

Figure 4.19: Resistivity updates done by 3D inversion from (a), (c) 1D starting model and (b), (d) 3D starting model extracted at the depths where starting resistivity is maximal. (a), (b) Inversion result from the first survey was used as starting model and data from the second survey were inverted; (c), (d) Inversion result from the second survey was used as starting model and data from the third survey were inverted. Black lines/triangles indicate source/receiver locations. The data fits f are: (a) f_{start}: 20.9/f_{final}: 9.0; (b) f_{start}: 18.5/f_{final}: 8.0;(c) f_{start}: 9.2/f_{final}: 4.5 and (d) f_{start}: 8.9/f_{final}: 4.4. Note that the color scale for (a) and (c) differs from the color scale for (b) and (d).

To consider time-lapse inversions, the inversion result for the base survey (SBK1) was used as the starting model for the repeat survey (SBK2), and the inversion result after the first repeat survey was used as the starting model for the second repeat survey (SBK3). The resistivity updates are shown in Figure 4.19. Figure 4.19a shows the changes between survey 2 and survey 1 using a 1D starting model and Figure 4.19c the changes between survey 3 and survey 2 using the starting model from the previous inversion. Apart from a decrease in resistivity between R1 – R3 for both time-lapse examples, changes between the two inversions are different. Figures 4.19b and 4.19d show corresponding inversion results for a 3D starting model. Resistivity updates between the surveys again differ from each other. Results from using the 3D starting model can be considered to be somewhat more reliable than those obtained using the 1D starting model. Final data fits from 3D starting model are better than final data fits when using a 1D starting model (see also Chapter 3). Nevertheless, we do not observe a clear trend of resistivity variation that can be related to the oil production during the time period between the surveys. The variations between the surveys are likely due to different noise patterns during the surveys. However, the exact origin of the variations cannot be explained without additional knowledge of all the noise sources.

4.4.3. CHALLENGES AND DISCUSSION

Receiver and source locations are dismantled after each survey. To allow for proper time-lapse measurements, source and receiver positions must be rebuilt at the same positions and thus measured accurately. The influence of slight differences in the survey layout on the data was found to be larger than initially expected with much larger than 10% (e.g., see receiver R6 in Figures 4.10 and 4.11). The inaccuracies may lead to EM field changes at receiver stations that are a multiple of the expected changes due to resistivity changes at the reservoir; in that case, even changes at reservoir level much larger than expected will be masked completely (e.g., receiver R6). We conclude that accurate measurements of the positions of every receiver electrode, and not only receiver midpoints, are needed to minimize receiver positioning errors to far less than 1 m. This is particularly the case in high-noise regions such as a producing oil field, where metallic objects as pipelines and borehole casings interfere with the measurements. Unfortunately, individual electrode locations were not measured during surveys 1 and 2. For these surveys, the nominal midpoints of the receiver electrodes remained stationary (repeatedly surveyed with differential GPS that proved to be more accurate than determining electrode locations along the N-S and W-E directions using a compass), but the distances between the midpoints and each individual electrode differed slightly. We estimate this may have resulted in lateral shifts of electrode dipoles by up to 3 m. For improvement of repeatability, we used the same electrode dipole lengths for the third survey as were used for the first survey in order to reduce the lateral shifts of electrode dipoles between these two surveys.

As mentioned above, on the source side, it is important to repeat source electrodes and cables. Further, the emitted signal between the surveys should be of identical base and rotation frequency in order to avoid interpolation errors in the data during data processing.

4.5. CONCLUSIONS

Subtle resistivity changes inside a reservoir are only recognizable in highly repeatable time-lapse CSEM data and thus efforts in minimizing the errors due to inaccurate surface geometry and noise sources were taken. We estimate that the resistivity changes inside the reservoir during the short time period of less than two years between the three acquired surveys were minor and relative changes between the data no more than ~1%, and thus too low to be detectable. Therefore, this study focused on the issue of repeatability to assure high-quality data sets for future monitoring applications. To enhance data quality and subsequently decrease repeatability errors, more attention needs to be focused on accurate source and receiver positions. Procedures that are used for one-time CSEM surveys such as measuring receiver midpoints and dipole length only, have to be adjusted to achieve the necessary repeatability. Measuring each receiver electrode location by differential GPS and GPS-tracking of the source cables should be done for each survey to minimize discrepancies between the survey layouts. Imprecise layout together with technical challenges such as high-cultural EM noise, near-surface heterogeneities and metallic objects near the measurement equipment showed that slight changes in receiver location of 1-5 m may lead to relative changes between the different data set a multiple larger than changes of interest (>10%), i.e. due to steam injection. Further, source signals should have the same source base frequency for all surveys in order to avoid inaccuracies in response function calculation. Small-scale resistivity changes that are estimated from reservoir simulation data and petrophysical relations cannot be resolved by the CSEM method with the used survey geometry. However, the general behavior of the resistivity variations is possible to detect.

All in all, repeatability errors between the data found in this study were below 2–3% apart from the large-offset data. A best-case simulation shows similar differences in response-function amplitudes, which suggests that source influence and changes in noise patterns over a one-year period have a rather small influence on repeatability. No space/frequency trends in amplitude and phase were observed in the time-lapse differences of the horizontal-field response functions. Signal-to-noise ratios at long offsets can, in principle, be improved by longer recordings and/or stronger source currents (the latter is not possible with the source used). Data quality during the three surveys slightly increased likely as a result of different source signal periods and transmission times and, especially, the stop of steam injection and oil production before the beginning of the third survey leading to less man-made EM-noise. Separate 1D inversions for the three surveys show a good match of inversion models, with starting and final rms values within ±2, whereas resistivity updates as a result of 3D inversions show no clear pattern between the three surveys. Time-lapse inversions (using previous survey inversion result as starting model) show only small inversion updates indicating that the three data sets are similar. With high-accuracy and high-quality measurements using the suggested improvements, repeatability errors might be lowered by another ~1%, thus clearly stating that land CSEM reservoir monitoring has a potential to add additional information to long-term reservoir monitoring where changes in the reservoir are assumed to be larger than the changes that were expected in this study.

APPENDICES

A. RESPONSE FUNCTION AMPLITUDES AND PHASES FOR HORIZONTAL ELECTRIC FIELDS FOR SOURCE T1

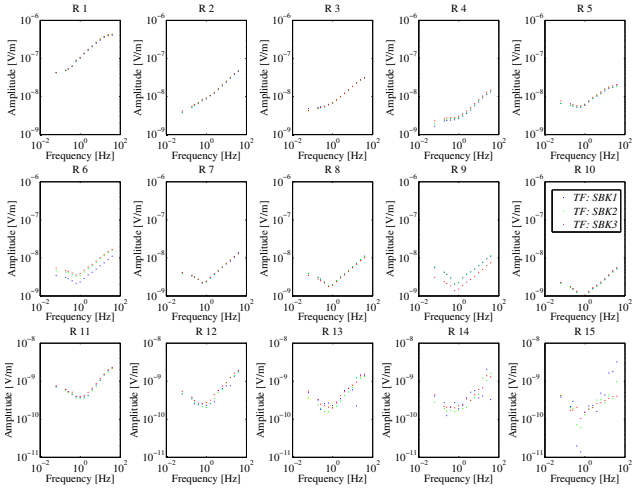

Figure 4.20: Amplitudes of response functions of all surface receivers after notch filtering for component $T_{2,3}^{E_x}$ obtained for first (blue dots), second (green dots) and third (red dots) survey for transmitter location T1 (base frequencies of 16 s and 4 s only).

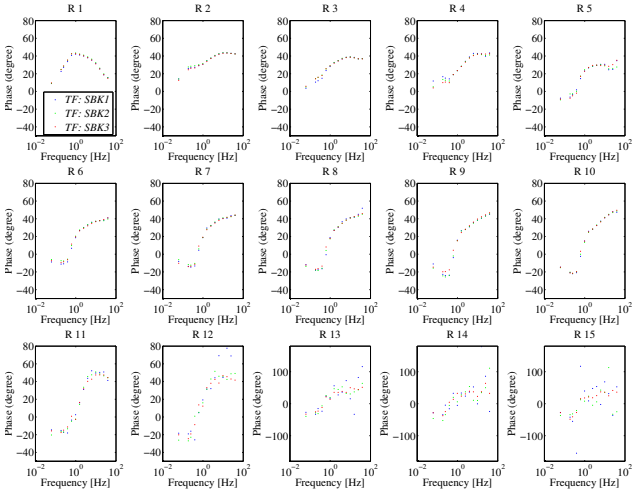

Figure 4.21: Phase of response functions of all surface receivers after notch filtering for component $T_{2,3}^{E_x}$ obtained for first (blue dots), second (green dots) and third (red dots) survey for transmitter location T1 (base frequencies of 16 s and 4 s only).

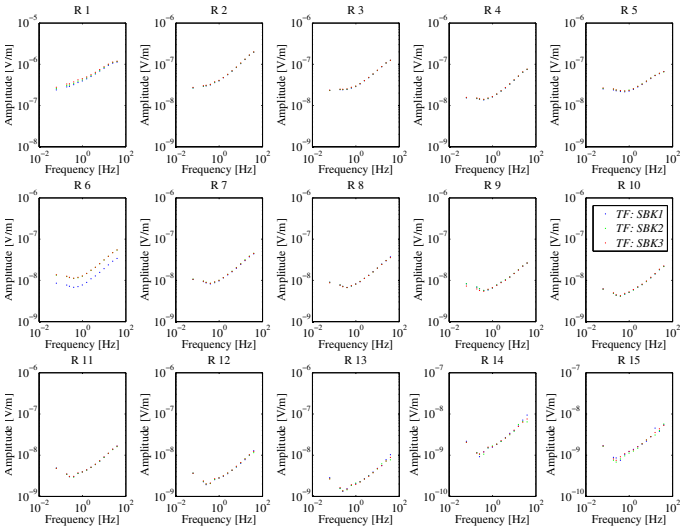

Figure 4.22: Amplitudes of response functions of all surface receivers after notch filtering for component $T_{1,2}^{E_x}$ obtained for first (blue dots), second (green dots) and third (red dots) survey for transmitter location T1 (base frequencies of 16 s and 4 s only).

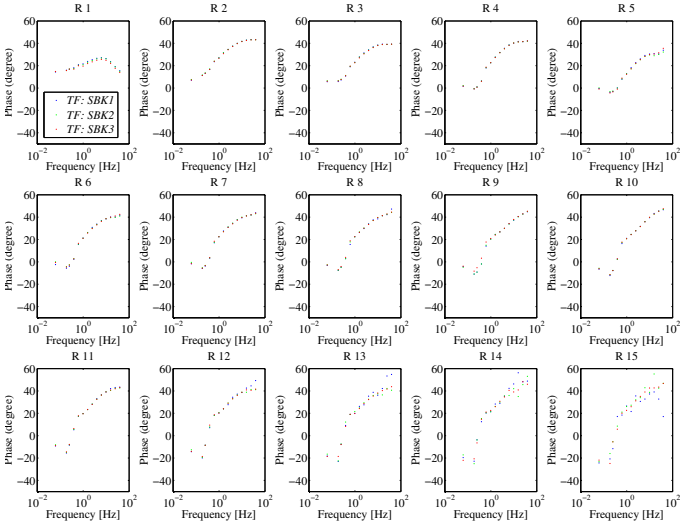

Figure 4.23: Phase of response functions of all surface receivers after notch filtering for component $T_{1,2}^{E_x}$ obtained for first (blue dots), second (green dots) and third (red dots) survey for transmitter location T1 (base frequencies of 16 s and 4 s only).

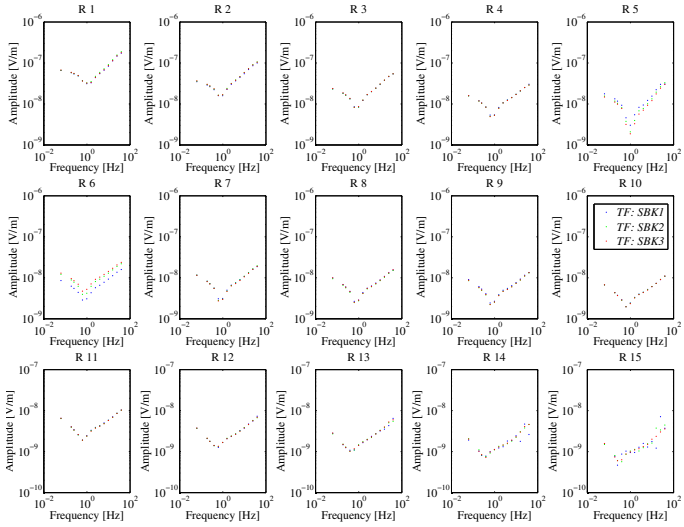

Figure 4.24: Amplitudes of response functions of all surface receivers after notch filtering for component $T_{2,3}^{E_y}$ obtained for first (blue dots), second (green dots) and third (red dots) survey for transmitter location T1 (base frequencies of 16 s and 4 s only).

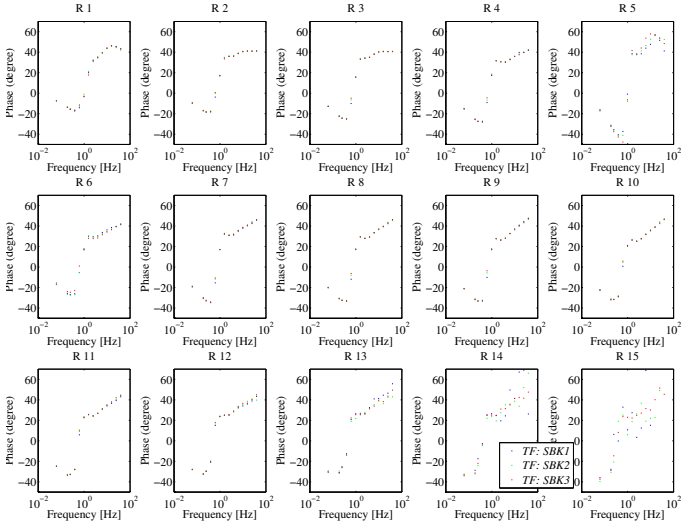

Figure 4.25: Phase of response functions of all surface receivers after notch filtering for component $T_{2,3}^{E_y}$ obtained for first (blue dots), second (green dots) and third (red dots) survey for transmitter location T1 (base frequencies of 16 s and 4 s only).

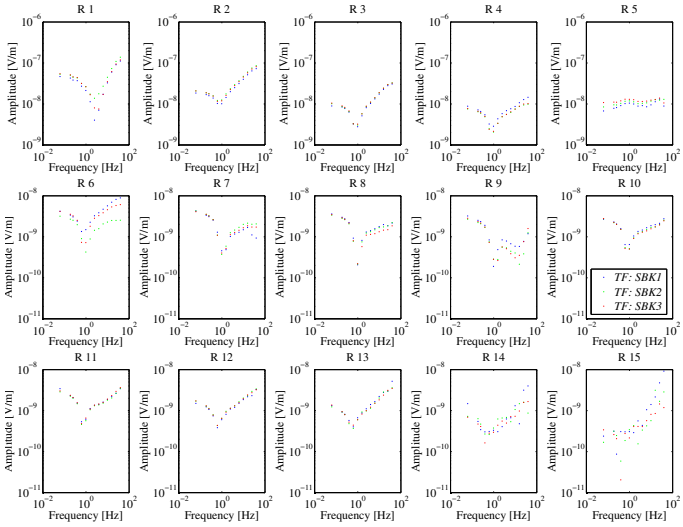

Figure 4.26: Amplitudes of response functions of all surface receivers after notch filtering for component $T_{1,2}^{E_y}$ obtained for first (blue dots), second (green dots) and third (red dots) survey for transmitter location T1 (base frequencies of 16 s and 4 s only).

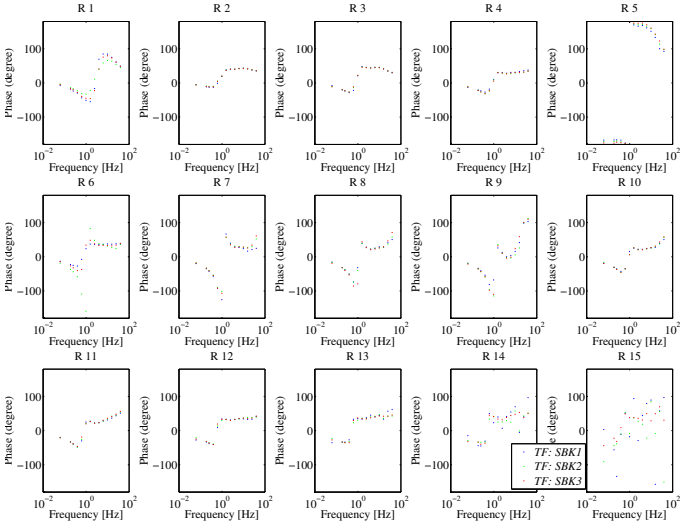

Figure 4.27: Phase of response functions of all surface receivers after notch filtering for component $T_{1,2}^{E_y}$ obtained for first (blue dots), second (green dots) and third (red dots) survey for transmitter location T1 (base frequencies of 16 s and 4 s only).

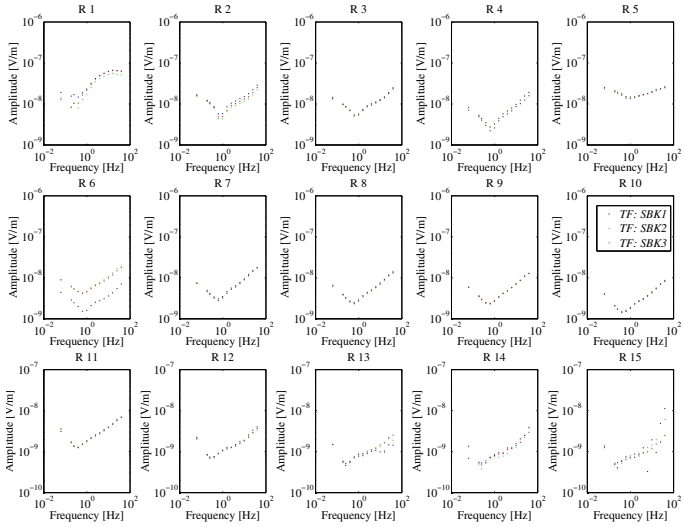

Figure 4.28: Amplitudes of response functions of all surface receivers after notch filtering for component $T_{1,3}^{E_y}$ obtained for first (blue dots), second (green dots) and third (red dots) survey for transmitter location T1 (base frequencies of 16 s and 4 s only).

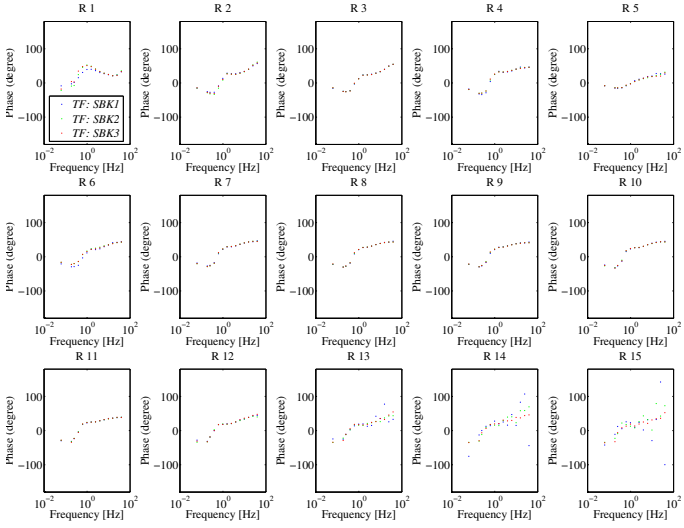

Figure 4.29: Phase of response functions of all surface receivers after notch filtering for component $T_{1,3}^{E_y}$ obtained for first (blue dots), second (green dots) and third (red dots) survey for transmitter location T1 (base frequencies of 16 s and 4 s only).

B. RESPONSE FUNCTION AMPLITUDES AND PHASES FOR HORIZONTAL ELECTRIC FIELDS FOR SOURCE T3

Note: TF amplitudes and phases for R13, R14 and R15 are not trustworthy since these receivers are too close to the source and their data were partly clipped. For some polarizations of R10–R12 TF's also differ strongly from survey to survey – causes for this are not yet known.

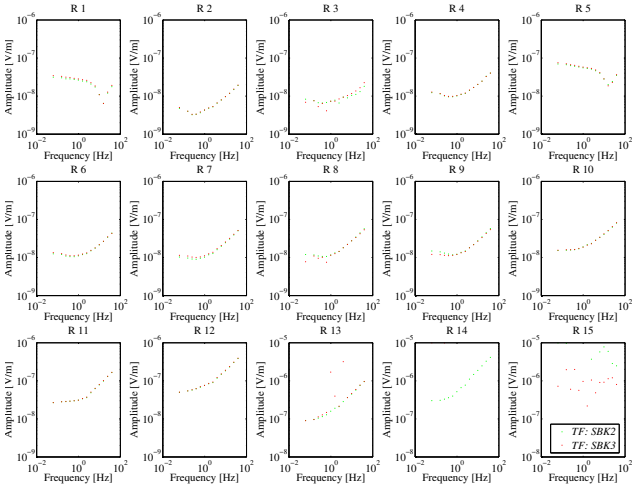

Figure 4.30: Amplitudes of response functions of all surface receivers after notch filtering for component $T_{2,3}^{E_x}$ obtained for second (green dots) and third (red dots) survey for transmitter location 3.

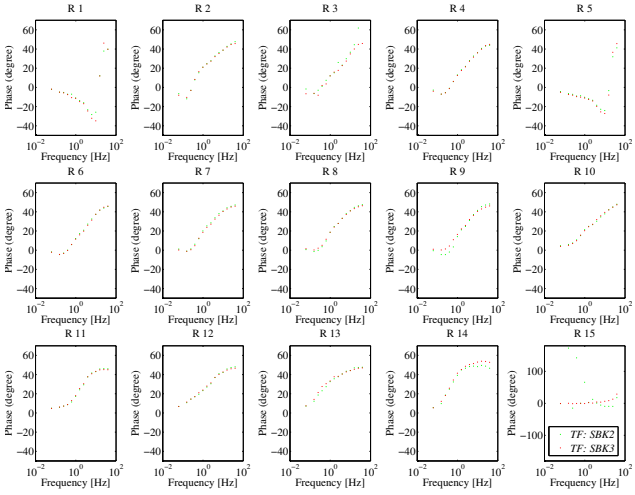

Figure 4.31: Phase of response functions of all surface receivers after notch filtering for component $T_{2,3}^{E_x}$ obtained for second (green dots) and third (red dots) survey for transmitter location 3.

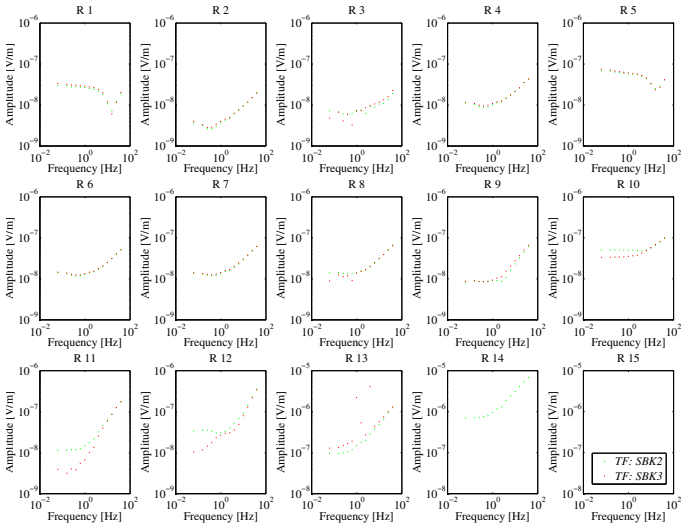

Figure 4.32: Amplitudes of response functions of all surface receivers after notch filtering for component $T_{1,2}^{E_x}$ obtained for second (green dots) and third (red dots) survey for transmitter location 3. Note: Changes in R11 and R12 need further investigation.

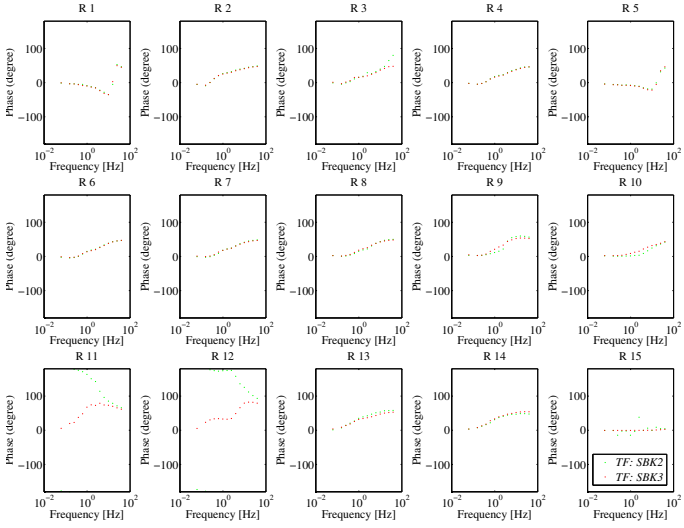

Figure 4.33: Phase of response functions of all surface receivers after notch filtering for component $T_{1,2}^{E_x}$ obtained for second (green dots) and third (red dots) survey for transmitter location 3.

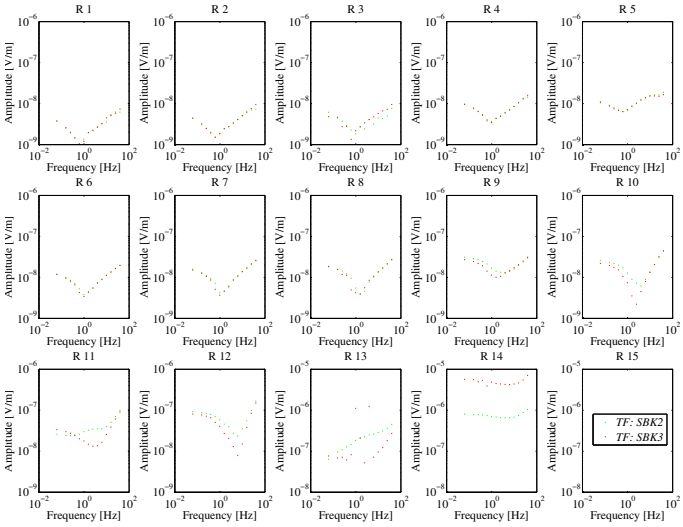

Figure 4.34: Amplitudes of response functions of all surface receivers after notch filtering for component $T_{2,3}^{Ey}$ obtained for second (green dots) and third (red dots) survey for transmitter location 3.

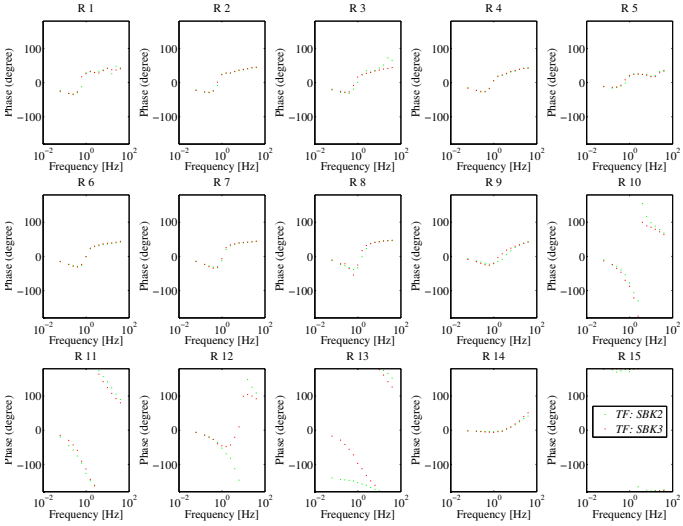

Figure 4.35: Phase of response functions of all surface receivers after notch filtering for component $T_{2,3}^{Ey}$ obtained for second (green dots) and third (red dots) survey for transmitter location 3.

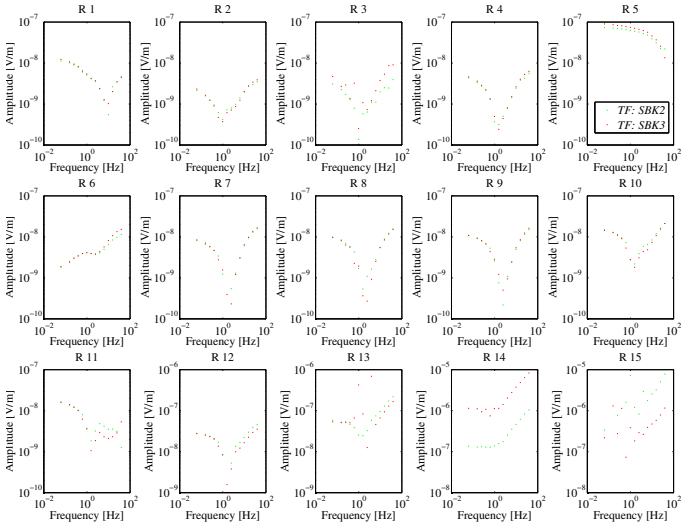

Figure 4.36: Amplitudes of response functions of all surface receivers after notch filtering for component $T_{1,3}^{E_y}$ obtained for second (green dots) and third (red dots) survey for transmitter location 3.

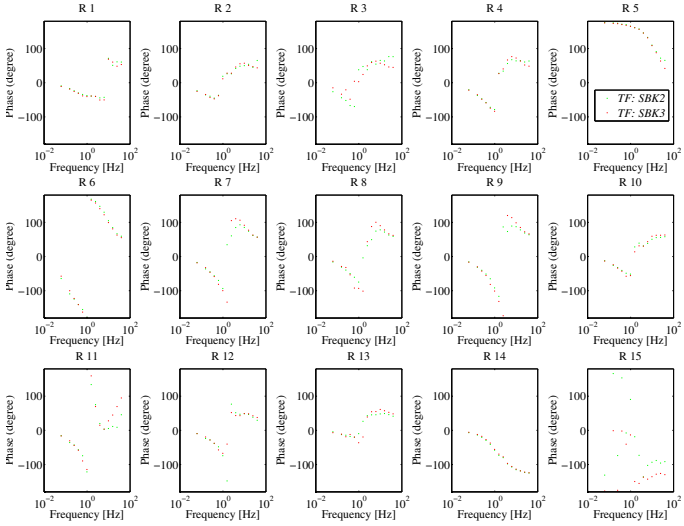

Figure 4.37: Phase of response functions of all surface receivers after notch filtering for component $T_{1,3}^{E_y}$ obtained for second (green dots) and third (red dots) survey for transmitter location 3.

REFERENCES

Abubakar, A., G. Gao, T. M. Habashy, and J. Liu, 2012, Joint inversion approaches for geophysical electromagnetic and elastic full-waveform data: Inverse Problems, **28**.

Aminzadeh, F., J. Brac, and T. Kuns, 1997, 3-D salt and overthrust models: SEG/EAGE.

Batzle, M., and Z. Wang, 1992, Seismic properties of pore fluids: GEOPHYSICS, **57**, 1396–1408.

Brown, V., G. M. Hoversten, and K. Key, 2012, Seismically regularized controlled-source electromagnetic inversion: Geophysics, **77(1)**, E57–E65.

Colombo, D., and G. McNeice, 2013, Quantifying surface-to-reservoir electromagnetics for waterflood monitoring in a Saudi Arabian carbonate reservoir: Geophysics, **78**, E281–E297.

Constable, S., 2010, Ten years of marine CSEM for hydrocarbon exploration: Geophysics, **75**, 75A67–75A81.

Den Boer, E., J. Eikelboom, P. Van Driel, and D. Watts, 2000, Resistivity imaging of shallow salt with magnetotellurics as an aid to prestack depth migration: First Break, **18**, 19–26.

Girard, J. F., N. Coppo, J. Rohmer, B. Bourgeois, V. Naudet, and C. Schmidt-Hattenberger, 2011, Time-lapse CSEM monitoring of the Ketzin (Germany) CO2 injection using 2xMAM configuration: Energy Procedia, 3322–3329.

Haber, E., and D. Oldenburg, 1997, Joint inversion: A structural approach: Inverse Problems, **13**, 63–77.

Hunziker, J., J. Thorbecke, and E. Slob, 2015, The electromagnetic response in a layered vertical transverse isotropic medium: A new look at an old problem: GEOPHYSICS, **80**, F1–F18.

Liang, L., A. Abubakar, and T. M. Habashy, 2012, Joint inversion of controlled-source electromagnetic and production data for reservoir monitoring: Geophysics, **77**.

Lien, M., and T. Mannseth, 2008, Sensitivity study of marine CSEM data for reservoir production monitoring: Geophysics, **73**, F151–F163.

MacGregor, L., S. Bouchrara, J. Tomlinson, U. Strecker, J. Fan, X. Ran, and G. Yu, 2012, Integrated analysis of CSEM, seismic and well log data for prospect appraisal: A case study from West Africa: First Break, **30**, 77–82.

Michou, L., T. Coléou, and Y. Lafet, 2013, 4D Seismic inversion on continuous land seismic reservoir monitoring of thermal EOR: 75^{th} EAGE Conference & Exhibition. (Extended Abstract).

Mulder, W., 2006, A multigrid solver for 3D electromagnetic diffusion: Geophysical Prospecting, **54**, 633–649.

Orange, A., K. Key, and S. Constable, 2009, The feasibility of reservoir monitoring using time-lapse marine CSEM: Geophysics, **74**, F21–F29.

Plessix, R. E., M. Darnet, and W. A. Mulder, 2007, An approach for 3D multisource, multifrequency CSEM modeling: Geophysics, **72**, SM177–SM184.

Salako, O., C. MacBeth, and L. MacGregor, 2015, Potential applications of time-lapse CSEM to reservoir monitoring: First Break, **33**, 35–46.

Streich, R., 2016, Controlled-Source Electromagnetic Approaches for Hydrocarbon Exploration and Monitoring on Land: Surveys in Geophysics, **37**, 47–80.

Streich, R., and M. Becken, 2011, Sensitivity of controlled-source electromagnetic fields

in planarly layered media: Geophysical Journal International, **187**, 705–728.

Streich, R., M. Becken, U. Matzander, and O. Ritter, 2011, Strategies for land-based controlled-source electromagnetic surveying in high-noise regions: The Leading Edge, **30**, 1174–1181.

Streich, R., M. Becken, and O. Ritter, 2013, Robust processing of noisy land-based controlled-source electromagnetic data: Geophysics, **78**, E237–E247.

Tietze, K., O. Ritter, and P. Veeken, 2015, Controlled-source electromagnetic monitoring of reservoir oil saturation using a novel borehole-to-surface configuration: Geophysical Prospecting, **63**, 1468–1490.

Tøndel, R., H. Schütt, S. Dümmong, A. Ducrocq, R. Godfrey, D. LaBrecque, L. Nutt, A. Campbell, and R. Rufino, 2014, Reservoir monitoring of steam-assisted gravity drainage using borehole measurements: Geophysical Prospecting, **62**, 760–778.

Vilamajó, E., B. Rondeleux, P. Queralt, A. Marcuello, and J. Ledo, 2015, A land controlled-source electromagnetic experiment using a deep vertical electric dipole: experimental settings, processing, and first data interpretation: Geophysical Prospecting, **63**, 1527–1540.

Wirianto, M., W. A. Mulder, and E. C. Slob, 2010, A feasibility study of land CSEM reservoir monitoring in a complex 3-D model: Geophysical Journal International, **181**, 741–755.

Wright, D., A. Ziolkowski, and B. Hobbs, 2002, Hydrocarbon detection and monitoring with a multicomponent transient electromagnetic (MTEM) survey: Leading Edge (Tulsa, OK), **21**, 852–864.

Zwartjes, P., T. Barker, J. Hornman, and J. Przybysz-Jarnut, 2015, Quantitative Interpretation of Nine Months of Daily SeisMovie^{TM} Data to Monitor Steam Injection at Schoonebeek: 77^{th} EAGE Conference and Exhibition. Extended Abstract.

5

ADVANTAGES AND CHALLENGES OF VERTICAL ELECTRIC-FIELD MEASUREMENTS USING A SURFACE-TO-BOREHOLE CONFIGURATION

A new approach of including the vertical electric-field component E_z in land-based CSEM surveying is investigated. This component is in addition to the conventionally measured horizontal electric-field components and the three magnetic-field components. Synthetic studies have shown that the vertical electric-field component is much more sensitive to resistivity changes in the reservoir. Therefore, it has the potential to measure even minor changes that would be too small to measure with the horizontal electric-field components. We focus on economic near-surface solutions by using shallow boreholes for measuring this vertical component. To that end, three CSEM surveys were carried out at the Schoonebeek oil field with shallow boreholes. The data were processed, analyzed and inverted for a conductivity model where possible. We show that the sensitivity, especially to changes in a reservoir, is higher for the vertical than for the horizontal electric-field components measured near or at the surface. However, resolving depth and resistivity of the reservoir with E_z measurements alone is challenging. Nevertheless, we show that E_z measurements have the potential of detecting resistivity changes and are repeatable and thus might be useful for long-term monitoring applications due to their higher sensitivity to small changes in the target layer.

Parts of this chapter have been published as: Andreas Schaller, Jürg Hunziker, Guy Drijkoningen, and Rita Streich (2014): Sensitivity of the near-surface vertical electric field in land controlled-source electromagnetic monitoring. SEG Technical Program Expanded Abstracts 2014: pp. 838-843. doi: 10.1190/segam2014-1460.1

5.1. INTRODUCTION

Conventional land controlled-source electromagnetic (CSEM) surveys are usually designed such that the two horizontal electric-field components can be measured accurately. In addition, the three magnetic field components are often measured simultaneously with the horizontal electric field. Measuring the vertical electric-field component E_z, however, requires extra effort. Therefore, E_z is generally not measured in an exploration setting. Yet, recent synthetic studies discussed below suggest that the information obtained from the E_z component may be beneficial in a monitoring setting. The goal of this study is to investigate if near-surface E_z measurements indeed provide additional benefits to measuring the horizontal components alone in a setting of long-term reservoir monitoring. If successful, subsurface array measurements may replace surface measurements, i.e. one initial surface-based survey may still be necessary, but subsequent surveys would use subsurface sensors only.

5.1.1. E_z MEASUREMENTS ON LAND

When acquiring CSEM measurements for targets at a few kilometers depth, five components of the electromagnetic field can easily be measured at the Earth's surface. The horizontal electric-field components are recorded using two perpendicular electrode dipoles, typically about 60-100 m long. The three magnetic-field components are commonly measured using induction coils oriented in the N-S, E-W and vertical directions.

The only component lacking is the vertical electric-field component E_z. In a layered earth, the electromagnetic field can be decomposed into a TE-mode (= tangential electric, i.e. no vertical electric field) and a TM-mode (= tangential magnetic, i.e. no vertical magnetic field) (Weidelt, 2007). These modes are coupled only through the source, which generally excites both modes and otherwise propagate without coupling through a layered structure. In theory, when the earth is assumed to consist of a 1D structure that is parallel to the surface, E_z is TM mode only and has no contribution of the TE mode, like, e.g., the air wave. Air waves, which mask much of the subsurface response, thus have no strength on the vertical component (Hunziker et al., 2011; Singer and Atramonova, 2013; Weidelt, 2007) and the air wave is only present in five of the six electromagnetic field components. Under the ideal assumption of perfectly vertical E_z sensors, the amplitudes of E_z generated by a surface Horizontal Electric-Dipole (HED) source are by an order of magnitude and more lower than the magnitude of the horizontal electric-field components primarily due to the absence of the air wave. Thus absolute noise levels in E_z are likely to be lower than in E_x and E_y and more strongly coupled to subsurface resistivity. This was confirmed by previous feasibility studies on land CSEM monitoring that clearly indicate that E_z should be the field component most sensitive to resistivity changes in depth; this was numerically shown for the Ketzin CO_2 storage test site by Streich et al. (2010) and for the SEG/EAGE overthrust model by Wirianto et al. (2010). In both cases, it was concluded that E_z measurements in a well around the reservoir provided the highest sensitivity to relatively small resistive reservoirs. E_z cannot be measured directly at the Earth's surface, because near-surface E_z amplitudes are very small, effectively going to zero at the air-ground interface. However, E_z amplitudes rapidly increase with depth, such that measuring E_z should be possible at shallow depths below the surface. Numerical computations indicate that measuring E_z to depths of roughly 100 m is sufficient

to get high amplitudes, but clearly, logistically more difficult and more expensive than using surface instruments. Although the proposed E_z sensors in boreholes up to 100 m depth are not significantly closer to the reservoir in order to allow for an additional advantage, this non-standard configuration may lessen the influence of man-made near-surface EM noise and noise levels should be lower in E_z than in the horizontal electric-field components, because the receivers are planted in boreholes, slightly further from most electric infrastructure (e.g., power lines and pipelines buried horizontally or installed at a constant height above the surface) than horizontal electric-dipole receivers. Measuring E_z in shallow boreholes may thus be advantageous for noisy areas.

For CSEM sources, similar considerations apply, as a consequence of source-receiver reciprocity. In CSEM surveys nowadays, electric current sources (horizontal dipoles) with a length of the order of 1 km are commonly being used (Streich and Becken, 2011). Vertical electric sources would provide higher sensitivity to resistive reservoirs than horizontal ones, but again require a borehole, which makes them expensive because of borehole costs and accessibility constraints. Still, Tietze et al. (2015b) suggest using existing infrastructure such as metal borehole casings as an active source. Vilamajó et al. (2015) used a deep vertical electric dipole installed at reservoir depth below the steel casing of an injector well and recorded data with low experimental errors and good repeatability at 55 permanent surface electrodes. From an economic point of view, making boreholes for E_z measurements for exploration purposes seems excessively expensive. However, for monitoring purposes, a more permanent setup is often desired to facilitate repeat measurements over time. Also, in monitoring applications, the changes in the subsurface to be detected are more subtle than the structures to be detected in exploration applications. If the target region that requires monitoring is sufficiently well-known, survey geometries can be optimized.

A recent surface-to-borehole CSEM modeling study on monitoring of waterflooding operations (Colombo and McNeice, 2013) indicates that the vertical component of the electric field shows the largest sensitivity to reservoir changes and obtains the best spatial resolution after inversion. Further, this study concludes that surface-to-surface electromagnetic measurements (i.e., surface CSEM or controlled-source audio-frequency magnetotellurics) are not capable of time-lapse monitoring in carbonate reservoir settings whereas the vertical electric field measured in a surface-to-borehole electromagnetic setting might have the potential to detect small changes. Therefore, E_z sensors at carefully chosen locations may be well-suited for monitoring purposes. In those cases, installing E_z sensors in shallow boreholes also becomes economically feasible.

5.1.2. OBJECTIVES

We investigated the suitability of the vertical electric field for detecting resistivity changes related to steam injection. A synthetic study was performed to optimize the survey layout with plausible receiver locations and depths and source locations. Other requirements for receiver installation such as borehole verticality, i.e. required accuracy for determining the accurate well trajectory of the shallow boreholes, were defined. Additional tests were carried out, e.g., to determine the sensitivities of the vertical electric-field component for the site where monitoring was envisaged. Tolerable noise levels were investigated taking into account expected strong noise levels at these sites due to,

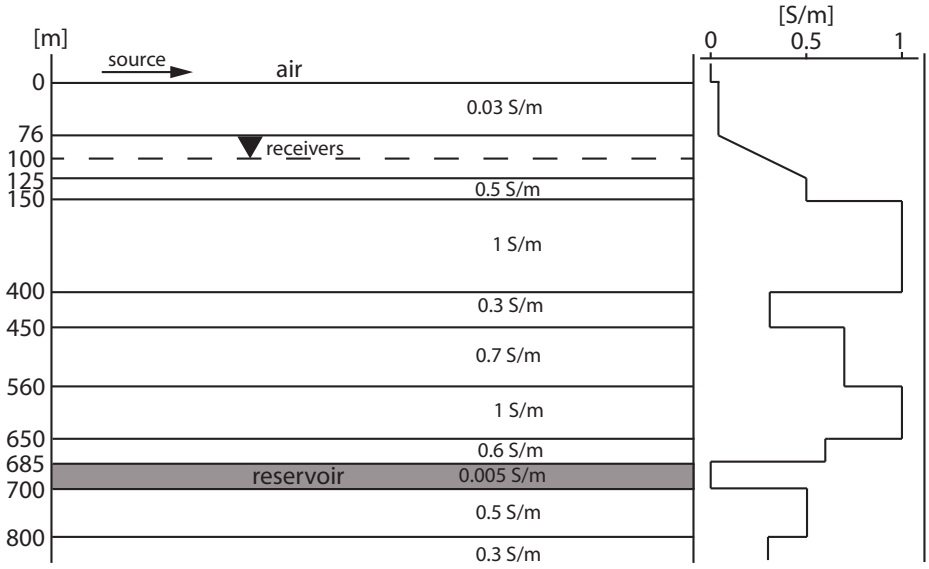

Figure 5.1: Layer model and conductivity profile (in S/m) of Schoonebeek area derived from logging data. The source represented by the black arrow is placed at the surface, and receivers are placed at a depth of 100 m. The conductivity profile is plotted in linear scale to better indicate the conductivity changes of the layers above the strongly resistive reservoir layer.

e.g., producing oil fields, pipelines, power supply for pumps, and various metallic installations that all contribute in creating strong EM noise. The repeatability of E_z measurements in the presence of such noise was studied.

CSEM field experiments were carried out during steam injection that was taking place at the Schoonebeek onshore oil field, using E_z sensors installed in shallow boreholes. The acquired data were processed and will be analyzed for signal-to-noise ratios, repeatability, and the capability of resolving changes at reservoir depth. We investigate the potential of E_z for detecting small resistivity changes, useful for monitoring applications. Finally, inversions for the resistivity distribution will be performed by using the vertical data in addition to horizontal data, aiming to get an improved image of the resistivity distribution inside the reservoir and its changes.

5.2. MODELING STUDY

Prior to the field survey, a comprehensive modeling study was performed. For this study, we assume a horizontally layered model. Such a model is a reasonable zero-order estimate for representing the subsurface structure at the site of our field survey and understanding major effects on EM fields. Because of these assumptions, we used the fast reflectivity forward modeling code EMmod Hunziker et al. (2014). Figure 5.1 shows the 1D model of the Schoonebeek region derived from averaging regional logging data obtained from older well logs (TNO, 2017). The resistivity values of the top 150 m were taken from a recent well log that was taken prior to the survey in the vicinity of the receiver line. The

model consists of multiple layers with different conductivities, and a resistive reservoir at a depth of 685-700 m. Strong electric fields develop inside a resistive reservoir that diffuse faster than through a conductive background and the degree of attenuation through a resistive reservoir is smaller compared to that through a conductive background. We simulate an x-directed HED source. E_z receivers are modeled as vertical electric point devices located 100 m below the surface.

Further, we quantify the sensitivity of the vertical electric-field component and compare it to the sensitivities of the horizontal electric-field component. We investigate how to optimize survey layout, for the choice of source locations and receiver locations and depths with respect to resolving the target reservoir. The effects of expected subsurface changes were quantified, i.e., time-lapse effects due to steam injection via varying the thickness of the steam. Since E_z measurements can be strongly affected by a deviation from verticality, the sensitivity of borehole tilt on the measurement was tested.

In the following computations, use is made of either a point dipole or a dipole source of 1 km length, a typical length for land electric-field sources. A point dipole source can be assumed because synthetic tests with reduced source lengths have shown that the sensitivity range does not depend strongly on the source size for 1D targets. The sensitivity to 3D targets, however, decreases somewhat with source length. Since the signal-to-noise ratio is proportional to the source size, its dipole length should be chosen as large as economically feasible.

5.2.1. COMPARISON OF ELECTRIC-FIELD COMPONENTS

For the model defined in Figure 5.1, an HED point source and a 20 x 20 km area of receivers oriented in the x, y and z directions were considered. As source frequency 0.5 Hz is used, and the source current is 1 A. For the steam-injection scenario, an increased conductivity value of 0.05 S/m is assumed representing the displacement of highly resistive oil by more conductive condensed steam mixed with saline formation water. The modeled associated electric-field amplitudes are shown in Figure 5.2. Figure 5.2a, d and g show the electric-field amplitudes for a model into which a steam layer was included at depth 685 – 690 m. Figure 5.2b, e and h show the electric-field amplitudes for the background model without any injected steam. Figure 5.2c, f and i show the ratios between the pre- and post-injection electric-field data and indicate the sensitivity to changes in the reservoir. The white area at large source-receiver offsets represents regions in which field amplitudes are smaller than 10^{-14} V/m and thus not expected to be measurable. The value of the noise floor is more conservative than commonly used for marine surveys because higher levels of cultural noise are expected on land. However, noise as measured at a later stage in the field as well as recent studies (Tietze et al., 2015b) suggest that a noise floor on the order of 10^{-10} V/m is more realistic for very noisy land data although this value may be significantly lowered by long-time stacking or may be lower in less severely noise-affected data.

The corresponding phases of the electric fields are shown in Figure 5.3. They indicate that phase differences, especially for the E_z component, are larger than 20° for all offsets larger than 1 km. From night-time noise records at the field site, overall amplitudes from (slightly tilted) near-vertical measurements are roughly 5-8 times smaller than the ones of the horizontal components at the same location (Streich, 2016). Although the noise

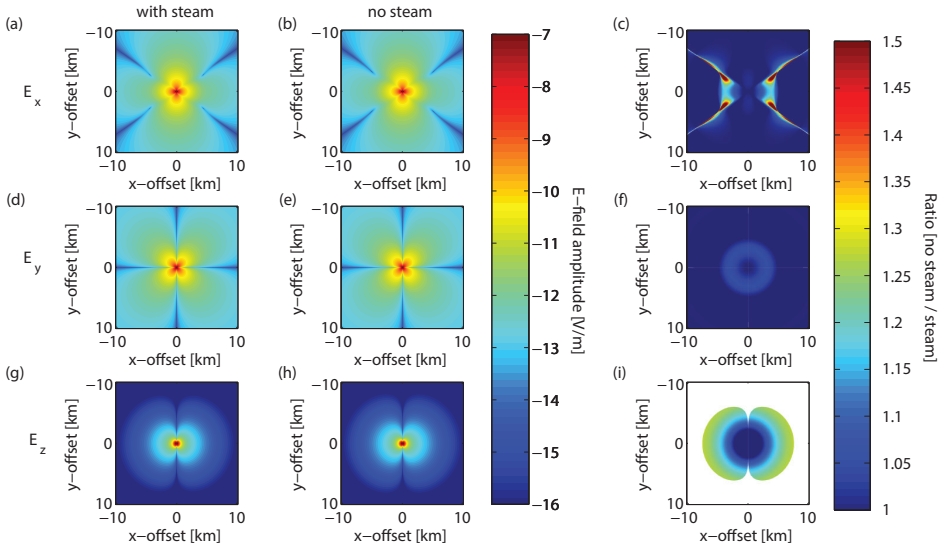

Figure 5.2: Amplitude of electric-field components for the model from Figure 5.1 with a 5 m thick steam layer of 0.05 S/m inside the reservoir (left column) and without steam layer (central column), and corresponding electric-field ratios (right column), for a frequency of 0.5 Hz. Ratios are not shown where amplitudes are below 10^{-14} V/m. E_x (a – c), E_y (d – f) and E_z (g – i) are computed at a depth of 100 m, and an x-directed point dipole HED source is assumed.

level for the vertical component is nearly an order of magnitude smaller, we find it reasonable to assume the same noise level as for the horizontal components, due to a larger decrease in signal levels and additional challenges in measuring the vertical electric field as described below.

As expected, the electric-field amplitudes for vertical receivers are much smaller than for horizontal receivers and decay more rapidly with distance from the source (Figure 5.2g, h). The amplitudes of the horizontal field components due to horizontal sources are above the assumed noise floor for offsets exceeding 10 km (Figure 5.2a, b, d, e). However, the vertical component is much more sensitive to changes in the reservoir. Figure 5.2i shows that the amplitude response of the model including a steam layer differs from the background model response by up to 25% (obviously, short-term changes and thus changes restricted to the vicinity of the steam injection site with a laterally limited steam volume would be significantly smaller). For the horizontal components, the relative changes due to steam injection are minor, except for small areas near the local minima of E_x (Fig. 5.2c), in which reliable measurements would not be possible.

5.2.2. OPTIMIZATION OF SURVEY LAYOUT

In our field study, the target region is confined to the area in about 700 meters depth. A first issue is the minimum source-receiver offset. Previous surveys acquired at Ketzin in Germany (Grayver et al., 2014) stated that receivers placed too close to the source could not be used for inversion due to complex near-source characteristics and due to

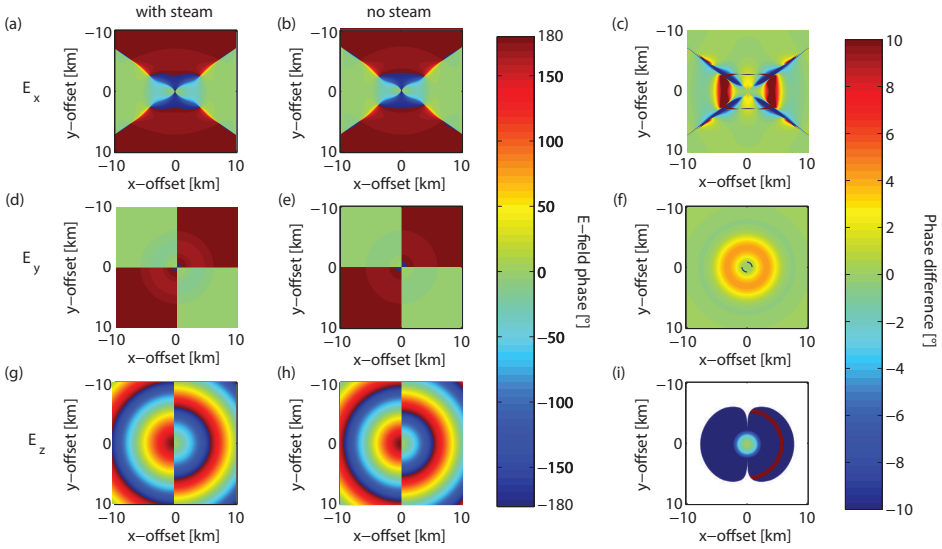

Figure 5.3: Phase of electric-field components for the model from Figure 5.1 with a 5 m thick steam layer inside the reservoir (left column) and without steam layer (central column), and corresponding phase differences (right column), for a frequency of 0.5 Hz. Phase differences are not shown where amplitudes are below 10^{-14} V/m. E_x (a – c), E_y (d – f) and E_z (g – i) are computed at a depth of 100 m, and an x-directed point dipole HED source is assumed.

the strong direct source field that masks subsurface information. Therefore, we suggest that receivers should be placed at least 1 km away from the source. Another issue is the maximum source-receiver offset. At large source-receiver offsets, the data will suffer from low signal-to-noise ratios. The optimal offset range between source and receivers was thus studied considering both electric-field amplitudes and the sensitivity to resistivity changes in the target region assuming a minimal offset of at least 1 km. The same model as defined above (Figure 5.1) was used. To study the influence of variations inside the reservoir, data were created for a model with and without a reservoir layer. This was done for two frequencies, namely 0.1 and 1 Hz.

Figure 5.4 shows the ratio of the response of the model in Figure 5.1 with the reservoir to the response of the same model without the reservoir layer, for the frequencies of 0.1 Hz and 1 Hz. The figure shows at which offsets the reservoir response is the strongest. Data with amplitudes smaller than 10^{-14} V/m have been blanked, as these would likely have an insufficient signal-to-noise ratio to be measured in the field. The dark-red area expresses the area where the response of the model including the reservoir is at least 4 times stronger (ratio cut at that value) compared to the response of the model without the reservoir.

Generally, the reservoir response is clearer and the noise level is reduced when the receivers are deeper and thus closer to the reservoir. Vilamajó et al. (2013) confirmed that placing an electric source at reservoir depth leads to better detectability of time-lapse resistivity changes inside a reservoir. Based on reciprocity, placing a receiver at reser-

(a) Frequency: 1 Hz (b) Frequency: 0.1 Hz

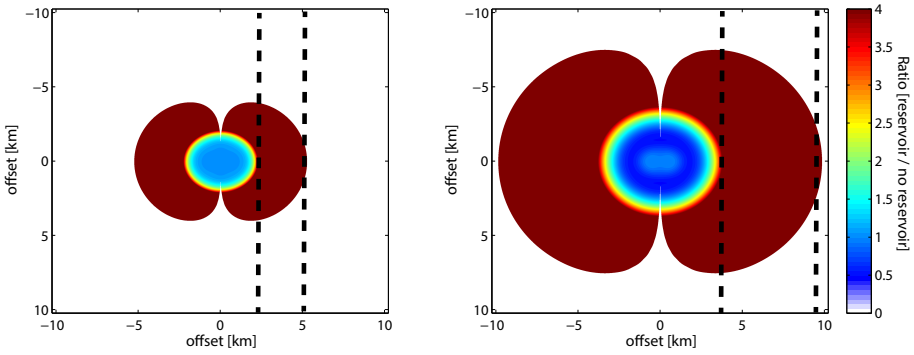

Figure 5.4: Ratio of the vertical electric-field responses with and without a reservoir for a receiver depth of 5 m, where the ratio is made white when amplitudes are below the noise level of 10^{-14} V/m. The black-dashed vertical lines show the best offsets for (a) 1 Hz and (b) 0.1 Hz. The black lines were chosen such that they define the range where the ratio of the vertical electric-field responses with and without a reservoir is larger than 4 and above noise level. Note that the usable offset slightly increases with increasing depth of receivers.

voir depth would lead to the same conclusion. Therefore, the goal is to find a compromise between placing the receivers as deep as possible and being economically feasible. Commonly in The Netherlands, the drilling of shallow boreholes up to some 150 meters can be done rather cheaply while drilling deeper boreholes becomes substantially more expensive. So for the modeling study, the following receiver depths were used: 5, 50, 100 and 150 m. Figure 5.4 shows, for a receiver depth of 5 m, that the sensitivity for the near offsets smaller than 2 km is very low. The best sensitivity to reservoir changes is for source-receiver offsets between 3 to 5 km for 1 Hz and 4 to 9 km for 0.1 Hz. For larger offsets the sensitivity is still good, however, in our model, the signal amplitude is below our assumed noise floor and assumed not to be useful.

5.2.3. SENSITIVITY OF NEAR-SURFACE E_z FOR STEAM-INJECTION SCENARIO

While injecting steam, the size of the steam body increases laterally and vertically over time. To roughly assess the effect of growing steam volume in 1D, we let the thickness of the steam layer increase from 0 to 15 m from the top of the reservoir, assuming a steam conductivity of 0.05 S/m. Correspondingly, the thickness of the remaining reservoir is reduced from 15 to 0 m. For this effect, we determined the amplitude of the horizontal and vertical electric fields which are shown in Figure 5.5. It can be observed that both the E_x and E_z amplitudes depend on the thickness of the steam layer. Whereas relative changes in E_x are minor, changes in E_z are clearly recognizable. Absolute changes of the horizontal electric-field components are larger than for E_z such that for high-fidelity, low-noise data these absolute changes are likely to be measurable as well. The figure thus suggests that resistivity variations due to steam injection should be sufficient to

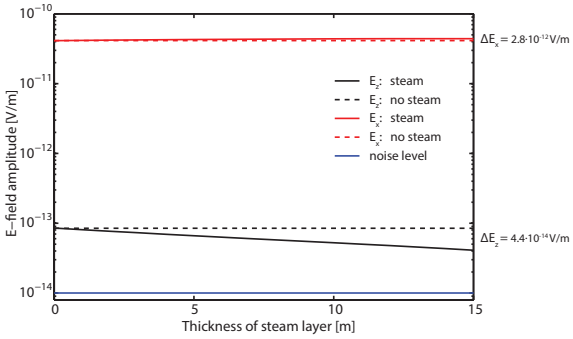

Figure 5.5: Effect of thickness of steam layer on the vertical and horizontal electric-field amplitudes for the model in Figure 5.1 with increasing steam thickness at a source-receiver offset of 4 km for a frequency of 0.1 Hz. ΔE_x and ΔE_z are the absolute changes of E_x and E_z, respectively.

be detectable and E_z amplitude differences, as well as overall amplitude levels, should be sufficiently large to be measurable. Note that 3D reservoir-modeling results (Streich, 2016), however, suggested that resistivity variations are much more complex and lead to areas of increased and areas of reduced resistivity so considering complex 3D variations would give less optimistic feasibility results.

In addition, we tested the sensitivity of E_z by placing three receivers in a homogeneous model. The results are shown in Figure 5.6. It shows that the sensitivity is particularly high in the layers where receivers are located, demonstrating that the strength of the measured vertical electric field is largely controlled by the resistivity of those layers. Also, the electromagnetic boundary condition for vertically propagating currents, which imposes continuity of the normal current density results in sharp electric-field changes where resistivity values vary rapidly. Due to this property, the E_z field might be more sensitive to resistivity anomalies occurring near the receiver (e.g., casing, variable well fluids) or to improperly modeled electrical overburden anisotropy. However, if these near receiver effects can be limited, E_z data might have the power to accurately diagnose 3D resistivity variations inside the reservoir. Also, E_z shows the strongest variability relative to the position of the receivers in a well (Colombo and McNeice, 2013). According to Colombo and McNeice (2013), the E_z component is the most sensitive to the vertical resistivity structure in the overburden and thus must be accurately modeled before attempting any interpretation of E_z field measurements. Therefore, they have numerically tested a surface-to-borehole acquisition geometry using electromagnetic sources located on the surface and receivers located at the reservoir level to avoid sensitivity issues of the vertical electric-field measurements due to the overburden.

Numerous synthetic 1D inversions were executed on modeled E_z data obtained from the model in Figure 5.1. Since E_z is very sensitive to resistivity changes in the vicinity of the receivers, it is necessary to have detailed knowledge about the near-surface, so including the electrical anisotropy where the receivers are placed. As a starting model, a homogeneous 1 Ωm halfspace model with accurate near-surface information of the first 150 m from the model from Figure 5.1, was used. To focus an inversion on the depth range of interest, the near-surface layers are kept fixed during the inversion, and updates

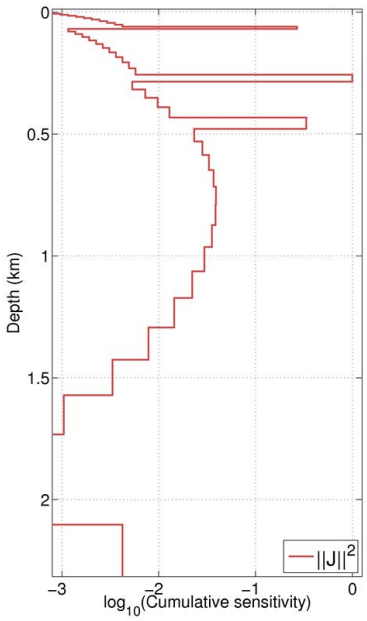

Figure 5.6: Cumulative sensitivity for a 1 Ωm homogeneous half-space model and for receivers placed at depths of z = 60, 260, 460 m. Note the high-sensitivity peaks of the vertical electric field for the layers where receivers are located.

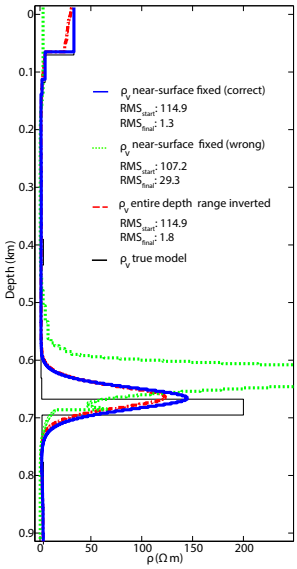

Figure 5.7: Inversion results of computed vertical electric-field data and the impact of a-priori knowledge of the near surface on the inversion performance.

are only allowed in layers below 150 m depth, assuming that the resistivity distribution in the near-surface is known. Figure 5.7 shows three 1D inversion results:

1. the entire depth range was inverted;
2. the near-surface layers were fixed and kept out of the inversion;
3. the near-surface layers were fixed but chosen to be wrong and kept out of the inversion.

It can be seen from the figure that the vertical resolution of the vertical data is not much different than for previously inverted horizontal data (e.g., Chapter 3, Figure 3.13.). However, in contrast to the horizontal data, inversion parameters for the vertical data needed to be properly tuned to get this image. Fixing the near surface where the sensitivity to changes in these layers is high improves the inversion result. Assuming wrong near-surface resistivities lead to poor inversion results and large data misfits. However, the inversion trials showed that the inversion consistently tends to put the resistor at somewhat shallower depths than the actual reservoir suggesting that E_z inversion should be combined with other data to image subsurface features at correct depths. Inversion results from the horizontal electric-field components can be directly used as initial model for the E_z inversion or obtained reservoir depth and resistivity information of the subsurface can be used to improve the starting model. Combined inversion of E_z with the horizontal components could be beneficial but was not taken into account in this study. Low-frequency and single-receiver inversions were tested but gave no improvement so therefore are not shown here.

Hunziker et al. (2016)) inverted TE and TM reflection responses for the subsurface conductivity distribution. The TM-mode reflection response is almost equal to the vertical electric field apart from the fact that there is a horizontal derivative in E_z that is not contained in the TM-mode reflection coefficient. They concluded, in accordance with our findings, that the TM-mode reflection response shows much higher sensitivity to a resistive reservoir than the TE-mode reflection response and that the inversion of the TE-mode reflection response produces a better estimate of the subsurface including a resistive reservoir. Um et al. (2012) showed for a marine example using a Vertical Electric-Dipole (VED) source that 1D inversion of short-offset E_z measurements over complex 3D offshore models can provide useful insights into the lateral extent of a hydrocarbon reservoir, although the measurements lack thickness and resistivity resolution of the hydrocarbon reservoir. Despite the fact that E_z is much more sensitive to a resistive reservoir than the horizontal electric-field components, it was already confirmed by Key (2009) in a marine setting that the resolving power of a resistive reservoir for the vertical electric field is much weaker. The sensitivity of E_z should not be confused with resolution as Constable (2013) stated in his ASEG keynote speech.

Again, as a final remark with our 1D modeling approach: Since the vertical electric field is expected to be more sensitive to 3D structures and 3D effects, the assumption of a 1D subsurface model may be too inaccurate for fitting E_z data at all, and only a 3D inversion might be beneficial.

5.2.4. EFFECTS OF BOREHOLE DEVIATIONS FROM THE VERTICAL

Another crucial issue is the effect when electrodes are installed in slightly tilted boreholes which in reality will always be the case, unless drilling technology is used which is much more expensive than what was available for our field trial. Using numerically modeled data for a marine environment, Hunziker et al. (2011) showed that for a slightly dipping vertical source of 0.05°, the air-wave contribution to the full electric field is about 20%. Because E_z commonly is more than an order of magnitude smaller than the horizontal electric field, not knowing the borehole tilt and thus not accounting for it, would result in wrong interpretation. Our measurements of borehole deviation have shown that shallow boreholes drilled using conventional flushing techniques can deviate from the vertical by more than 3 m (>1.7°) at a depth of 100 m. Figure 5.8 shows, for the example of a 1-km long source and point dipole receivers, that this tilt strongly influences the data. The top row in Figure 5.8 shows vertical electric-field amplitudes for a model with and without steam and their relative difference for a perfectly vertical borehole. Figure 5.8d, e and f show data for a borehole tilted by 3 m per 100 m depth. The electric-field loses its symmetric shape to the y axis and looks more similar to the E_x component rather than the E_z component suggesting that even a relatively small deviation influences the reservoir response significantly. In Figure 5.9 the effect of a borehole tilted by 0.5 m at 100 m depth is given for two different reservoir conductivities of 0.05 and 0.005 S/m for the model shown in Figure 5.1. The simulated changes show an appreciable 4D effect (Figs. 5.9c and 5.9d) and suggest that borehole tilt may have a strong influence on the measured voltage especially in the frequency range of interest between 0.1 and 10 Hz.

Since the tilt of the receiver borehole has significant consequences on the measurement it is necessary to include borehole deviations in modeling for obtaining reliable

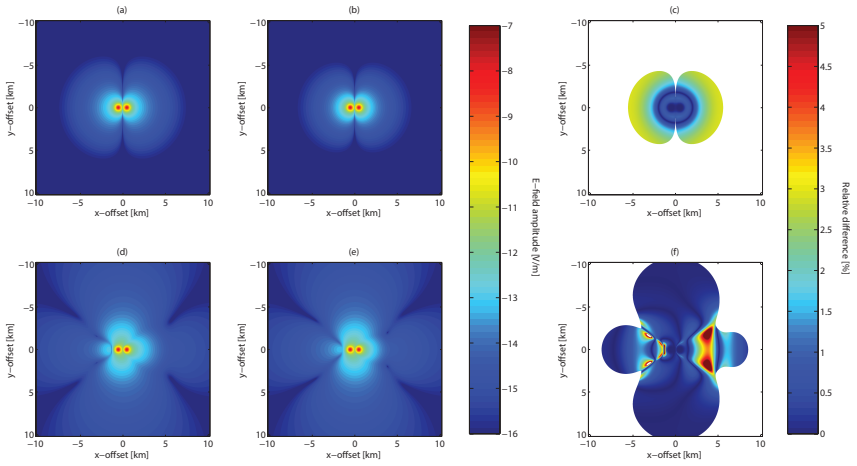

Figure 5.8: Comparison of amplitudes of electric fields that would be measured in a perfectly vertical borehole (a-c) and a borehole tilted by 3 m at a depth of 100 m (d–f), for a frequency of 0.5 Hz and a 1-km long source for a source current of 1 A. Amplitudes normalized by source length are shown for a model with a 5 m thick steam layer (a and d) and without steam (b and e). Relative differences of responses with and without steam are shown in (c) and (f). Regions where amplitudes are below noise floor 10^{-14} V/m are blanked in (c) and (f).

(a) Voltage of vertical and tilted dipole receivers

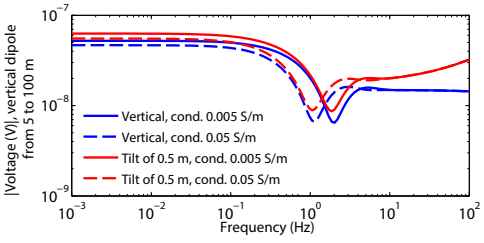

(b) Voltage ratio for tilted to vertical borehole

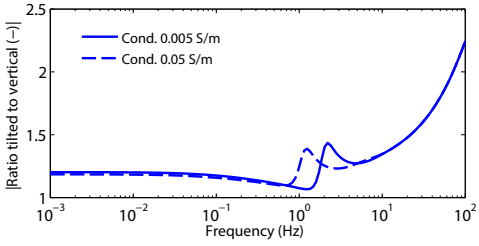

(c) Voltage ratio of conductivities 0.005 to 0.05 S/m

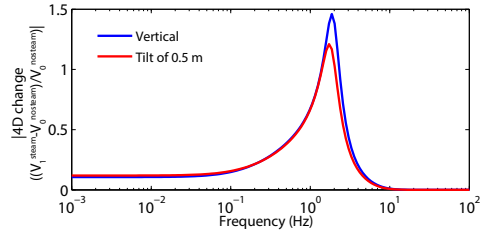

(d) Ratio of 4D changes (red to blue curve from (c))

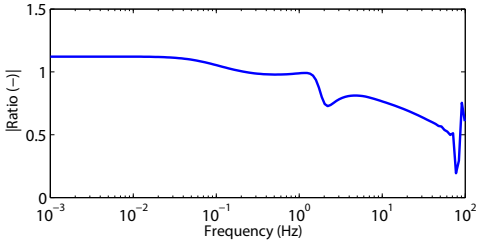

Figure 5.9: Comparison of a perfectly vertical borehole and a borehole tilted by 0.5 m. The source is a 1 km long horizontal dipole (1 A current) and positioned 3 km away from the receiver which is a 95 m long (near-) vertical dipole (5 m to 100 m depth). Electric-field values are converted to voltage as measured in the field.

Figure 5.10: Location of field survey and detailed survey layout. Surface electric field receivers are oriented in the north-south and west-east direction. Transmitters are located west and east of the receiver line. Transmitter 1 west of the receiver line is used for all surveys. Transmitter 2 was shifted to location T3 after the first survey.

results. In case of a borehole equipped with only two electrodes, a shallow and a deep one, the information about the location of the deep electrode could be used to put the surface (shallow) electrode right above the deep electrode and thus avoid the issue of a tilting borehole presuming that the location of the borehole electrodes can be accurately determined.

5.3. FIELD SURVEY

CSEM measurements at Schoonebeek were carried out subsequent to this study (see Chapters 3 and 4). Measurements of the vertical electric field via shallow boreholes, however, are a novelty, and deployment of these electrodes, as well as proper field setup, is challenging.

5.3.1. FIELD SETUP

Three field survey CSEM experiments were carried out at the Schoonebeek field in the Netherlands between 2014 and 2015. The Schoonebeek field is a producing oil field in which steam is injected into a reservoir for enhanced oil recovery. A simplified model of the subsurface derived from logging data was shown previously in Figure 5.1. Source and receiver positions were chosen such that sensitivity to the target area, the reservoir at about 700 m depth in the area of the vertical electric-field receivers, and the signal-to-noise ratio, were optimized (Figure 5.10). Receivers were placed in boreholes 3-5 km away from the two source positions and placed at depths of about 5, 50, 100 and 125 m (Figure 5.11). The exact depth of each receiver achieved, is mentioned in Figure 5.12. The surface receivers to measure the horizontal electric-field components were kept at the

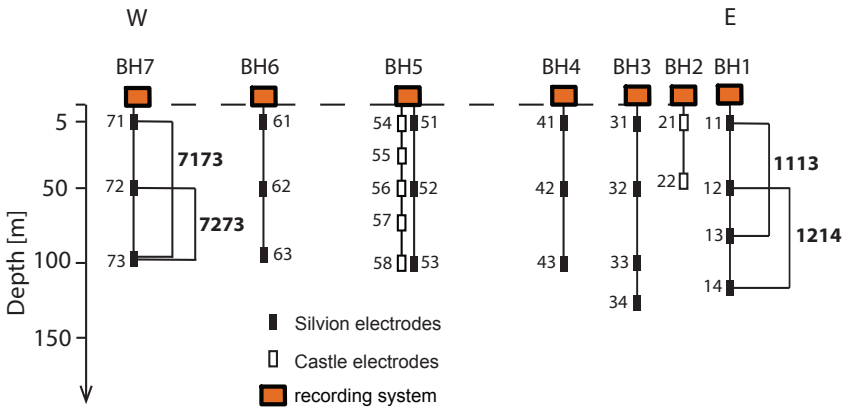

Figure 5.11: Section view of vertical electrodes. Electrodes were given individual numbers where the first digit stands for borehole number and the second digit for electrode number. The latter were numbered sequentially from top to bottom such that '12' would mean electrode 2 in borehole 1. Examples of possible dipole combinations of the electrodes are shown by 1113, 1214, 7173 and 7273.

locations as described in Chapter 2. The vertical receivers remained stationary throughout the first and the two repeat surveys (except for electrode 11 which was replaced by a new electrode at 2 m depth during the first survey as it appeared to be broken). For more details about the Schoonebeek field, survey acquisition, source locations and characteristics, the reader is referred to Chapter 2 and Chapter 3.

As stated in the previous section, reliable E_z measurements require the electrode dipole in the boreholes to be as close as possible to the vertical. As an alternative to non-metallic casing and to avoid introducing conductive features near the electrodes, downhole electrode deployment was attempted using rotary flush drilling without casing. After placing the electrodes, the unsupported boreholes naturally collapse and bury the electrodes while preserving the earth structure, with only minor modifications along the borehole path due to the drilling mud. The electrodes used were chosen due to their shape (thin with large contact surface) and manufacturer's specifications (long-term usability and stability). Six of the boreholes were equipped with Ag/AgCl WE200 electrodes (from Silvion Ltd.) and two boreholes were equipped with Ag/AgCl LD25 electrodes (from Castle Electrodes Ltd.) to additionally compare the quality of both electrode types. Small-scale field testing of the Ag/AgCl Silvion WE200 electrodes prior to deployment at Schoonebeek had confirmed their ability to record consistent EM signals under Northern Netherlands' field conditions. However, longer-term observations later revealed that contact resistances increased more rapidly than anticipated. During the ~2.5-year period of time-lapse experiments, we observed a rise from about 500 Ω to roughly 3.5 $k\Omega$ for most of the shallow and mid-depth electrodes, and somewhat smaller rise for the deepest electrodes (Figure 5.12). Also, the large tip making ground contact consisting of porous material that proved to be quite fragile. Several electrodes broke during preparation for deployment and temporary burial at Schoonebeek while contact resistance measurements suggest a failure of one electrode after deployment. Different

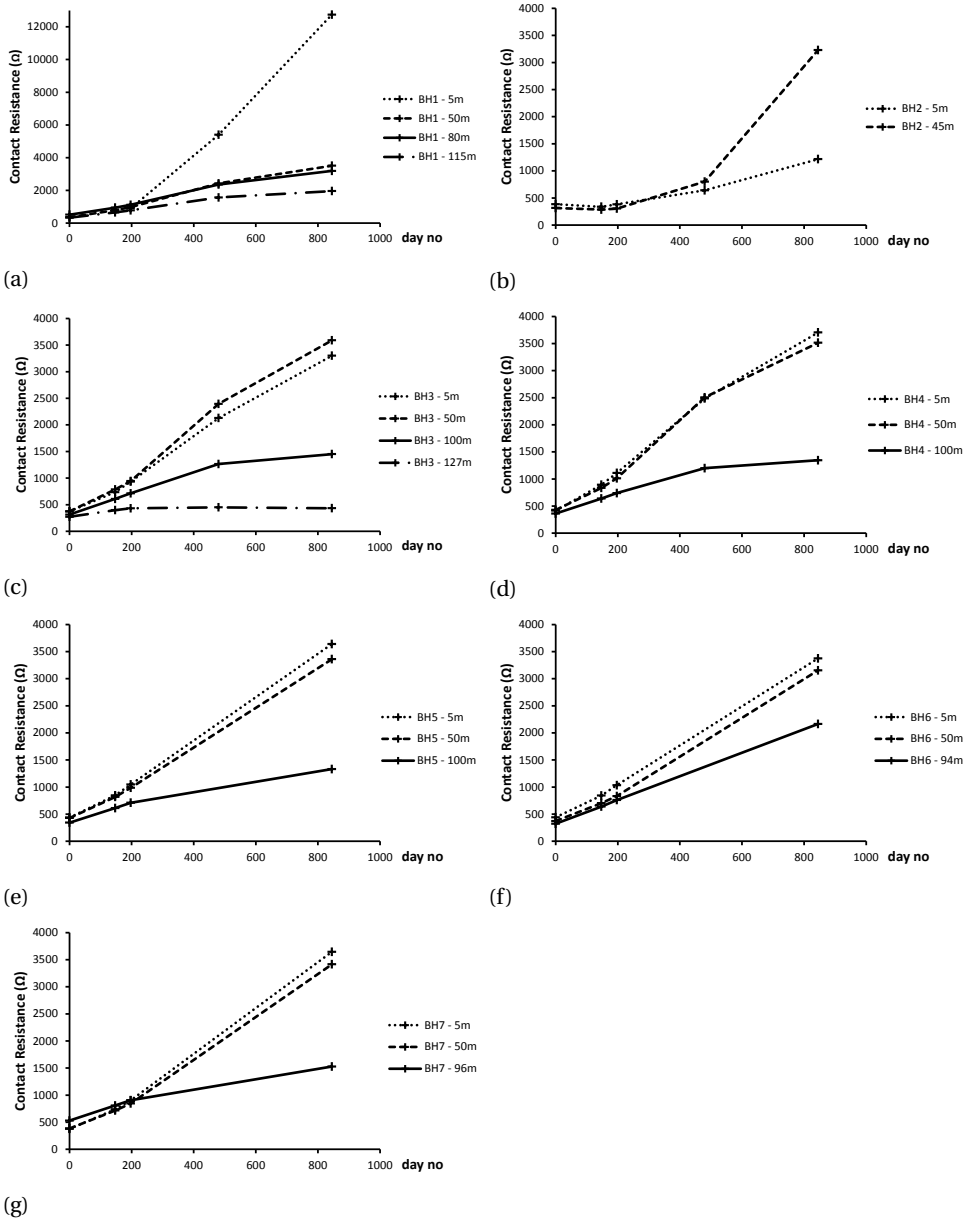

Figure 5.12: Contact resistances of WE200 electrodes from Silvion Ltd. in boreholes BH1, BH3 and BH4, and of LD25 electrodes from Castle Electrodes Ltd. in BH2. Day 0 is 25 July 2013.

(a) (b)

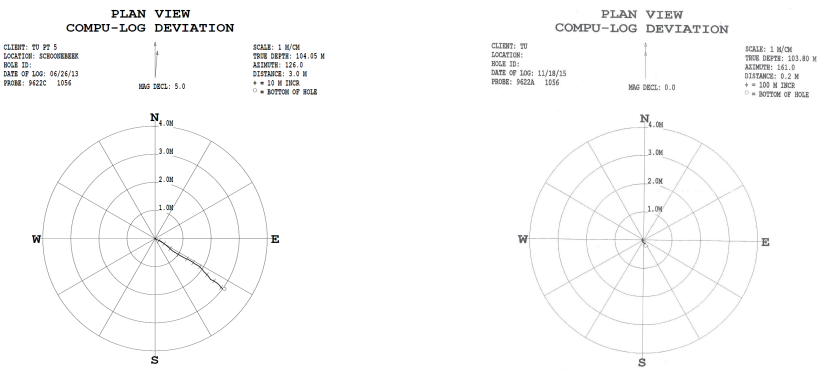

Figure 5.13: Deviation measurements at Schoonebeek. Plan view of the deviation of the (a) old less vertical and (b) new more vertical borehole 5. Mark '+' in (a) gives 10-meter increment.

electrodes would, therefore, be needed for future surveys although off-the-shelf electrodes that function properly for a longer time in a saline sedimentary environment did not seem to exist at the time of the studies. Recently, a prototype of a borehole sensor for measuring E_z in a borehole was developed by GFZ Potsdam (Tietze et al., 2015a).

Borehole 5 had a deviation of 3 m from verticality for the first 100 m. An additional more vertical borehole was drilled at a later stage 10 m away from this existing borehole to allow comparison between these two boreholes. The new borehole was drilled with improved drilling technology, taking learnings from the drilling of the previous boreholes into account, to achieve a more vertical borehole than the seven older ones. The new borehole was about one order of magnitude more vertical than the other boreholes (deviation 0.21 m at 100 m depth compared to previous deviations between 0.8 and 3 m at that same depth). The new borehole was equipped with Castle LD25 electrodes, which are more robust against mechanical damage and had been observed, up until the second field survey (i.e. day 475 in Figure 5.12), to have somewhat more stable contact resistances than the Silvion WE200 electrodes used in most of the previous boreholes.

To precisely determine the inclination of the borehole and to further correct for the receiver dipole tilt in modeling, inversion and interpretation of the data, borehole deviation measurements were conducted separately at each borehole location. This was achieved by lowering a logging tool into the borehole prior to placing the receivers inside the borehole. An example of such a measurement indicating the direction of the deviation and the deviation as a function of depth is shown in Figure 5.13 for the old and the new borehole 5. In borehole 1, the maximum deviation of 3.4 m was measured at a depth of 148.32 m.

For all surface stations, the entire receivers were re-installed for each survey. The S.P.A.M. Mk.IV systems of GFZ Potsdam were used. At most of the borehole stations, Metronix ADU 07e recorders were used.

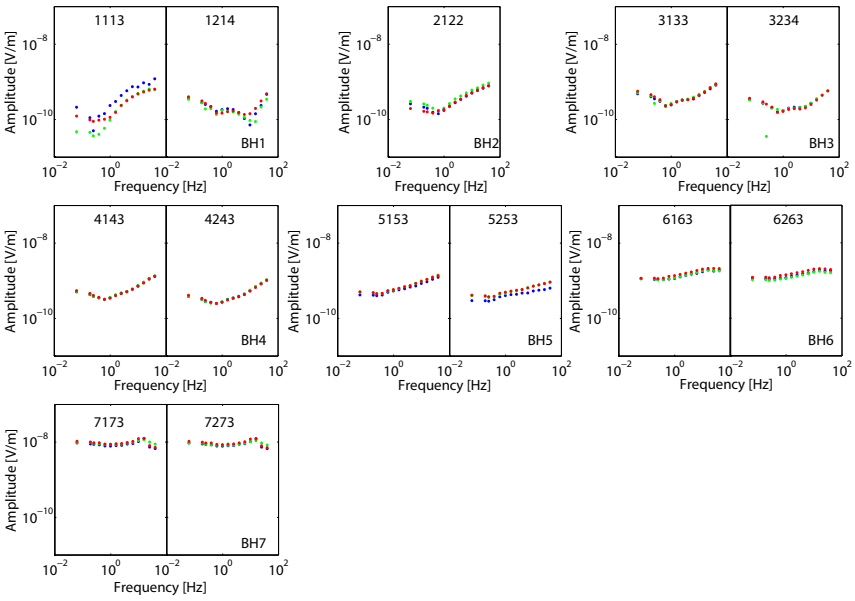

Figure 5.14: Amplitude of response functions of all vertical receivers after notch filtering (50 Hz and harmonics) component $T_{1,3}^{E_z}$ obtained for first (blue dots), second (green dots) and third (red dots) survey for transmitter location 1 (base frequencies of 1/16 and 1/4 Hz only).

5.3.2. RESULTS

The vertical electric-field data of the three surveys were processed following the procedure described in Chapter 2 and 3. Figures 5.14- 5.17 show response function amplitudes and phases for the E_z field component for two chosen polarizations for transmitter location T1. The response functions were processed for the vertical electric field E_z and two source current combinations (I_1, I_3) and (I_2, I_3) using base frequencies of 1/16 and 1/4 Hz for best comparability between all three surveys following the procedure in Chapter 3. The numbers on the top of each figure indicate the electrode combination according to Figure 5.11. For the majority of the dipole combinations, amplitudes and phases were repeatable although variations between the surveys were found to be larger than for the horizontal components (see Chapter 4).

Figure 5.18 shows a comparison of response functions from horizontal and vertical data from two locations close to each other (see locations in Figure 5.10). The overall amplitude behavior is similar, although the vertical field amplitudes are about one order of magnitude lower. Phase differences are 20-30°. Overall, the vertical data are noisier (see error bars) compared to horizontal data.

The influence of borehole tilt on amplitude and phase was tested in the field by comparing the two closely-spaced boreholes at borehole location 5 (Figure 5.13). Figure 5.19 compares time series for the two boreholes. Amplitudes are strongly reduced especially for the shorter electrode dipole (50 m - 100 m) when the borehole is more vertical. The corresponding amplitude and phase responses of the two boreholes are shown in Fig-

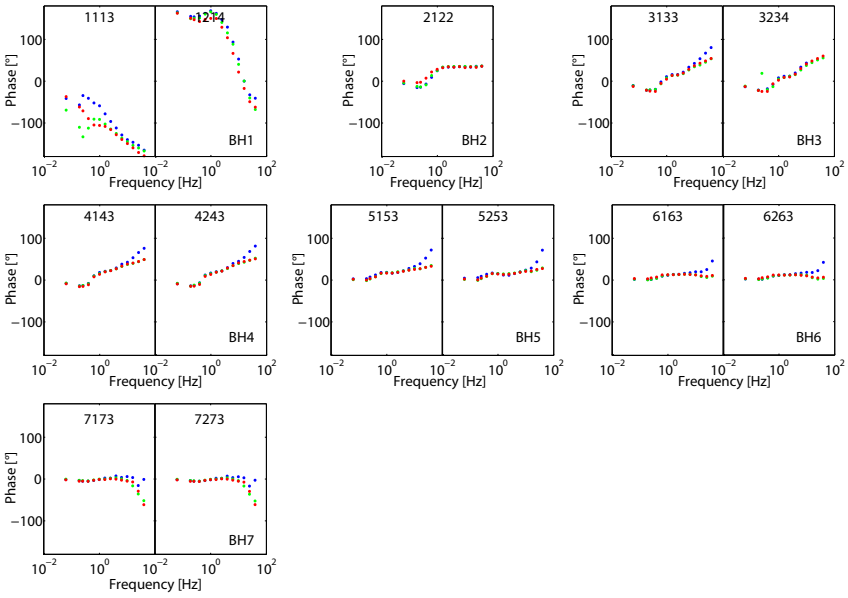

Figure 5.15: Phase of response functions of all vertical receivers after notch filtering (50 Hz and harmonics) component $T_{1,3}^{E_z}$ obtained for first (blue dots), second (green dots) and third (red dots) survey for transmitter location 1 (base frequencies of 1/16 and 1/4 Hz only).

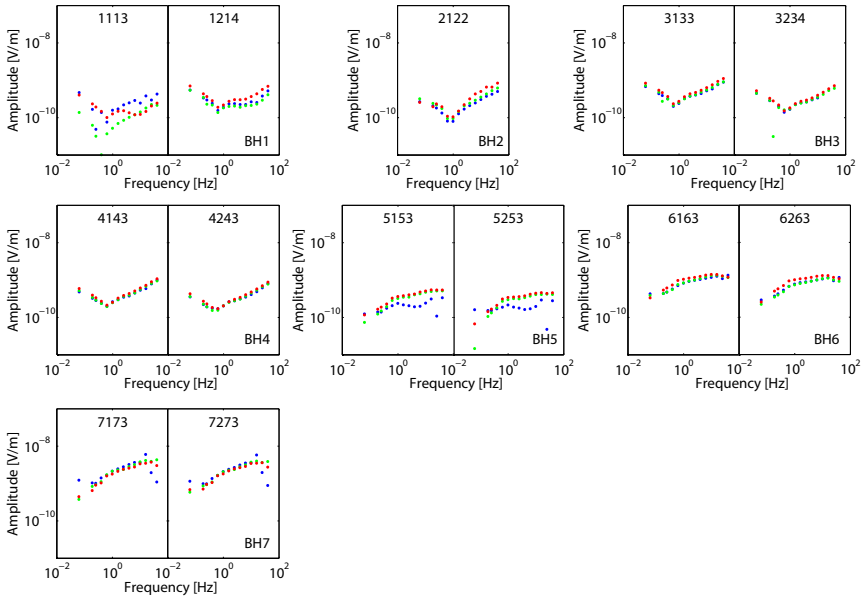

Figure 5.16: Amplitude of response functions of all vertical receivers after notch filtering (50 Hz and harmonics) component $T_{2,3}^{E_z}$ obtained for first (blue dots), second (green dots) and third (red dots) survey for transmitter location 1 (base frequencies of 1/16 and 1/4 Hz only).

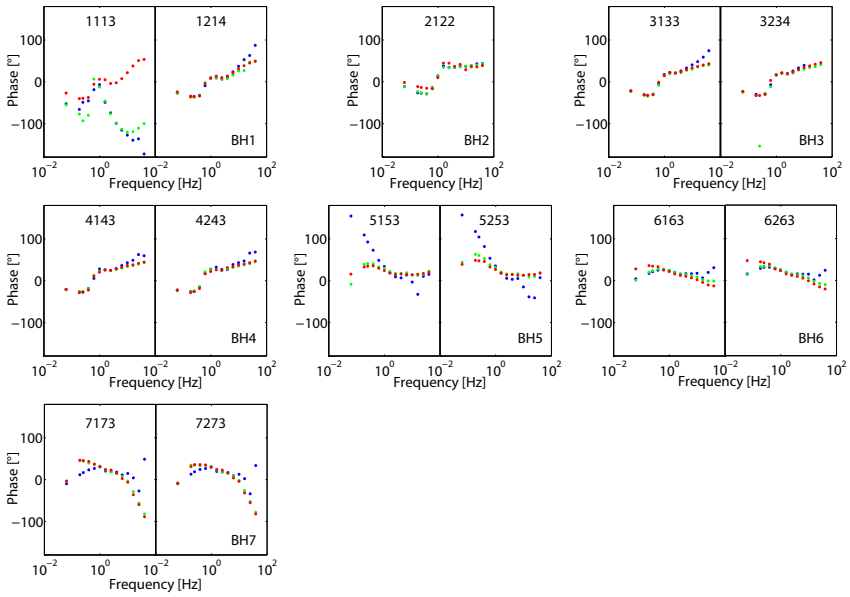

Figure 5.17: Phase of response functions of all vertical receivers after notch filtering (50 Hz and harmonics) component $T_{2,3}^{E_z}$ obtained for first (blue dots) and second (green dots) survey for transmitter location 1 (base frequencies of 1/16 and 1/4 Hz only).

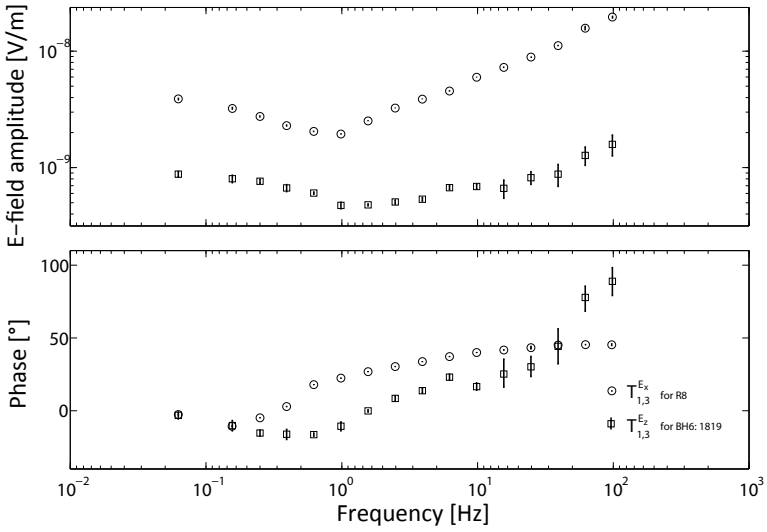

Figure 5.18: Comparison of response function $T_{1,3}^{Ex}$ and $T_{1,3}^{Ez}$: Horizontal data is obtained from surface station R8 and vertical data is obtained from borehole BH6. The error bars indicate uncertainty estimates.

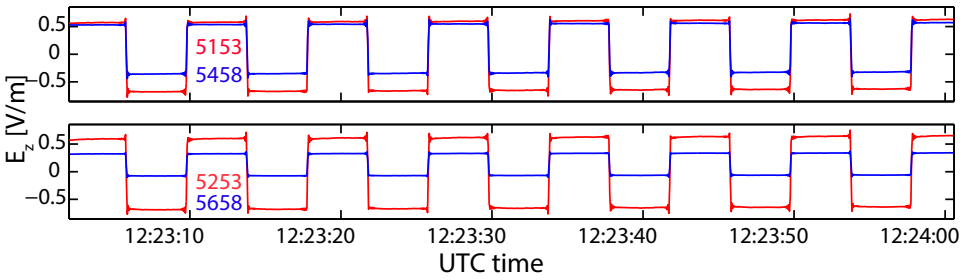

Figure 5.19: Comparison of time series of old less vertical (red) and new more vertical (blue) borehole BH 5 for long dipole between 5 and 100 m (top) and shorter dipole between 50 and 100 m (bottom). The signal was created by a small EM source (Phoenix T3) approximately 200 m away from the borehole.

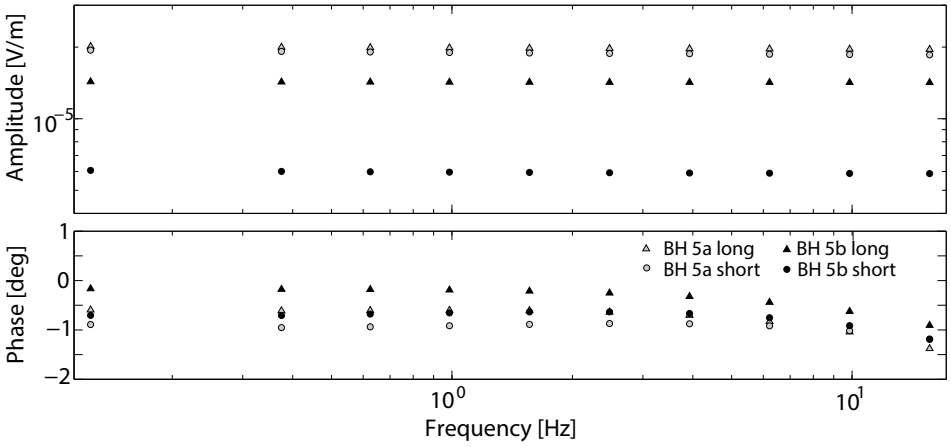

Figure 5.20: Amplitude and phase of response functions for the vertical electric field of old less vertical (gray) and new more vertical (black) borehole BH 5 for long dipole between 5 and 100 m (triangles) and short dipole between 50 and 100 m (circles) and for a large-amplitude source signal from a nearby small EM source.

(a) Before inversion

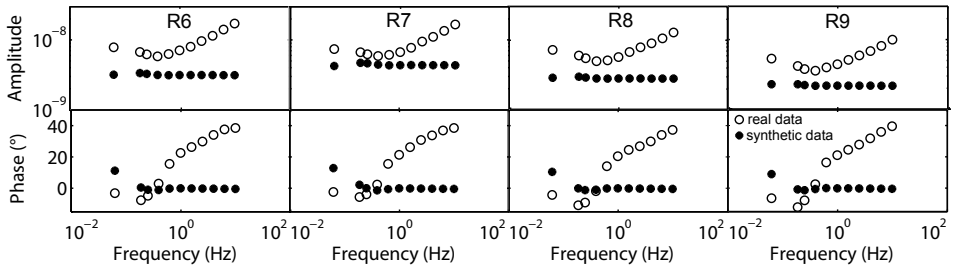

(b) After 12 iterations

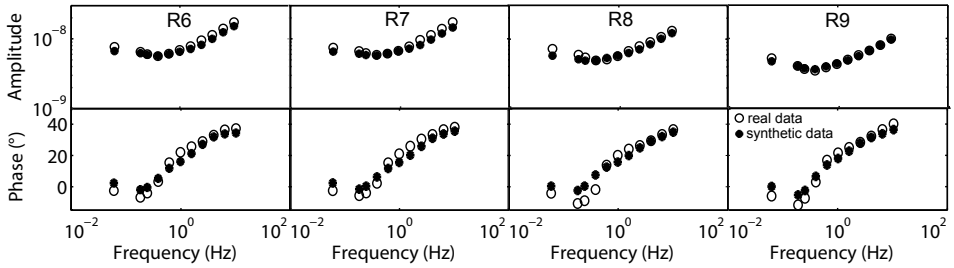

Figure 5.21: Field amplitudes and phases of horizontal electric-field data for four central receiver stations compared with synthetically calculated amplitudes (a) before and (b) after 1D inversion.

ure 5.20. The amplitudes of the new and more vertical borehole are approximately half the magnitude for the short dipole. The phase behavior, however, is similar and depends only infinitesimally on the verticality of the borehole. This may be different for sources further from the boreholes, though.

5.4. REAL DATA RESULTS AND INTERPRETATION

Inversion of the horizontal electric-field data was done in the previous chapters 2- 4. In order to invert for the vertical electric field, understanding of the field data, i.e. their amplitude and phase behavior, is essential. Figure 5.21 shows a comparison of real data response functions to modeled response functions before and after 1D inversion with 12 iterations for the horizontal electric-field data. As a starting model, the model of Figure 5.1 was assumed. For a detailed description of the inversion algorithm and used parameters, the reader is referred to Chapter 3. The modeled data in Figure 5.21 is close to the real data and the 1D inversion is able to improve the misfits between the data and the model for all receiver positions.

This model as obtained for the horizontal data was used as the starting model for inverting the vertical electric-field data. The obtained forward-modeled vertical electric-field data have lower amplitudes than the observed field data for most of the vertical dipoles even though the borehole tilt was properly accounted for in the forward modeling (Figure 5.22). The electrode dipoles show unexpectedly high amplitudes that cannot

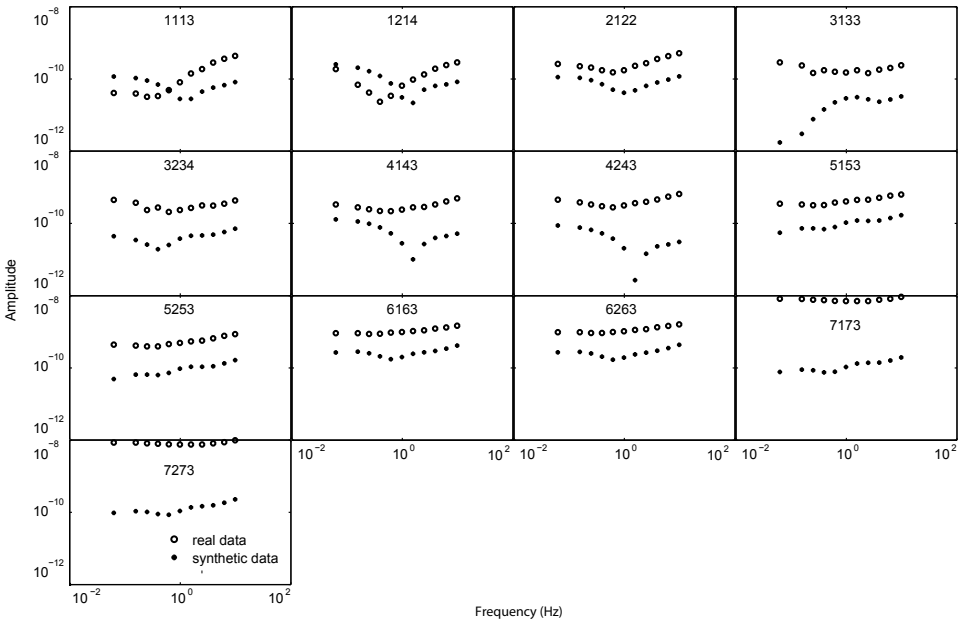

Figure 5.22: Field amplitudes of vertical electric-field data compared with synthetically calculated amplitudes for all dipole combinations.

be explained by a simple 1D model. Tests on 3D modeling have shown that even more complex 3D structures failed to model these high amplitudes. Since a good guess of the subsurface resistivity distribution can be made due to available well-log data, the high amplitudes are likely a result of nearby metal structures such as well casings and pipelines.

In order to investigate the effect of well casings, seven highly conductive steel casings close to the receiver line were incorporated into a 3D model (Figure 5.23). In the forward modeling, an effective-medium approximation was used since the size of the steel casing is much smaller than the grid size used. For the steel casing, a conductivity of $2 \cdot 10^{-7}$ Ωm, a well casing radius of 10 cm and a casing thickness of 1 cm, were assumed. Well locations and casing depth were obtained from Shell's well database but to our knowledge are also publicly available online from the Netherlands Oil and Gas Portal (TNO, 2017). For simplicity, all casings were assumed to be perfectly vertical. The model grid around the well locations was locally refined to lateral cell dimensions of 10 m×10 m. The effective-medium approximation is used to assign well resistivities for each depth level to the entire grid cell. The well casing's vertical resistivity per grid cell is determined by three resistors acting in parallel

$$\frac{A}{\rho_v} = \sum_{i=1}^{3} \frac{A_i}{\rho_i}, \tag{5.1}$$

where A_i and ρ_i are the areas and resistivities of mud, steel and background, respec-

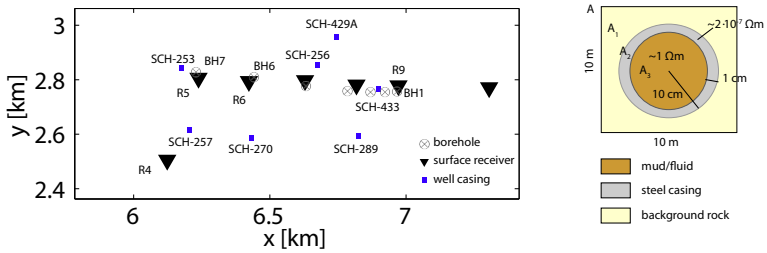

Figure 5.23: Location of modeled casings. Casings were modeled laterally as squares of size 10×10 m with an average conductivity of 1/300 Ωm using an effective medium approximation. Casing depth information of each well was obtained from Shell's well database.

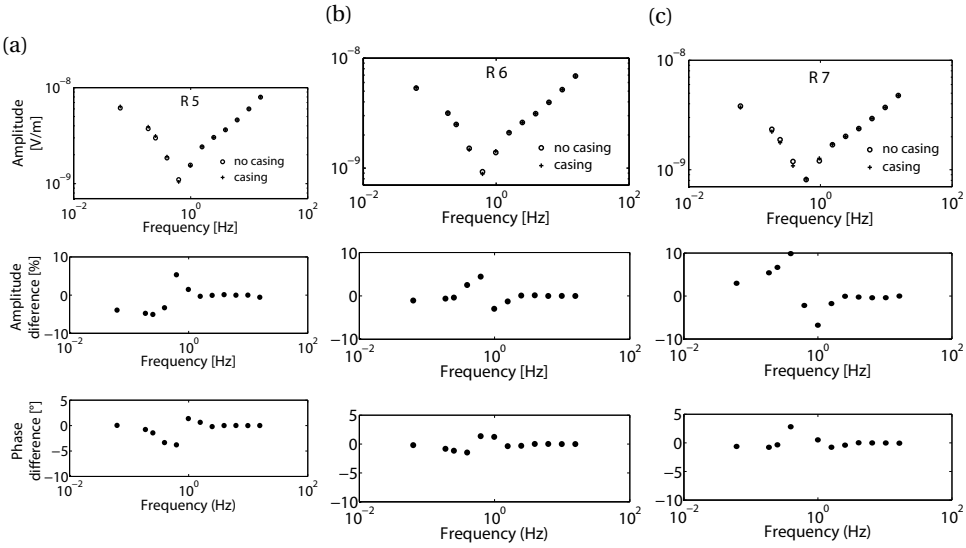

Figure 5.24: Influence of well casings on horizontal electric-field component E_y from 3D modeling for stations (a) R5, (b) R6 and (c) R7.

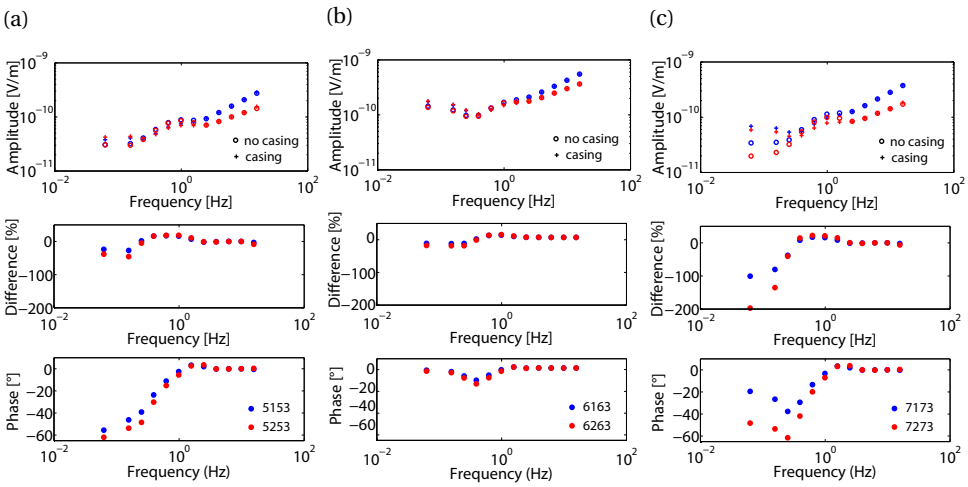

Figure 5.25: Influence of well casings on vertical electric-field component E_z from 3D modeling for boreholes (a) BH5, (b) BH6 and (c) BH7. Amplitude and phase differences for both short (blue) and long (red) dipole are plotted.

tively, and A is the area of the entire model grid cell. Assuming an average background resistivity of 10 Ωm (0.1 S/m), we obtain a vertical resistivity of $\rho_v \approx 1/300$ Ωm. The horizontal resistivity is determined by three resistors acting in series. Since the calculated horizontal resistivity does not differ much from the background horizontal resistivity, it is assumed to be not affected by the well casings. The effective-medium approach is simple, but possibly very inaccurate such that further studies should use a more sophisticated approach.

The influence of the seven well casings on the electric-field components E_y and E_z is shown in Figures 5.24 and 5.25. Figure 5.24 shows, within the approximations made for modeling (true casing effects can be different), that models including well casings lead to changes in E-field amplitudes and phases of up to 10% for the horizontal electric-field component E_y, specifically in the frequency range of 0.1 to 2-3 Hz. While E-field amplitudes for receiver R5 increase for lower frequencies, they decrease for lower frequencies for receiver R7 when incorporating the casings into the model. The influence of the seven casings to the vertical electric field is shown in Figure 5.25 for the three boreholes closest to the three surface stations R5, R6 and R7. The influence of the well casings on E_z is large and the E-field amplitudes generally increase. Borehole 7 closest to a well casing (SCH-253) shows the strongest amplitude change, of up to 200%. This is in agreement with the large amplitudes observed in the real data for borehole 7 (Figure 5.22). However, the different amplitude levels of the real and modeled data cannot be explained solely by the influence of the well casings. Tests have shown that the influence of the borehole casings on overall amplitude is too low and can even lead to a slight decrease in the observed amplitudes. However, the effective medium approximation cannot be expected to model well casing effects accurately. Additional modeling studies, not shown here, using the COMSOL Multiphysics®Modeling Software have supported the observation

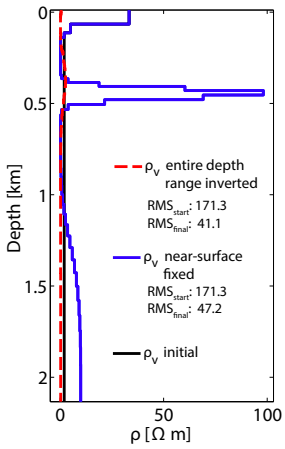

Figure 5.26: Effect of a-priori knowledge of near surface on real vertical electric data inversion using a homogeneous halfspace of 2 Ωm with accurate near-surface data for the first 150 m as starting model.

that the influence of well casings near the receiver and source side are present but are not in the magnitude range of the field data deviation. Ongoing studies indicate that a horizontal pipeline that is crossing the vertical array influences the measurements by an amount similar to the amount observed in the field data. Therefore, for proper inversion studies, pipeline structure and well casings, as well as other conductive bodies, have to be considered and accurately modeled.

It has not (yet) been possible to fit the borehole receiver stations during a 1D or 3D inversion and large misfits remained after inverting the data. A proper starting model with all conductive bodies that affect the measurements still has to be found.

Further, we tested the effect of the near surface on the inversion results. Figure 5.26 shows 1D inversion results of field data for a source polarization of 100°. The red dashed line indicates the inversion result after inverting the entire depth range whereas the blue solid line indicates the inversion result after inverting only the depth range below 150 m. The reservoir can be seen at a shallower depth (around 500 m instead of ~780 m), demonstrating again that resolving the location of the reservoir in depth and amplitude is challenging. The inversion trials on real data contrasts the findings of the modeled example shown in Figure 5.7. Even if we fix the resistivity values in the first 150 m, the inversion is not capable of resolving the reservoir at its true depth.

5.5. DISCUSSION ON FIELD CHALLENGES OF E_z MEASUREMENTS

In contrast to conventional surface-based horizontal electric-field measurements, the non-standard measurement of the vertical electric-field component via shallow boreholes led to additional challenges to field acquisition and processing. Assessment of the active CSEM data has revealed that the observed amplitudes of the vertical electric-field

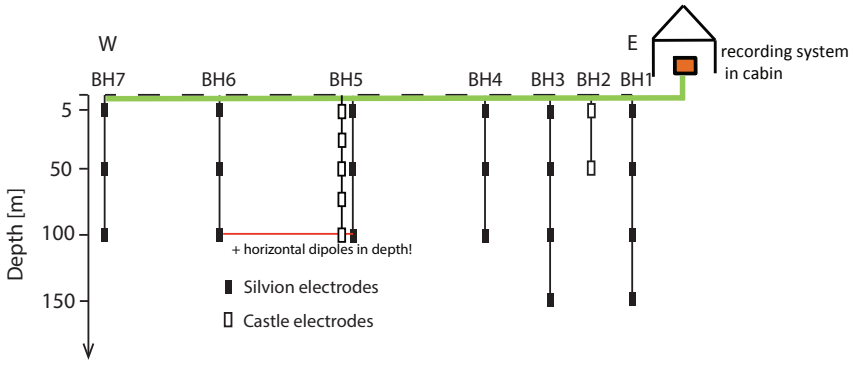

Figure 5.27: Section view of initially planned acquisition setup with only one recording system.

were higher than predicted from modeling studies even when the exact borehole tilt was incorporated into modeling. Modeling studies indicated that the E_z component is more influenced by metal structures such as pipelines and well casings than the horizontal electric-field components. Vertical dipoles should be either positioned as far away from metal bodies as possible or the metal bodies have to be accurately incorporated into the modeling.

The E_z data were found to be noisier than expected, most likely due to man-made EM noise. In addition, the contact resistances of the borehole electrodes linearly rose over time and are expected to increase further. Although this increase most likely is not a serious problem in the short term, the trend of the linear increase, however, might be problematic for future surveys since higher contact resistances will lead to noisier data. Possible reasons of rising contact resistance include: (1) the erosion of the contact surface of the electrode, (2) drying out of the contact/electrode or (3) contamination of the electrode by dirt. Nevertheless, the three surveys gave similar responses, but repeatability was not good in view of the 1% target error required for time-lapse imaging.

For the first survey, signal-to-noise ratios of E_z for the second transmitter T2 were such that the signal was barely visible at the most distant vertical receiver dipoles suggesting that the second transmitter was too far from the electrode array to make interpretable E_z recordings. As a consequence, transmitter location 2 was relocated toward the receiver array for the repeat surveys. The source-receiver offset range usable for E_z-based imaging was thus more limited than predicted from the initial modeling.

Initially, a setup was planned in which the signal was transmitted through long cables (up to nearly 1 km) to a single recording unit placed in a cabin at one end of the electrode array (Figure 5.27). This simple setup proved impossible, because the cables picked up strong noise that completely masked the CSEM signal. An ad-hoc solution of installing recording equipment next to the electrode holes was thus implemented resulting in data of much better quality when compared to the initial setup (Figure 5.11). Although this worked, it is impractical for time-lapse measurements since this would require maintaining and powering expensive acquisition units in the field. Data transmission to a single recording unit as shown in Figure 5.27 would allow for real-time quality control

and for more flexible receiver geometries. In principle, such a layout would allow us to form receiver dipoles between any two of the buried electrodes and would lead to the possibility of measuring horizontal dipoles in depth. The measured horizontal electric field may be of better signal quality than the electric field measured at the surface, since the receivers are located slightly closer to the area of interest and slightly further away from the surface where man-made noise sources are expected to be the strongest. Tietze et al. (2015b) showed that although field amplitudes are close to the smallest resolvable signal levels, resistivity changes can be observed if receivers are deployed close to the reservoir. Active amplifier electronics for transmitting the signal to a central recording location were therefore developed and tested in order to be operational for future surveys (but are not discussed in this thesis).

5.6. CONCLUSIONS

Due to the much larger resistivity time-lapse signature compared to the associated acoustic property changes, CSEM methods and especially the more sensitive vertical electric-field component E_z, in theory, has a good potential for monitoring applications in detecting small changes in the reservoir. Therefore, the advantages and challenges of measuring E_z via shallow boreholes in addition to surface-measured horizontal electric-field components was investigated. Sensitivity analyses have shown that E_z is very sensitive to reservoir changes. It also shows that the influence of borehole deviation has to be taken into account. Vertical electric-field data are much more difficult to fit via modeling than horizontal field data; E_z inversions are less stable, returning a reservoir at its known depth only after careful tuning of inversion parameters. Synthetic studies revealed that cumulative sensitivity to the depth range containing the receivers is 1-2 orders of magnitude higher than to other depths, resulting in decreased vertical resolution of E_z. A-priori knowledge, such as resistivity distribution obtained after 1D and 3D inversion of horizontal electric-field data and additional near-surface resistivity information, should be included for a better constraint. Nevertheless, E_z has the ability to detect resistive changes at reservoir level, i.e. the ability to distinguish between reservoir and no-reservoir cases.

The analysis of the real E_z data has shown that recording the vertical electric field accurately and reliably is challenging. Apart from the expected lower signal amplitudes compared to the horizontal electric-field components, relative noise levels were higher indicating that more attention on minimizing noise sources is necessary in order to improve the signal-to-noise ratio. Real E_z data measurements were fairly repeatable between the three surveys but could not (yet) be fitted to an acceptable level and consequently a reliable subsurface model from E_z data is still missing. Synthetic data for models that include the exact position of nearby well casings show large differences in E_z amplitude and phase compared to data for a metal-free subsurface, suggesting that (1) accurate inclusion of position and trajectories of well casings and pipelines into the initial model for inversion along with (2) accurate modeling, using more accurate approaches than effective-medium averaging in future studies may lead to better data fits.

REFERENCES

Colombo, D., and G. McNeice, 2013, Quantifying surface-to-reservoir electromagnetics for waterflood monitoring in a Saudi Arabian carbonate reservoir: Geophysics, **78**, E281–E297.

Constable, S. C., 2013, Marine CSEM: An Academic's Perspective on the Past, Present, and Future: Presented at the ASEG keynote.

Grayver, A. V., R. Streich, and O. Ritter, 2014, 3D inversion and resolution analysis of land-based CSEM data from the Ketzin CO2 storage formation: Geophysics, **79**, E101 E114.

Hunziker, J., E. Slob, and W. Mulder, 2011, Effects of the airwave in time-domain marine controlled-source electromagnetics: Geophysics, **76**, F251–F261.

Hunziker, J., J. Thorbecke, J. Brackenhoff, and E. Slob, 2016, Inversion of controlled-source electromagnetic reflection responses: Geophysics, **81**, F49–F57.

Hunziker, J., J. Thorbecke, and E. Slob, 2014, The electromagnetic response in a layered vertical transverse isotropic medium: A new look at an old problem: Geophysics, **80**, F1–F18.

Key, K., 2009, 1D inversion of multicomponent, multifrequency marine CSEM data: Methodology and synthetic studies for resolving thin resistive layers: Geophysics, **74**, F9–F20.

Singer, B., and S. Atramonova, 2013, Vertical electric source in transient marine CSEM: Effect of 3D inhomogeneities on the late time response: Geophysics, **78**, E173–E188.

Streich, R., 2016, Controlled-Source Electromagnetic Approaches for Hydrocarbon Exploration and Monitoring on Land: Surveys in Geophysics, **37**, 47–80.

Streich, R., and M. Becken, 2011, Sensitivity of controlled-source electromagnetic fields in planarly layered media: Geophysical Journal International, **187**, 705–728.

Streich, R., M. Becken, and O. Ritter, 2010, Imaging of CO2 storage sites, geothermal reservoirs, and gas shales using controlled-source magnetotellurics: Modeling studies: Chemie der Erde - Geochemistry, **70**, 63–75.

Tietze, K., O. Ritter, C. Patzer, P. Veeken, B. Verboom, et al., 2015a, Borehole Controlled Source Electromagnetic (CSEM) Surveying for Monitoring HC-Saturation in the Bockstedt Oilfield (NW Germany): Presented at the Abu Dhabi International Petroleum Exhibition and Conference, Society of Petroleum Engineers.

Tietze, K., O. Ritter, and P. Veeken, 2015b, Controlled-source electromagnetic monitoring of reservoir oil saturation using a novel borehole-to-surface configuration: Geophysical Prospecting, **63**, 1468–1490.

TNO, 2017, NL Olie en Gasportaal.

Um, E., D. Alumbaugh, J. Harris, and J. Chen, 2012, Numerical modeling analysis of short-offset electric-field measurements with a vertical electric dipole source in complex offshore environments: Geophysics, **77**, E329–E341.

Vilamajó, E., P. Queralt, J. Ledo, and A. Marcuello, 2013, Feasibility of monitoring the Hontomín (Burgos, Spain) CO2 storage site using a deep EM source: Surveys in Geophysics, **34**, 441–461.

Vilamajó, E., B. Rondeleux, P. Queralt, A. Marcuello, and J. Ledo, 2015, A land controlled-source electromagnetic experiment using a deep vertical electric dipole: experimental settings, processing, and first data interpretation: Geophysical Prospecting, **63**, 1527–1540.

Weidelt, P., 2007, Guided waves in marine CSEM: Geophysical Journal International, **171**, 153–176.

Wirianto, M., W. A. Mulder, and E. C. Slob, 2010, A feasibility study of land CSEM reservoir monitoring in a complex 3-D model: Geophysical Journal International, **181**, 741–755.

6

CONCLUSION

The work described in this thesis explores various aspects of land CSEM exploration and monitoring. I have discussed the use of the CSEM method for monitoring applications as a complement to other geophysical methods, primarily to the seismic method. Since the resistivity time-lapse signature can be large while associated changes in acoustic properties may be small, the CSEM method is expected to give benefits in detecting resistivity changes in a reservoir. Beside the rather standard measurements of the horizontal electric-field components discussed in Chapters 3 and 4, the vertical electric-field component was measured by employing shallow boreholes in Chapter 5. To this end, one base survey and two repeat surveys were carried out at the Schoonebeek oil field in the Netherlands. The work especially focused on issues related to time-lapse measurements such as repeatability and on the vertical electric-field component.

Therefore, the advantages and challenges of measuring E_z via shallow boreholes in addition to surface-measured horizontal electric-field components was investigated. In the following, the major conclusions from this work are presented and the scientific and technical implications for monitoring applications are explained in the order of appearance in the previous chapters. In the end, I will give some recommendations for further studies in order to allow for improved data quality and time-lapse measurements in subsequent CSEM monitoring surveys.

6.1. OVERALL CONCLUSIONS

Three separate land CSEM surveys with the same survey geometry were conducted during this study. In Chapter 2, the field survey design was discussed in detail. The main aim of the survey was to test the feasibility of vertical electric-field measurements in shallow boreholes, and the geometry was defined such as to provide background information/models to that data. The survey geometry became a 2D-type geometry since the source and receivers were nearly aligned as in a 2D configuration. Different geometries were tested. Cross-line sources were found to increase (in-line) resolution, whereas cross-line receivers hardly helped to increase (in-line) resolution.

In Chapter 3, I focused on different simulation scenarios by conducting a resolution analysis and by assessing the performance of 1D and 3D inversions using the survey geometry applied in the field and the background geology from the Schoonebeek area. I showed by looking at cumulative sensitivity across the entire depth range that small resistive anomalies can be recognized, but their size and resistivity are hardly recoverable. Complex structures such as small-scale resistivity variations due to steam injection, however, were not resolvable assuming real-data uncertainties. Real-data results from the base survey were processed and inverted. It was shown that the highly-resistive Schoonebeek reservoir can be clearly identified just by using a simple line survey geometry and horizontal electric-field data. Unconstrained 1D inversion has approximately recovered the correct reservoir depth. The introduction of fine layering around the predicted reservoir depth has resulted in a more geologically plausible 1D model that could be used as input for 3D inversion. Lateral variations and small resistive or conductive bodies inside the reservoir, however, could not be resolved as well as anticipated from synthetic studies. From the results of the 3D inversion, I obtained a more complex 3D structure indicating resistivity variation within the reservoir. Its interpretation is difficult without further constraints. Unaccounted features such as metal infrastructure may have limited the ability of the inversions to fit the data and resolve detailed reservoir structure such that the results show most likely actual reservoir structure with an imprint of acquisition geometry and distorted by the influence of unaccounted conductive (or resistive) bodies. Although reservoir depth and large bodies inside the reservoir are detectable, small-scale resistivity structures due to steam injection that are estimated from reservoir simulation data and petrophysical relations cannot be resolved by the CSEM method with the used surface-based survey geometry. However, the general large-scale resistivity structure is possible to detect.

After studying the base survey in detail, I looked at time-lapse changes by comparing the response functions and the inversion results of the base survey to the ones from the two repeat surveys. According to literature and from early simulation studies, I concluded that time-lapse resistivity changes inside the reservoir due to steam injection are too small to be detectable on the horizontal electric-field components. This was confirmed after evaluating the field tests. Small-scale resistivity variations, or time-lapse changes induced by hydrocarbon production and steam injection over the short time period of our measurements, are not detectable; most likely this will not even be detectable with better EM data coverage and more accurate knowledge of the background resistivity model. Subtle resistivity changes inside the reservoir are only recognizable in highly repeatable time-lapse CSEM data and thus efforts toward minimizing the errors due to inaccurate surface geometry and noise sources were taken. I found from synthetic studies that the resistivity changes inside the reservoir during the short time period of less than two years between the three acquired surveys were expected to be minor and relative changes between the data were expected to be no more than ~1% at most locations, and thus too low to be detectable. Therefore, the main focus of Chapter 4 is on the issue of repeatability of the CSEM measurements to assure high-quality data sets for future monitoring applications. To enhance data quality and subsequently decrease repeatability errors, more attention needs to be focused on accurate source and receiver positioning. Procedures used for one-time CSEM surveys such as measuring

receiver midpoints and dipole length only, have to be adjusted to achieve the necessary repeatability. Measuring each receiver electrode location by differential GPS and GPS-based layout of the source cables should be done for each survey to minimize discrepancies between the survey layouts. Imprecise layout together with technical challenges such as high-cultural EM noise, near-surface heterogeneities and metallic objects near the measurement equipment showed that slight changes in receiver location may lead to relative changes between the different data sets a multiple larger than changes of interest, i.e. due to steam injection. On the source side, it was found that the source base frequencies of the source signals should be identical for all surveys in order to avoid inaccuracies during data processing. Throughout the three surveys, data quality slightly increased, most likely related to updated source-signal periods and transmission times. The better data quality of the third survey is mainly the result of less man-made EM noise due to the stoppage of steam injection and oil production before the beginning of the third survey. Repeatability errors were about 2 3% for shorter-offset data (up to 6 km), but increased to 5 10% for the longest offsets in the survey. In principle, signal-to-noise ratios at large offsets should be improvable by longer recordings and/or stronger source currents. The latter, however, is not possible with the source used. Separate 1D inversions for the three surveys show a good match whereas resistivity updates as a result of 3D inversions show no clear trend of resistivity change between the three surveys. Using previous-survey inversion results as the starting model of the subsequent survey and thus simulating time-lapse inversions led to only minor inversion updates that could not be associated with changes due to steam injection and oil production. This is a direct cause of the similarity of the three data sets. Using the suggested improvements to achieve higher-accuracy and higher-quality measurements, repeatability errors might be lowered by another ~1%, thus suggesting that land CSEM reservoir monitoring has a potential to add additional information to reservoir monitoring.

I have shown that time-lapse changes of the horizontal electric-field data are too small to be detectable assuming a monitoring period of less than two years. Another component, that is more sensitive to resistivity changes inside the reservoir, is the vertical electric-field component E_z. In Chapter 5, I have studied the advantages and challenges of using this component. Sensitivity analyses have shown that E_z is the most sensitive component to reservoir changes; it is more sensitive than the horizontal electric-field (and the three magnetic-field) components used in the previous chapters. I found that vertical electric-field data are much more difficult to fit via modeling than horizontal electric-field data. The E_z inversions were less stable and returned a reservoir at its known depth only after careful tuning of inversion parameters. Synthetic studies revealed that cumulative sensitivity to the depth range containing the receivers is 1-2 orders of magnitude higher than to other depths resulting in decreased vertical resolution of E_z. The inversion can benefit from including a-priori knowledge as a constraint, such as resistivity distribution obtained after 1D and 3D inversion of horizontal electric-field data and additional near-surface resistivity information. Further, the influence of borehole deviation has to be taken into account precisely. The analysis of real E_z data has shown that recording this component accurately and reliably is challenging. Apart from the expected lower signal amplitudes compared to the horizontal electric-field components, relative noise levels were higher (i.e., signal-to-noise ratios were lower) indicat-

ing that more attention on minimizing noise sources is necessary in order to improve the signal-to-noise ratio. The E_z measurements were similar and moderately repeatable between the three surveys but could not (yet) be fitted to an acceptable level and consequently a reliable subsurface model from E_z data is still missing. Modeling that includes the exact position of nearby well casings has revealed that casings can cause large changes in amplitude and phase suggesting that accurate inclusion of position and trajectories of well casings into the initial model for inversion in future studies may lead to acceptable data fits. Although there are many challenges that need to be overcome, theoretical studies provide abundant indication that E_z should be able to detect resistivity changes at reservoir level that might not be detectable by the horizontal electric-field components. Further work is required to enable us to use E_z to its full potential.

6.2. OUTLOOK AND FURTHER STUDIES

In this section, recommendations for further studies and an outlook on using the land CSEM method for reservoir monitoring is given. The findings of this thesis are used to discuss improvements for future land CSEM surveys.

For future monitoring surveys, more efforts should be invested to minimize inaccuracies in source and receiver positioning. Apart from the discussed efforts to use differential GPS measurements on all electrode locations to more accurately measure the exact positions, a more permanent set-up may be beneficial to further reduce repeatability errors. By burying both receivers and source cables, noise picked up by weather conditions (e.g., rain and wind) can be possibly reduced. On the receiver side, a buried grid of electrodes has the added advantage that in principle, different electrode combinations may be usable, subject to further equipment development, and optimized for 3D monitoring. This is similar in concept to what is used in DC-resistivity imaging, although forming arbitrary electrode pairs from an electrode array is not as straightforward as in DC surveys, due to the additional electromagnetic interaction that needs to be considered. Different electrode combinations were studied but were not discussed in the main body of the thesis. An issue that came up is that signals are small in amplitude such that amplifiers are needed to transport the signal over to a central recording unit. Also, the long-term stability of the electrodes is an issue and needs to be studied and improved in the future. On the long-term, subsurface array measurements may replace surface measurements for monitoring purposes. One initial surface-based survey may then be followed by subsequent surveys using subsurface sensors only. More studies are needed to investigate the E_z component. Since the E_z data could not be properly modeled during the time of this work, inversion of the E_z data was only slightly discussed here although more provisional inversion trials were executed. The complexity of the starting model may need to be increased and reasons for the observed unexpectedly high E_z amplitudes need to be investigated further.

One issue that emerged during the study of E_z and was not properly taken into account, is the influence of steel casings and pipelines on the data. Steel is a very good conductor and thus can create a strong secondary electromagnetic field that contaminates the data. Recent studies in the literature show the importance of including metal casings into modeling. Swidinsky et al. (2013) have studied the influence of borehole casings in a marine setting and concluded that boreholes must be at least 200 m away from the CSEM

array in order to minimize the effects of the casings. The electromagnetic response of conductive steel borehole casings was analytically and numerically modeled by several research groups, primarily to investigate the possibility to enable steel-cased wells in or near a hydrocarbon reservoir as galvanic sources for time-lapse monitoring (Yang et al., 2009; Kong et al., 2009; Cuevas, 2012, 2014; Tang et al., 2015; Commer et al., 2015; Um et al., 2015). In most of the approaches, the casing is considered as a secondary source, thus allowing to model well casing effects (approximately) while avoiding explicit, numerically very expensive discretization of the casing. The effect of steel-cased wells on collected data for electromagnetic surveys was studied by Kohnke et al. (2017).

The Schoonebeek oilfield is perforated with many steel-cased wells and many pipelines are present at the surface. Since wells and pipelines are all over the place, it was impossible to define source and receiver locations such that they were not in the vicinity of these wells and metal body locations were thus hardly considered before defining the survey geometry; only the immediate vicinity to wells was avoided. Accordingly, the recorded data showed significant indications of metal interferences. Therefore, it was also necessary to model the effect of these steel objects on the collected data. The tests in this thesis suggest that the influence of the well casings is not big enough to explain observed amplitudes, yet more accurate modeling techniques than the effective medium approach used here would have to be used to verify this. Recent studies conducted by others inside Shell (private communications) indicated that a horizontal pipeline close to receiver location R6 is likely to be the primary source of metal interference. Detailed studies that include both steel casings and pipelines are still needed to be able to better understand the data. In contrast to inverting the horizontal electric-field components, it was found that for inverting the vertical data conductive steel bodies in the vicinity of the sources and receivers need to be incorporated into the starting model.

The data in this thesis were entirely processed in the frequency domain and the entire acquisition was designed for that purpose. Since the strong air-wave signal is usually easier to separate in the time domain, time-domain processing of the data or part of the data may give additional insight that might help in data interpretation. Further studies should therefore also consider time domain interpretation.

Due to the generally low resolution, EM data is often interpreted together with other available data. The capability of the EM method to recognize resistivity changes can be combined with detailed local information that may be gathered from well-logs, geological information, different EM data such as the vertical electric field E_z or from other geophysical data (e.g., seismic) and may be used for joint data interpretation. Since EM data are lacking the resolution that other geophysical methods such as the seismic method are likely to provide, combining time-lapse measurements of the vertical (and horizontal) electric field with seismic data is deemed to be beneficial and may potentially be an economically viable alternative to high-resolution 4D seismic. Joint data interpretation or even joint inversion of CSEM and seismic data acquired at the site may further reduce the uncertainty in our interpretation. At Schoonebeek, high-resolution seismic data using the so-called SeisMovie system are available and exist at the central position of our survey. Combining these data with our measured data may be the next step for a better image of the subsurface changes. One of the challenges that need to be handled, is how to combine data with significantly different resolution possibilities.

REFERENCES

Commer, M., G. M. Hoversten, and E. S. Um, 2015, Transient-electromagnetic finite-difference time-domain earth modeling over steel infrastructure: Geophysics, **80**, E147–E162.

Cuevas, N., 2012, Casing effect in borehole-surface (surfaceborehole) em fields: 74th European Association of Geoscientists and Engineers Conference and Exhibition 2012 Incorporating SPE EUROPEC 2012: Responsibly Securing Natural Resources, 2939–2943.

Cuevas, N. H., 2014, Analytical solutions of EM fields due to a dipolar source inside an infinite casing: Geophysics, **79**, E231–E241.

Kohnke, C., L. Liu, R. Streich, and A. Swidinsky, 2017, A Method of Moments Solution to the Conductive Steel Casing Problem-Theory, Validation and Model Studies: Presented at the 79th EAGE Conference and Exhibition 2017.

Kong, F. N., F. Roth, P. A. Olsen, and S. O. Stalheim, 2009, Casing effects in the sea-to-borehole electromagnetic method: Geophysics, **74**, F77–F87.

Swidinsky, A., R. N. Edwards, and M. Jegen, 2013, The marine controlled source electromagnetic response of a steel borehole casing: Applications for the NEPTUNE Canada gas hydrate observatory: Geophysical Prospecting, **61**, 842–856.

Tang, W., Y. Li, A. Swidinsky, and J. Liu, 2015, Three-dimensional controlled-source electromagnetic modelling with a well casing as a grounded source: a hybrid method of moments and finite element scheme: Geophysical Prospecting, **63**, 1491–1507.

Um, E. S., M. Commer, G. A. Newman, and G. M. Hoversten, 2015, Finite element modelling of transient electromagnetic fields near steel-cased wells: Geophysical Journal International, **202**, 901–913.

Yang, W., C. Torres-Verd J. Hou, and Z. Zhang, 2009, 1D subsurface electromagnetic fields excited by energized steel casing: Geophysics, **74**, E159–E180.

SUMMARY

Geophysical methods are widely used for hydrocarbon exploration and time-lapse measurements. One method that can be applied in place of or in addition to the routinely used seismic method, is the Controlled-Source ElectroMagnetic (CSEM) method. The work described in this thesis explores various aspects to improve the land CSEM method for exploration and monitoring purposes. Therefore, three separate active land CSEM field experiments, a baseline and two repeat surveys, were carried out over a period of nearly two years at the Dutch Schoonebeek oil field, where heavy oil is produced by injecting steam to reduce the viscosity of the oil. Steam injection and oil production have to be closely monitored to prevent breakthrough of steam to production wells and to detect possible unwanted leakage or contamination of groundwater such that further measures can be taken.

First, the use of the CSEM method for oil and gas exploration is discussed. This is done by focusing on different simulation scenarios, by conducting resolution analysis and by assessing the performance of 1D and 3D inversions using the survey geometry applied in the field and the background geology from the Schoonebeek area. It was shown that small resistive anomalies can be recognized but their size and resistivity are hardly recoverable. Complex structures such as small-scale resistivity variations due to steam injection, however, were not resolvable assuming real-data uncertainties. Real-data results from the base survey were processed and inverted. It was shown that the highly-resistive Schoonebeek reservoir can be clearly identified by using a simple line survey geometry and horizontal electric-field data. Unconstrained 1D inversion has approximately recovered the correct reservoir depth. Introduction of fine layering around the predicted reservoir depth has resulted in a more geologically plausible 1D model that could be used as input for 3D inversion. From the results of the 3D inversion, a more complex 3D structure indicating resistivity variation within the reservoir was obtained. Unaccounted features such as metal infrastructure may have limited the ability of the inversions to fit the data and resolve detailed reservoir structure such that the results show most likely actual reservoir structure with an imprint of acquisition geometry and distorted by the influence of unaccounted conductive (or resistive) bodies. Although reservoir depth and large bodies inside the reservoir are detectable, small-scale resistivity structures due to steam injection that are estimated from reservoir simulation data and petrophysical relations cannot be resolved by the CSEM method with the used surface-based survey geometry.

Second, after studying the base survey in detail, I looked at time-lapse changes by comparing the base survey with the two repeat surveys. According to literature and from early simulation studies, time-lapse resistivity changes inside the reservoir due to steam injection are likely too small to be detectable on the horizontal electric-field components. This was confirmed after evaluating the field tests. Small-scale resistivity variations or time-lapse changes induced by hydrocarbon production and steam in-

jection over the time period of our measurements are not detectable. Subtle resistivity changes inside the reservoir are only recognizable in highly-repeatable time-lapse CSEM data and thus efforts in minimizing the errors due to inaccurate surface geometry and noise sources were taken. Therefore, I focused on the issue of repeatability of the CSEM measurements to assure high-quality data sets for future monitoring applications. I have shown that to enhance data quality and subsequently decrease repeatability errors, more attention needs to be focused on accurate source and receiver positions. Procedures that are used for one-time CSEM surveys have to be adjusted to achieve the necessary repeatability. Imprecise layout together with technical challenges such as high-cultural EM noise, near-surface heterogeneities and metallic objects near the measurement equipment showed that slight changes in receiver location may lead to relative changes between the different data sets of >10%, which is an order of magnitude larger than changes of interest, i.e. due to steam injection. On the source side, it was found that the source signals should be exactly identical for all surveys in order to avoid inaccuracies during data processing. During the three surveys, data quality slightly increased most likely linked to updated source signal periods and transmission times. The better data quality of the third survey is also the result of less man-made EM-noise due to the stoppage of steam injection and oil production before the beginning of the third survey.

Repeatability errors were about 2 3% for shorter-offset data (up to 6 km), but increased to 5 10% for the longest offsets in the survey. Signal-to-noise ratios at large offsets can, in principle, be improved by longer recordings and/or stronger source currents. The latter, however, is not possible with the source used. Separate 1D inversions for the three surveys showed a good match whereas resistivity updates as a result of 3D inversions showed no clear pattern between the three surveys. Using previous survey inversion results as the starting model of the subsequent survey and thus simulating time-lapse inversions led to only minor inversion updates that could not be associated with changes due to steam injection and oil production. This is a direct cause of the similarity of the three data sets. Using the suggested improvements to achieve higher-accuracy and higher-quality measurements, repeatability errors might be lowered by another ~1%. If that can be achieved, land CSEM reservoir monitoring has a potential to add additional information to reservoir monitoring.

I have shown that time-lapse changes of the horizontal electric-field data are too small to be detectable assuming a monitoring period of less than two years. Another component, that is more sensitive to resistivity changes inside the reservoir, is the vertical electric-field component E_z. This component can be measured by employing shallow boreholes, but accurate and reliable recording via boreholes is more challenging than recording surface measurements. I studied the advantages and challenges of using the E_z component. Sensitivity analyses showed that the E_z component, in theory, is very sensitive to reservoir changes and more sensitive than the horizontal electric-field components. The analysis of the vertical electric-field data has shown that the data are much more difficult to fit via modeling than horizontal electric-field data. E_z measurements were fairly repeatable between the three surveys but could not (yet) be fitted to an acceptable level and consequently a reliable subsurface model from E_z data is still missing. The E_z inversions were less stable and returned a reservoir at its known depth only

after careful tuning of inversion parameters. Synthetic studies revealed that cumulative sensitivity to the depth range containing the receivers is 1-2 orders of magnitude higher than to other depths resulting in decreased vertical resolution of E_z. The inversion can benefit when including a-priori knowledge as a constraint, such as resistivity distribution obtained after 1D and 3D inversion of horizontal electric-field data and additional near-surface resistivity information. Apart from the expected lower signal amplitudes compared to the horizontal electric-field components, relative noise levels were higher indicating that more attention on minimizing noise sources is necessary in order to improve the signal-to-noise ratio. Further, the influence of borehole deviation has to be taken into account in modeling, inversion and interpretation of the data. Modeling that includes the exact position of nearby well casings has indicated strong dependency of amplitude and phase on well casings, suggesting that accurate inclusion of position and trajectories of well casings and pipelines into the initial model for inversion in future studies may lead to much better data fits. Although there are many challenges that need to be overcome, theoretical studies provide abundant indication that E_z should be able to detect resistivity changes at reservoir level that might not be detectable by the horizontal electric-field components. Further work is required to be able to use E_z to its full potential.